Modelling the gobforming process in glass production

van der Ven, M.F.

Award date:
2006

Modelling the gobforming process in glass production

M.F. van der Ven
Reportnumber WET 2006.13

Supervisors: Dr. Ir. C.C.M. Rindt
Dr. Ir. O.M.G.C. op den Camp
Prof. Dr. Ir. A.A.v. Steenhoven

Eindhoven University of Technology
Department of Mechanical Engineering
Division Thermo Fluids Engineering
Section Energy Technology

Contents

Nomenclature

Roman symbols

A	surface area	m^2
c	material label	$-$
c_p	specific heat capacity	$Jkg^{-1}K^{-1}$
e	emissive power	Wm^{-2}
g	gravitational acceleration	ms^{-2}
i	radiation intensity	$Wm^{-2}sr^{-1}$
k	thermal conductivity	$Wm^{-1}K^{-1}$
L	characteristic length	m
n	index of refraction	$-$
p	pressure	Pa
q	heat flux	Wm^{-2}
s	thickness	m
S	distance	m
t	time	s
t_0	initial time	s
T	temperature	$°C(or K)$
T_0	initial temperature	$°C(or K)$
ΔT	temperature difference	$°C(or K)$
u	velocity	ms^{-1}
U	characteristic velocity	ms^{-1}
V	volume	m^3
x, y, z	spatial coordinates	m

Greek symbols

α	absorption coefficient	m^{-1}
α_w	absorptance at a wall	$-$
ε	emissivity, emission coefficient	$-$
Γ	boundary	$-$
η	dynamic viscosity	Pas
κ	extinction coefficient	m^{-1}
λ	wavelength	m
ν	frequency	Hz
ρ	density	kgm^{-3}
ρ_w	reflectance at a wall	$-$
σ	Stefan-Boltzmann constant	$Wm^{-2}K^{-4}$

$\boldsymbol{\sigma}$	stress tensor	Pa
τ	characteristic time	s
τ_w	transmittance at a wall	$-$
ϕ	shape function	$-$
φ	azimuthal angle	rad
ψ	(pressure) shape function	$-$
ω	solid angle	sr
Ω	computational domain	$-$

Dimensionless numbers

Ca	Capillary number	$=$	$\frac{\text{viscous force}}{\text{interfacial tension force}}$
Fo	Fourier number	$=$	$\frac{\text{elapsed time}}{\text{characteristic cooling time}}$
Fr	Froude number	$=$	$\frac{\text{inertia force}}{\text{gravity force}}$
Gr	Grashof	$=$	$\frac{\text{buoyancy force}}{\text{viscous force}}$
M	conduction / radiation parameter	$=$	$\frac{\text{heat conduction}}{\text{heat radiation}}$
Pe	Péclet number	$=$	$\frac{\text{heat convection}}{\text{heat conduction}}$
Pr	Prandtl number	$=$	$\frac{\text{momentum diffusivity}}{\text{thermal diffusivity}}$
Ra	Rayleigh number	$=$	$GrPr$
Re	Reynolds number	$=$	$\frac{\text{inertia force}}{\text{viscous force}}$
Sr	Strouhal number	$=$	$\frac{\text{instationary inertia force}}{\text{stationary inertia force}}$

Summary

In a glass production process, single glass gobs are produced out of a continuous glass flow. The gobs are cut and led to a final forming stage. In this process a reproducible gob weight, gob shape and temperature distribution are essential, as they effect the uniformity and the reproducibility of the end-products. A non-uniformity of the temperature profile in the final forming stage could lead to local defects, high internal stresses and deformations in the end-products. This temperature profile can be derived from the distribution in the gob. For a better understanding and control of the production process, a gobform model has been developed in which the gob shape end temperature profile can be simulated.

The gobform model is based on the finite element method. It employs a pseudo-concentration method, in which the governing equations are solved on a fixed grid that covers the entire domain. In this domain the distinction is made between the glass gob and the air that surrounds the gob. Since we are not interested in the air domain, the air is replaced by a fictitious fluid with a viscosity of the order of 10^{-3} times the glass viscosity but with the same density. This way the Reynolds number is reduced, without interfering with the interaction between the glass and the air. Due to the reduced Reynolds number, we can neglect the non-linear terms in the conservation of momentum equation. In the pseudo-concentration method, a material label is introduced, c, to distinguish the glass from the fictitious fluid. All the material properties are defined as a function of this material label.

In a gob forming process, the heat transfer of the gob to the surroundings is dominated by radiative heat transfer. The ratio of the convective heat transfer in the air at the glass surface is about 6%. The main challenge in the modelling of the gobform process is the semitransparent radiative heat transfer properties in combination with the moving free surface of the glass gob. At this point, known radiation models based on the DOM-method as for example the improved diffusion approximation of Lentes and Siedow, are not yet able to deal with material interfaces. Therefore, a method is derived in which a distinction is made in the radiative heat transfer internally in the glass and through the glass surface to the surroundings. Internally, in the glass gob, a Rosseland approximation is used. For the implementation of the heat transfer to the surroundings two different methods are developed. In the one, the TRH-method, the heat flux is prescribed as a proportional heat flux at a boundary of choice of the computational domain. In the other, the IRH-method, the heat transfer is prescribed as a heat sink at the glass surface. The magnitude of the heat flux is approximated using $q_r = \sigma\varepsilon({T_{glass}}^4 - {T_{ambient}}^4)$. In our case, ε, this is the total hemispherical emissivity.

An example for the emissivity ε is derived from spectral energy measurement of float glass. These experiments are performed at temperatures of 600, 700 and 800 °C. These results are extrapolated to the desired gobform temperature domain of about 1000 °C. An analysis of the temperature dependency of the absorption coefficient shows that this extrapolation is valid. The spectral energy measurements are performed perpendicular to the glass samples. Therefore, the directional dependency is taken into account using literature values. The results are compared with the emissivity derived using data from TNO of the absorption coefficient of a comparable glass type. Comparison showed similar results. An experimental analysis is performed with respect to the optical alignment, the spectral transformation factor, the ground intensity and the reproducibility.

Validation of the gobform model is carried out using numerical tests as well as experimental

data from a scaled (isothermal) gobform simulation set-up from LG.Philips. In the numerical tests, different parts of the gobform model are tested individually. They showed good results in comparison to a reference solution. Comparison between the gobform model and the data from LG.Philips gave a deviating solution with regards to the gob shape. This is the result of an ill-defined inflow boundary condition at the spout orifice and the shortage of information of the influence of the cutting mechanism. This inflow boundary condition, is responsible for a gob mass deviation of 5 to 50%. The influence of the cutting mechanism is derived from the characteristic gob length results, given in the data from LG.Philips. Based on these findings, the data from LG.Philips can not be used in the validation of the gobform model.

In conclusion, the developed model enables the simulation of the gob forming process. Contrary to frequently used radiation models, the implemented radiative heat transfer is able to deal with a moving material interface.

Chapter 1

Introduction

1.1 Problem description

The glass industry produces glass in mass production. Because of its material properties, glass is used in all sorts of applications in the packing industry as well as in the high-tech industry. The production of glass is a continuous process, whereas the end-products often are discrete objects such as bottles, jars, tableware glasses or TV-panels. In order to manufacture discrete products in a continuous production process, single glass gobs are produced out of the continuous glass flow. The glass flows through a spout orifice in the bottom of a glass feeder and is cut in portions by a set of shears. The flow through the orifice is controlled by a pen or gobber. The rate of production of gobs is about 2 gobs per second for small sized bottles or jars to about 12 seconds per gob for large sized TV-panels. After the gob cutting, the gob is led to the final stage of the formation process, in which the end product is formed.

In this continuous process a reproducible gob weight, gob shape and temperature distribution are essential, as they effect the uniformity and the reproducibility of the forming process, [1]. The gob weight is determined by the temperature distribution in the spout, the pen or gobber stroke, the glass level in the spout, the spout orifice diameter and the application of a spanker for the support of large glass gobs during the gob formation.

A non-uniformity of the temperature profile in the forming stage of the end-product could lead to local defects, high internal stresses and deformed end-products. This temperature profile can be derived from the temperature distribution of the gob. Therefore a good prediction of the temperature distribution of the gob is required for a better understanding and control of the production process.

Figure 1.1: The gobforming process

The temperature distribution of the gob originates from the temperature distribution in the feeder, the flow through the orifice, and the heat transfer during the formation of the gob. During the formation of the gob, show in figure 1.1, the heat transfer is dominated by radiative heat

transfer. Because glass is semitransparent, it emits and absorbs radiation from every direction. This makes radiation a complex effect that covers the complete surroundings. This is in contrast to conduction, which is a local effect.

TNO has developed a preliminary simulation tool for gob forming, in which the radiation within the glass has been modelled by means of the Rosseland approximation. This simulation tool does not yet cover radiative heat transfer from the glass to the surroundings. The Rosseland approximation takes the radiation into account, as a contribution to the conductivity term in the conservation of energy balance. In cooperation with the Eindhoven University of Technology, TNO has also developed a simulation tool for radiative heat transfer within glass by means of a discrete ordinate radiation model.

In this research, the objective is to model the process of gobforming with radiative heat transfer with the finite element package SEPRAN. Different radiation models (Rosseland, non-spectral DOM, improved diffusion approximation of Lentes and Siedow) are investigated on their applicability for the gobform model. Verification procedures for the model are examined, preferably on basis of laboratory or industrial measurements.

1.2 Outline of the report

The main problem in the modelling of the gobform process is the semitransparent radiative heat transfer properties of glass in combination with a moving free surface. Usually, numerical implementation of radiative heat transfer in glass is achieved for fixed surfaces with prescribed boundary conditions instead of moving surfaces. For this reason, the use of a moving free surface in combination with known radiation models has to be evaluated. In addition to radiation, part of the heat transfer at the gob surface is caused by convection.

This thesis has the following structure. Chapter 2 discusses the heat transfer in the gobform process. Since radiation plays an important role, we discuss some of the theoretical principles. A selection in the known radiation models is made, based on their ability to deal with a moving free surface. In chapter 3, the construction and implementation of the gobform model are discussed. The governing equations are shown and rewritten in dimensionless form for the evaluation of the different terms. Special attention is paid to the implementation of the radiative heat transfer for which two different methods are derived. Both methods require information about the emissivity, a measurable temperature dependent material property. The emissivity is measured using an experimental set-up. In chapter 4, the determination of the emissivity is discussed, as well as an analysis of the performed experiments is given. As an example, the emissivity of Float glass is derived. To verify the gobform model, the validation method and the results are discussed in chapter 5. Finally, in chapter 6 conclusions and recommendations are given.

Chapter 2

Heat transfer in the gobform process

Heat transfer can be dominated by conduction, convection, radiation or a combination. Depending on the temperature region, the dominant heat transfer mechanisms can be classified following [2]:

$$\begin{array}{rl} T < 300\,^{\circ}\mathrm{C} & \text{conduction} \\ 300\,^{\circ}\mathrm{C} < T < 800\,^{\circ}\mathrm{C} & \text{conduction and radiation} \\ 800\,^{\circ}\mathrm{C} < T & \text{radiation and convection} \end{array} \tag{2.1}$$

Here, convection stands for the flow mechanisms in the glass melt or the flow during the forming process. The glass in the gobform process has a temperature of about 1000 °C. During the process the gob cools by approximation $10 - 50\,^{\circ}\mathrm{C}$, depending on size and cycle-time. The gob is cooled as a result of radiative heat transfer to the surroundings and convective heat transfer in the air film surrounding the gob.

In this chapter, the heat transfer mechanisms during the gobform process are discussed. It has the following structure. First, the ratio between the convective and the radiative heat transfer to the surroundings is evaluated. This heat transfer is dominated by radiation. Then, an introduction in radiative heat transfer is given with the most important interfacial radiation effects. Finally, for the implementation of the radiative heat transfer, the applicability of known radiation models based on the Rosseland approximation or the DOM-method, are discussed.

2.1 Evaluation of the heat transfer to the surroundings

The radiative heat transfer q_r of the gob to the surroundings is approximated, [3], using:

$$q_r \cong \sigma \left({T_{gob}}^4 - {T_\infty}^4 \right) \tag{2.2}$$

with T_{gob} the temperature of the gob and T_∞ the ambient temperature. An approximation for the natural, and forced convective heat transfer in the air film surrounding the gob is derived below.

Natural convection

The flow in the thermal boundary layer is considered laminar since the Grashof number is $< 10^9$. The Prandtl number is about $Pr = 0.70$ for air in the boundary layer with a film temperature of about 500 °C. For the glass gob, we can now use a Nusselt relation for a spheroid shape as described in [3], in which:

$$\overline{\mathrm{Nu}}_{\mathcal{L}} = 3.47 + 0.51 \mathrm{Ra}_{\mathcal{L}}^{1/4} \tag{2.3}$$

with $\mathrm{Ra}_{\mathcal{L}}$ the Rayleigh number. The heat flux as a result of natural convection can now be calculated with:

$$q_c = \frac{\overline{\mathrm{Nu}}_{\mathcal{L}} k \Delta T}{\mathcal{L}} \tag{2.4}$$

In which k is the conduction coefficient, ΔT the temperature difference between glass and air, and $\mathcal{L}$ the square root of the entire surface of the gob.

Forced convection

The relative velocity of the glass with respect to the air during the gobforming process can be considered to contribute as a forced convection in the convective heat transfer. In the evaluation procedure we use the following Nusselt correlation for a spheroid shape, as described in [3]:

$$\overline{\mathrm{Nu}}_{\mathcal{L}} = \overline{\mathrm{Nu}}^{0}_{\mathcal{L}} + \left[0.15\left(\frac{p}{\mathcal{L}}\right)^{1/2} Re_{\mathcal{L}}^{1/2} + 0.35 Re_{\mathcal{L}}^{0.566}\right] Pr^{1/3} \tag{2.5}$$

with $Re_{\mathcal{L}}$ the $\mathcal{L}$-based Reynolds number ($0 < Re_{\mathcal{L}} < 2\times 10^5$), p the maximum equatorial perimeter of the glass gob perpendicular to the flow direction and $\overline{\mathrm{Nu}}^{0}_{\mathcal{L}}$ a given constant depending on the spheroid shape. The heat flux is calculated with equation 2.4.

Ratio between the convective and radiative heat transfer

The contribution of the natural or forced convection at the glass surface is compared to the radiative heat transfer in Figure 2.1. With a maximum contribution of the (forced) convection of about 6% of the radiative heat transfer, the convective heat transfer is neglected. The benefit is that the radiative heat transfer of the glass to the surroundings can be implemented more easily in the gobform model, as discussed in section 3.6.

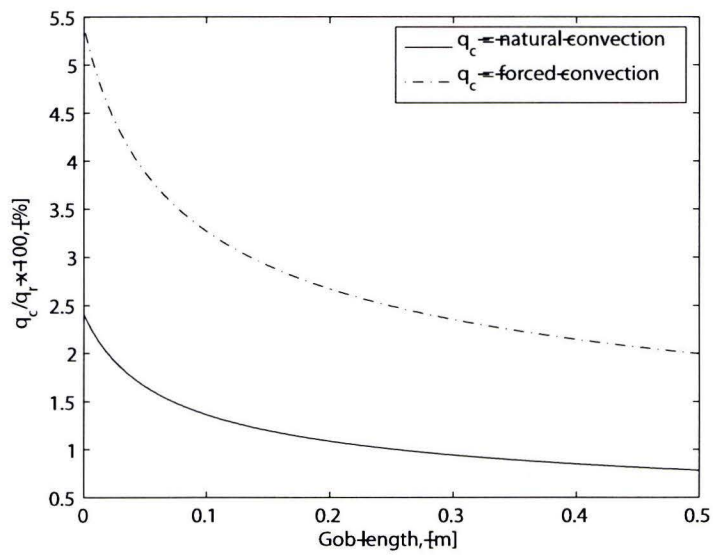

Figure 2.1: Convective to radiative heat flux ratio

2.2 Radiative heat transfer

2.2.1 Blackbody radiation

In thermal radiation calculations, the concept of a black body is of considerable importance. A blackbody is defined as a perfect absorber and emitter for all wavelengths and directions. In radiative heat transfer studies, it serves as a standard to which real objects can be compared. For calculations on the total radiative energy transfer of an object, important parameters are the hemispherical emissive power e and radiant intensity i. The spectral distributions of hemispherical emissive power and radiant intensity for a blackbody in vacuum are given as a function of wavelength and the blackbody's absolute temperature by Planck's spectral distribution of emissive power:

$$e_{\lambda b}(\lambda_0, T) = \pi i_{\lambda b}(\lambda_0, T) = \frac{2\pi C_1}{\lambda_0^5 (e^{C_2/(\lambda_0 T)} - 1)} \tag{2.6}$$

with λ_0 denotes the wavelength, T denotes the temperature, $C_1 = hc_0^2$ and $C_2 = hc_0/k$ where c_0 is the speed of light, h is Planck's constant and k is the Boltzmann constant. The subscript "0" denotes the related property in vacuum. Equation (2.6) can be used where radiant emission is usually into air or other gases with an index of refraction $n = c_0/c$ close to 1. For radiation into a medium within which the speed of light is not close to c_0, equation (2.6) must be modified to become:

$$e_{\lambda b}(\lambda_0, T) = \frac{2n^2\pi C_1}{\lambda_0^5 (e^{C_2/(\lambda_0 T)} - 1)} \tag{2.7}$$

Another useful quantity is the wavelength for which the blackbody intensity $i_{\lambda b}(\lambda)$ is maximal for a given temperature. It can be calculated using Wien's displacement law:

$$\lambda_{max,m} = \frac{\lambda_{max,0}}{n} = \frac{C_3}{nT} \tag{2.8}$$

where the subscript "m" denotes the wavelength in a medium and C_3 Wien's displacement law constant. To calculate the total blackbody intensity, the spectral intensity is integrated over all wavelengths, together with Planck's spectral distribution giving:

$$i_b = \int_0^\infty i_{\lambda b}(\lambda) d\lambda = \int_0^\infty \frac{2n^2 C_1}{\lambda_0^5 (e^{C_2/(\lambda_0 T)} - 1)} \, d\lambda = \frac{n^2 \sigma}{\pi} T^4 \tag{2.9}$$

Here, σ denotes the Stefan Boltzmann constant. The hemispherical total emissive power of a blackbody is then:

$$e_b = \int_0^\infty e_{\lambda b}(\lambda) d\lambda = \pi i_b = n^2 \sigma T^4 \tag{2.10}$$

All radiative constants discussed in this section are given in appendix A.

2.2.2 Radiation intensity transfer equation

In transmitting material, radiative heat transfer is often described using radiation intensity. Here the spectral radiation intensity, i_λ is defined as the radiant energy passing through an area per unit of time, per unit of the projected area, per unit solid angle and per unit small wavelength interval around the wavelength λ. The radiative intensity throughout translucent material can be obtained using the radiation intensity equation of transfer. Consider spectral radiation of intensity $i_\lambda(S)$, travelling through an absorbing, emitting, and scattering medium over a distance dS, as shown in Figure 2.2. The radiation intensity decrease by absorption is:

$$di_{\lambda,\alpha} = -\alpha_\lambda(S) \; i_\lambda(S) \, dS \tag{2.11}$$

with $\alpha_\lambda(S)$ the spectral medium absorption coefficient with unity $[m^{-1}]$. If the radiation along the path is in local thermodynamic equilibrium, the intensity increase as a result of local spontaneous emission over dS is:

$$di_{\lambda,e} = \alpha_\lambda(S) \, i_{b\lambda}(S) \, dS \tag{2.12}$$

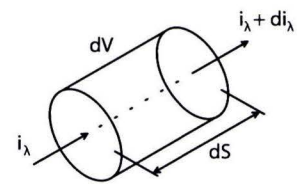

Figure 2.2: Radiation travelling over distance dS through volume dV of a medium

with $i_{b\lambda}(S)$ the black body intensity of the medium. Depending on material properties, the radiation intensity travelling over dS can also be decreased by scattering an amount of radiation out of the volume dV as well as increased by an amount of radiation intensity scattered into the volume dV. The nett change in radiation intensity as a result of scattering is given by:

$$di_{\lambda,s} = -\sigma_{\lambda,s}(S)\, i_\lambda(S)\, dS + \frac{\sigma_{\lambda,s} dS}{4\pi} \int_{\omega_i=0}^{4\pi} i_\lambda(S)\, \Phi_\lambda(\omega, \omega_i)\, d\omega_i \tag{2.13}$$

with $\sigma_{\lambda,s}$ the scattering coefficient and $\Phi_\lambda(\omega, \omega_i)$ the phase function for scattering from solid angle ω_i to solid angle ω. The combination of equation (2.11) to (2.13) gives the total change of intensity travelling along dS, known as the transport transfer equation for radiation intensity. For a non-scattering medium, $\sigma_{\lambda,s} = 0$, the transfer equation simplifies to:

$$\frac{di_\lambda}{dS} = -\alpha_\lambda(S)\, i_\lambda(S) + \alpha_\lambda(S)\, i_{b\lambda}(S) \tag{2.14}$$

Next, consider a transparent medium with uniform temperature and uniform composition then the solution of equation (2.14) states:

$$i_\lambda(S) = i_\lambda(0)\; e^{-\alpha_\lambda S} + \left(1 - e^{-\alpha_\lambda S}\right)\; i_{b\lambda} \tag{2.15}$$

Note the spectral dependency of the intensity and the absorption coefficient.

2.2.3 Interfacial radiation effects

In general, detailed radiation models do not cover interfacial radiation. The sheer complexity limits accurate numerical description or introduces long computation times. Incorporation of the interfacial radiative heat transfer effects in the gobform process would go beyond the scope of this research. Therefore these effects are approximated or neglected. Because of their importance, the general effects of radiation on surfaces as well as a short overview of the most important interfacial radiative effects are worth discussing in this section.

General effects on surfaces

Consider radiation impinging on a wall with intensity i_{in}. Part of the radiation intensity is reflected away from the medium, a part is absorbed inside the layer and the rest is transmitted through the wall, or surface. These characteristics, reflectance, absorptance and transmittance, are the three fundamental radiative properties on a wall. They are described by:

$$\begin{aligned}
&\text{Reflectance,} && \rho_w \equiv \tfrac{i_r}{i_{in}} = \frac{\text{reflected part of incoming radiation}}{\text{total incoming radiation}} \\
&\text{Absorptance,} && \alpha_w \equiv \tfrac{i_\alpha}{i_{in}} = \frac{\text{absorbed part of incoming radiation}}{\text{total incoming radiation}} \\
&\text{Transmittance,} && \tau_w \equiv \tfrac{i_\tau}{i_{in}} = \frac{\text{transmitted part of incoming radiation}}{\text{total incoming radiation}}
\end{aligned} \tag{2.16}$$

Note that the subscript "w" denotes that it concerns a property of a wall and must not be confused with properties of a medium. However, since all the radiation falling on the wall must either be reflected, absorbed or transmitted the following statement holds:

$$\rho_w + \alpha_w + \tau_w = 1 \tag{2.17}$$

If the wall, or medium, is sufficiently thick to be opaque, $\tau_w = 0$ and equation (2.17) reduces to:

$$\rho_w + \alpha_w = 1 \tag{2.18}$$

Reflection

In general, reflection on a wall is a mixture of partly specular and partly diffuse reflection. The characteristic mixture of reflection depends, among other things, on the reflective properties of the wall and the angle of incidence. For simplicity, this reflection behavior of a wall or material transition is taken independently of the angle of incidence and is shown schematically in Figure 2.3.

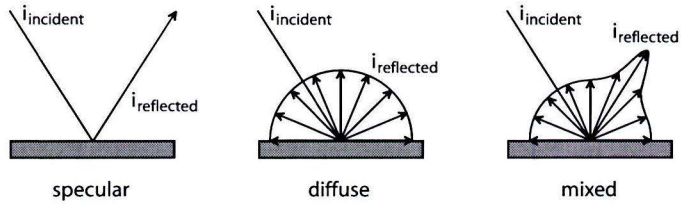

Figure 2.3: Specular, diffuse and mixed reflection against a wall

Effect of refractive index

The difference of refractive index has a significant effect on radiation crossing an interface of different materials. This effect results in a change in the magnitude of the intensity and a shift in wavelength, as is derived below.

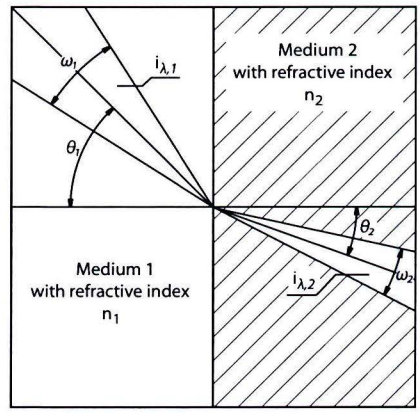

Figure 2.4: Radiation crossing an interface between media with different refractive index

Consider radiation travelling through a medium of refractive index n_1. Let the radiation with intensity $i_{\lambda,1}$ in solid angle $d\omega_1$ pass into a medium of refractive index n_2 as shown in Figure

2.4. The part from the radiation with intensity $i_{\lambda,1}$ with solid angle $d\omega_1$ at incidence angle θ_1 which is transmitted through the interface passes into solid angle $d\omega_2$ with intensity $i_{\lambda,2}$ at angle of refraction θ_2. Taking reflection into account the conservation of energy at the interface is given by:

$$i_{\lambda,1}(\lambda_1)[1-\rho_\lambda(\theta_1)]\ \cos\theta_1 dA d\omega_1 d\lambda_1 = i_{\lambda,2}(\lambda_2)\cos\theta_2 dA d\omega_2\ d\lambda_2 \tag{2.19}$$

with $\rho_\lambda(\theta_1)$ the directional-hemispherical reflectivity of the interface and $\cos\theta_1 dA$ the projected surface area from the area element dA in the plane of the interface. As the increment of circumferential angle φ is unchanged crossing the interface, substitution of the relation for solid angle, $d\omega = \sin\theta d\theta d\varphi$ gives:

$$i_{\lambda,1}(\lambda_1)[1-\rho_\lambda(\theta_1)]\ \sin\theta_1\cos\theta_1 d\theta_1 d\lambda_1 = i_{\lambda,2}(\lambda_2)\sin\theta_2\cos\theta_2 d\theta_2\ d\lambda_2 \tag{2.20}$$

Snell's law relates the indices of refraction to the angles of incidence and refraction:

$$\frac{n_1}{n_2} = \frac{\sin\theta_2}{\sin\theta_1} \tag{2.21}$$

Differentiation of equation (2.21) yields:

$$n_1\frac{d(\sin\theta_1)}{d\theta_1}d\theta_1 = n_2\frac{d(\sin\theta_2)}{d\theta_2}d\theta_2 \tag{2.22}$$

Substitution of 2.22 in equation (2.20) gives the rate of change in intensity for radiation crossing an interface:

$$\frac{i_{\lambda,1}(\lambda_1)}{i_{\lambda,2}(\lambda_2)} = \frac{1}{[1-\rho_\lambda(\theta_1)]}\ \frac{{n_1}^2}{{n_2}^2}\ \frac{d\lambda_2}{d\lambda_1} \tag{2.23}$$

The frequency ν is related to wavelength through:

$$\nu = \frac{c_0}{n\lambda} \tag{2.24}$$

Since the frequency of radiation does not change while crossing an interface, it can be shown that the rate of change in wavelength for radiation crossing an interface is given by:

$$\frac{\lambda_1}{\lambda_2} = \frac{n_2}{n_1} \tag{2.25}$$

Effect of angle for total reflection

Radiation crossing an interface between media with different refractive indices is limited, as a result of the effect of angle for total reflection.

Consider radiation travelling through a medium with refractive index n_1 and diffuse intensity i_1 as shown in Figure 2.5. Suppose that this diffuse intensity is incident upon the boundary from a medium with refractive index $n_2 > n_1$. Radiation incident at angles $0 \leq \theta_1 < 90\,^\circ$ is refracted into medium 2 at a maximum value of θ_2 given by:

$$\sin\theta_{2,\max} = \frac{n_1}{n_2}\sin 90\,^\circ = \frac{n_1}{n_2} \tag{2.26}$$

Consider a volume element dV inside medium 2. This volume element can only receive refracted radiation from medium 1 at angular directions within the range $0 \leq \theta_2 \leq \theta_{2,\max}$, with $\theta_{2,\max} = \sin^{-1}(n_1/n_2)$. Reversely only radiation at angular directions within the range $0 \leq \theta_2 \leq \theta_{2,\max}$ can enter medium 1. For incident angles on the interface from medium 2 towards medium 1 in excess of $\theta_{2,\max}$, the radiation is totally, internally reflected. Hence $\theta_{2,\max}$ is the angle of total internal reflection.

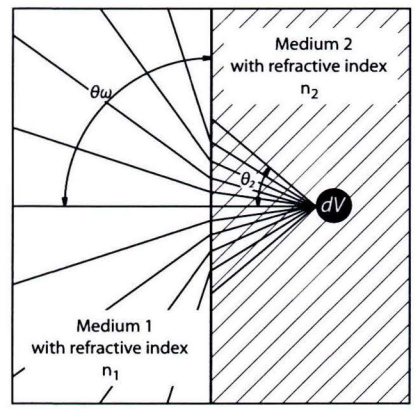

Figure 2.5: Effect of the angle for total reflection on radiation crossing an interface between media with differen refractive index

2.2.4 Emissivity

As seen in section 2.2.1 , a blackbody is a defined as a perfect emitter and absorber. However in general radiation problems, often real bodies are examined instead of black bodies. Since blackbody radiation is a helpful tool in radiation problems the radiation properties of a real body are related to that of a blackbody by the use of emissivity. It specifies how well a real body radiates energy compared to a blackbody. Emissivity can depend on factors as body temperature, wavelength of the emitted energy and angle of emission. Depending on the type of radiation problem, different emissivities may be required. We distinguish four different definitions of the emissivity: the directional spectral emissivity, the directional total spectral emissivity, the hemispherical spectral emissivity and the hemispherical total emissivity. Here, total and hemispherical stands for values averaged with respect to all wavelengths, respectively values averaged with respect to all directions.

Directional spectral emissivity

Directional spectral emissivity is the most fundamental emissivity, because it includes dependencies on wavelength, direction and surface temperature. Consider a geometry as shown in Figure 2.6. The radiation intensity is the energy per unit of time emitted in direction (θ, φ) per unit of projected area dA normal to this direction, per unit of solid angle and per unit wavelength interval. Note that for a blackbody the emitted intensity is independent of direction unlike the intensity of a real body.

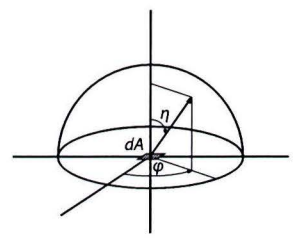

Figure 2.6: Hemisphere with emitting surface dA

The directional spectral emissivity is defined as:

$$\varepsilon(\lambda, \theta, \varphi, T) = \frac{i_\lambda(\lambda, \theta, \varphi, T)}{i_{\lambda b}(\lambda, T)} \tag{2.27}$$

with T the surface temperature.

Directional total emissivity

The directional total emissivity with respect to radiation emitted in the (θ, φ)-direction, can be obtained by averaging the directional spectral intensity over all wavelengths:

$$i(\theta, \varphi, T) = \int_0^\infty i_\lambda(\lambda, \theta, \varphi, T) d\lambda \tag{2.28}$$

where the total intensity for a blackbody is:

$$i_b(T) = \int_0^\infty i_{\lambda b}(\lambda, T) d\lambda = \frac{\sigma T^4}{\pi} \tag{2.29}$$

The directional total emissivity is defined as the ratio of $i(\theta, \varphi, T)$ for the real surface to $i_b(T)$ emitted by a blackbody:

$$\varepsilon(\theta, \varphi, T) = \frac{i(\theta, \varphi, T)}{i_b(T)} = \frac{\pi \int_0^\infty i_\lambda(\lambda, \theta, \varphi, T) d\lambda}{\sigma T^4} \tag{2.30}$$

Note that $i_\lambda(\lambda, \theta, \varphi, T)$ can also be expressed as:

$$i_\lambda(\lambda, \theta, \varphi, T) = \varepsilon_\lambda(\lambda, \theta, \varphi, T) i_{\lambda b}(\lambda, T) \tag{2.31}$$

Hemispherical spectral emissivity

The spectral radiation emitted by a unit surface area into all directions of a hemisphere is the hemispherical spectral emissive power, that is:

$$e_\lambda(\lambda, T) = i_{\lambda b}(\lambda, T) \int_{\varphi=0}^{2\pi} \int_{\theta=0}^{\pi/2} \varepsilon_\lambda(\lambda, \theta, \varphi, T) \cos\theta \sin\theta d\theta d\varphi \tag{2.32}$$

For a blackbody, the hemispherical spectral emissive power, is given by $e_{\lambda b}(\lambda, T) = \pi i_{\lambda b}(\lambda, T)$. The hemispherical spectral emissivity is then given by:

$$\varepsilon(\lambda, T) = \frac{e_\lambda(\lambda, T)}{e_{\lambda b}(\lambda, T)} = \frac{1}{\pi} \int_{\varphi=0}^{2\pi} \int_{\theta=0}^{\pi/2} \varepsilon_\lambda(\lambda, \theta, \varphi, T) \cos\theta \sin\theta d\theta d\varphi \tag{2.33}$$

Hemispherical total emissivity

The hemispherical total emissivity is the hemispherical spectral emissivity integrated over all wavelengths. It can be expressed in terms of the directional spectral emissivity, the directional total emissivity or in the hemispherical spectral emissivity. Here, the hemispherical total emissivity is only given in terms of the directional total emissivity:

$$\varepsilon(T) = \frac{1}{\pi} \int_{\varphi=0}^{2\pi} \int_{\theta=0}^{\pi/2} \varepsilon(\theta, \varphi, T) \cos\theta \sin\theta d\theta d\varphi \tag{2.34}$$

2.3 Applicability radiation models

For the simulation of the radiative heat transfer, the applicability in the gobform model of different radiation models has been investigated. These models are the Rosseland approximation, non-spectral Discrete Ordinate Method (D.O.M.) and the improved diffusion approximation of Lentes and Siedow. The latter two models are not yet applicable in simulations with a material interface as in the gobforming model. The adaptation of one of these models for a gobform simulation is out of the scope of this research. Moreover, in the gobform model the material transition is simulated with a moving free surface, further complicating the adaptation. Therefore, for more information about the Discrete Ordinate Method or the improved diffusion approximation of Lentes and Siedow, the reader is referred to [4], respectively [5].

Rosseland approximation

In the Rosseland approximation model, the radiative heat transfer is approximated with a radiative heat conduction coefficient, as discussed in [2]. This coefficient can easily be added in the conservation of energy equation, thus describing the contribution of the radiation. Therefore the Rosseland approximation is used in the gobform model. Here a distinction is made between the internal radiative heat transfer in the gob and the radiative heat transfer to the surroundings. The Rosseland approximation can only be used in the glass domain for the simulation of the internal radiative heat transfer. Therefore two different methods are developed for implementation of the radiative heat transfer to the surroundings. The implementation of the total radiative heat transfer in the gobform model is discussed in section 3.6. Here the validity range of the Rosseland approximation, as discussed below, has to be taken into account.

Validity range of the Rosseland approximation

In the Rosseland approximation, the glass is assumed optically thick. This means that complete absorption is assumed within the glass domain. The absorptance of the radiation in one direction is given by:

$$\alpha = 1 - e^{-\kappa S} \tag{2.35}$$

with κ the extinction coefficient of the glass and S the distance. Following [6], the Rosseland approximation cannot be used, if more then 10% of the radiation is transmitted. This results in the restriction $\alpha > 0.9$ so that:

$$\kappa S > 2.3 \tag{2.36}$$

This yields to a validation range of the Rosseland approximation as shown in Figure 2.7.

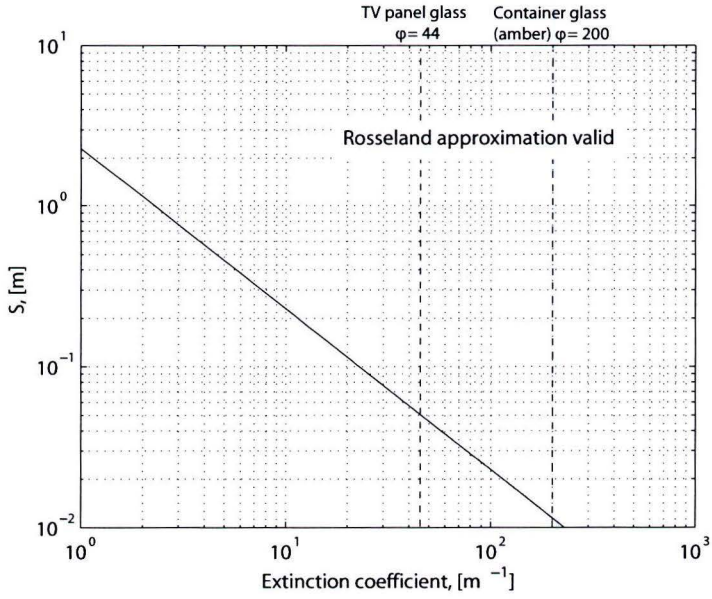

Figure 2.7: Validity range of the Rosseland approximation

It can be seen that, for example, container glass (amber) with an extinction coefficient of about $200m^{-1}$, the Rosseland approximation is valid from a glass thickness of about $1.2cm$. For TV panel glass with an extinction coefficient of about $44m^{-1}$, the use of the Rosseland approximation is valid from a thickness of about $5cm$.

2.4 Discussion

At $T = 1000$, The heat transfer in the gobform process is dominated by radiation and convection. In the heat transfer from the gob to the surroundings, the maximum contribution of the convection in the air film surrounding the gob is approximately 6% compared to the radiative heat transfer. The basic radiative heat transfer principles are discussed and some of the interfacial effects are given. Known radiation models based on the DOM-method are not yet able to deal with a moving free surface. Therefore in the gobform model, a Rosseland approximation is used in the implementation of the internal heat transfer in the gob. The validation range of the Rosseland approximation is calculated for a 90% absorption criterium. For the implementation of the heat transfer to the environment, two different methods are developed which are discussed in the next chapter.

Chapter 3

The gobform model

3.1 Introduction

The goal of this research is a model which can predict shape and temperature profiles in a glass gob during the gobforming process. The gobform process simulation is essentially a flow problem combined with an energy problem. The main difficulties in the simulation arise from the modelling of the glass surface. The glass surface is a boundary which acts as a moving free surface of which the position has to be determined as part of the solution procedure.

There are several methods which can be used to determine the position of the glass surface. In general these can be divided in adaptive grid methods and non-adaptive grid methods. In an adaptive grid method the computational domain is adapted to the calculated solution at every time-step. The elements can move freely, since the nodal points are not fixed. The main advantage of this method is the ability to define the glass surface as the boundary of the domain. Hence, the boundary conditions of the glass gob during the forming process can be directly described at the glass surface. The main disadvantage of this method is that as the elements move freely with the solution, they are distorted and remeshing has to occur. The remeshing procedure is very time-consuming, since the distribution and number of elements are redefined. To keep computational time as low as possible, a non-adaptive grid method is chosen. In a non-adaptive grid method, the elements and nodal points are fixed, so that the necessity for a remeshing procedure is ruled out. A disadvantage of this method is that the gob only partly occupies the computational domain, making it impossible to apply the boundary conditions directly on the glass surface. Furthermore, special care has to be taken to define the position of the glass surface, and hence the transition in material properties and conditions.

The position of the glass surface is determined by a pseudo-concentration method [7]. The essence of this method is that the distinction of glass and air in the grid is made by labelling the computational points with a material label c, which is given the value $c = 1$ for glass and $c = 0$ for air. This material label is continuous, it can be determined locally in the total domain and it determines the material properties used in the calculation of the flow. The glass surface is determined by the iso-value line for $c = 0.5$. To keep track of this interface, the material labels are convected with the fluid velocity and the material properties are updated at every time step. As a result of the pseudo-concentration method, the gobform process simulation is a combined flow, (material) convection and energy problem.

This chapter has the following structure. First, the governing equations describing the phenomena appearing in the gobforming process are discussed in section 3.2. In section 3.3, the governing equations are rewritten in dimensionless form for the evaluation of the importance of these phenomena on the basis of dimensionless numbers. In the gobform model, three different problems are distinguished: the flow problem, the material convection problem and the temperature problem. They are discussed separately in section 3.4, 3.5 and 3.6, respectively. In these sections, the terms of the governing equations are evaluated, and the implementation of the initial

and boundary conditions and the numerical methods are discussed. Finally, in section 3.7 an overview is given of the structure of the gobform model.

3.2 Governing equations

As discussed above the model of the gobform process is a combined flow, material convection and energy problem. The flow can be described with the conservation equations for mass and momentum, respectively:

$$\frac{\partial \rho}{\partial t} + (\boldsymbol{\nabla} \cdot \rho \mathbf{u}) = 0 \tag{3.1}$$

$$\rho \frac{\partial \mathbf{u}}{\partial t} + \rho \left(\mathbf{u} \cdot \boldsymbol{\nabla}\right) \mathbf{u} = \; -\boldsymbol{\nabla} p + \rho \mathbf{g} + \eta \boldsymbol{\nabla}^2 \mathbf{u} \tag{3.2}$$

with ρ the density, $\mathbf{u}$ the velocity vector, p the pressure, $\mathbf{g}$ the gravitation vector, η the viscosity and t denotes time. The material convection problem is described by a, 'conservation of identity', convection equation:

$$\frac{\partial c}{\partial t} + \mathbf{u} \cdot \boldsymbol{\nabla} c = 0 \tag{3.3}$$

with c a material label. This convection equation states that the identity of a material particle, labelled with a value c, does not change. The temperature problem can be described with the conservation of energy equation:

$$\rho c_p \left(\frac{\partial T}{\partial t} + \mathbf{u} \cdot \; \boldsymbol{\nabla} T \right) = k \boldsymbol{\nabla}^2 T \; - \boldsymbol{\nabla} \cdot \mathbf{q_r} \tag{3.4}$$

with c_p the specific heat capacity, T the temperature, k the thermal conductivity and $\mathbf{q_r}$ the radiation heat flux vector.

3.3 Non-dimensionalization

To characterize and to evaluate the system of equations (3.1) to (??), the different terms are written in non-dimensional form, using the following variables:

$$\begin{array}{cccc} \mathbf{u}^* = \frac{\mathbf{u}}{U} & , & t^* = \frac{t}{\tau} & , \quad p^* = \frac{p}{p_{ref}} \quad , \quad \mathbf{g}^* = \frac{\mathbf{g}}{g} \\ \boldsymbol{\nabla}^* = L \boldsymbol{\nabla} & , & T^* = \frac{T - T_0}{\Delta T} & , \quad q^* = \frac{q_r}{q_{ref}} \end{array} \tag{3.5}$$

with the characteristic reference quantities U, τ, p_{ref}, g, L, ΔT and q_{ref}. The superscript "*" denotes the dimensionless form. For a gobform problem, the maximum outflow velocity of the glass at the spout orifice is chosen as the reference velocity U. The characteristic time τ is related to the timescale in which velocity fluctuations of order U occur. The reference quantity g is the gravitational force. As characteristic length L, the length of the gob is chosen. The typical temperature reference, ΔT, is the initial temperature difference between the glass and the ambient temperature. The values for a typical gobforming process are shown in Table 3.1. The pressure is made dimensionless with a reference pressure p_{ref}, which is evaluated for the glass and air medium separately in section 3.4. The reference radiation heat flux q_{ref} is discussed below.

The maximum radiative heat flux q_r is expressed as:

$$q_r \cong \sigma \left({T_{gob}}^4 - {T_\infty}^4 \right) \tag{3.6}$$

with σ the Stefan-Boltzmann constant, T_{gob} the temperature of the gob and T_∞ the ambient temperature. Combining the dimensionless expression for the temperature in (3.5) with equation (3.6) gives:

$$\begin{aligned} q_r \; &\cong \sigma \left({T_{gob}}^4 - {T_\infty}^4 \right) \\ &= \sigma ({T_{gob}}^2 + {T_\infty}^2)(T_{gob} + T_\infty) \; (T_{gob} - T_\infty) \\ &= \sigma ({T_{gob}}^2 + {T_\infty}^2)(T_{gob} + T_\infty) \; \Delta T ({T_{gob}}^* - {T_\infty}^*) \end{aligned} \tag{3.7}$$

Table 3.1: Characteristic values of the gobform process variables

variable	unit	characteristic value	
		glass	air
ρ	$\frac{kg}{m^3}$	10^3	1
c_p	$\frac{J}{kg.K}$	10^3	10^3
η	Pa.s	10^3	10^{-5}
k	$\frac{W}{m.K}$	1	10^{-2}
T_0	K	10^3	10^2
g	$\frac{m}{s^2}$	10	
L	m	$10^{-2} - 10^{-1}$	
U	$\frac{m}{s}$	10^{-2}	
ΔT	K	10^3	
σ	$\frac{W}{m^2.K}$	10^{-8}	

The temperature of the gob is written as $T_{gob} = T_0 + \Delta T_{gob}$ with T_0 the initial glass temperature and ΔT_{gob} the temperature difference in the gob during gob formation. Since $\Delta T_{gob} and T_\infty << T_{gob}$, we can approximate the dimensional part of equation 3.7, resulting in:

$$\begin{aligned} \left({T_{gob}}^2 + {T_\infty}^2\right)\ \left(T_{gob} + T_\infty\right) = \\ {T_{gob}}^3 + {T_{gob}}^2 T_\infty + {T_\infty}^2 T_{gob} + {T_\infty}^3 \approx {T_0}^3 \end{aligned} \tag{3.8}$$

Finally, this leads to the reference radiative heat flux q_{ref} defined as:

$$q_{ref} = \sigma \Delta T {T_0}^3 \tag{3.9}$$

With 3.5, the non-dimensional set of equations becomes:

$$Sr \frac{\partial \rho}{\partial t^*} + \boldsymbol{\nabla}^* \cdot (\rho \mathbf{u}^*) = 0 \tag{3.10}$$

$$Sr \frac{\partial \mathbf{u}^*}{\partial t^*} + (\mathbf{u}^* \cdot \boldsymbol{\nabla}^*)\, \mathbf{u}^* = -\frac{p_{ref}}{\rho U^2} \boldsymbol{\nabla}^* p^* + \frac{1}{Fr} \mathbf{g}^* + \frac{1}{Re} \boldsymbol{\nabla}^{*2} \mathbf{u}^* \tag{3.11}$$

$$Sr \frac{\partial c}{\partial t^*} + \mathbf{u}^* \cdot \boldsymbol{\nabla}^* c = 0 \tag{3.12}$$

$$\frac{1}{Fo} \frac{\partial T^*}{\partial t^*} + Pe \mathbf{u}^* \cdot \boldsymbol{\nabla}^* T^* = \boldsymbol{\nabla}^{*2} T^* - \frac{1}{M} \boldsymbol{\nabla}^* \cdot {q_r}^* \tag{3.13}$$

The non-dimensional numbers used in the equations are defined as:

$$\begin{aligned} Re = \frac{\rho U L}{\eta} \quad , \quad Fr = \frac{U^2}{gL} \quad , \quad Sr = \frac{L}{U\tau} \quad , \quad Pr = \frac{c_p \eta}{k} \\ Pe = RePr = \frac{\rho c_p U L}{k} \quad , \quad Fo = \frac{1}{PeSr} = \frac{\rho c_p L^2}{k\tau} \\ M = \frac{k}{\sigma {T_0}^3 L} \end{aligned} \tag{3.14}$$

with Re the Reynolds number, Fr the Froude number, Sr the Strouhal number, Pr the Prandtl number, Pe the Peclet number, Fo the Fourier number and M a conduction-radiation parameter. Here, M depicts the proportion of conductive to radiative energy transport. The evaluation of the non-dimensional set of equations is discussed separately for the flow, material convection and temperature problem in section 3.4 to 3.6, respectively.

3.4 Flow problem

The starting points for the modelling of the flow are the dimensionless conservation of mass and conservation of momentum equations, (3.10) and (3.11). The evaluation of the different terms in these equations are discussed separately for glass and air, because of the difference in material properties. Furthermore, the boundary conditions, the initial condition and the numerical method used are specified.

3.4.1 Glass domain

The flow in the glass is assumed incompressible. This leads to a time-independent continuity equation.

For the dimensionless conservation of momentum equation (3.11), the relevant dimensionless numbers are the Reynolds, Froude and Strouhal numbers. With the characteristic values for the gobform process in Table 3.1, the Reynolds and Froude number can be determined as:

$$Re = \mathcal{O}(10^{-4} - 10^{-3}) \tag{3.15}$$

$$Fr = \mathcal{O}(10^{-4} - 10^{-3}) \tag{3.16}$$

depending on the size of the gob resulting in a characteristic goblength varying between $L = \mathcal{O}(10^{-2} - 10^{-1})$. The characteristic time τ is related to the time scale in which velocity fluctuations of order U occur. In the gobform process, such velocity fluctuations only occurs immediately at start-up of each gobform cycle, as the gobber starts to translate downwards. However, the point of interest does not lie in the start-up phenomena and typical time scales of a gobform process vary between $\tau = \mathcal{O}(0.1 - 10sec)$. Consequently, this results in a Strouhal number:

$$Sr = \mathcal{O}(1 - 10) \tag{3.17}$$

To determine the characteristic value for the pressure, p_{ref}, first the characteristic value for the gob length has to be evaluated. For relatively small gobs, $L = \mathcal{O}(10^{-2})$, the pressure in the glass is determined by viscous stresses. For relatively large gobs, $L = \mathcal{O}(10^{-1})$, the pressure is determined by hydrostatic stresses. Therefore, in glass the characteristic value for the pressure is chosen as:

$$\begin{array}{lll} \text{for } L = 10^{-2} & : & p_{ref} = \frac{\eta U}{L} \\ \text{for } L = 10^{-1} & : & p_{ref} = \rho g L \end{array} \tag{3.18}$$

Together with equations (3.10), (3.11) and the dimensionless numbers (3.15) to (3.17) this yields to a time independent continuity equation and a stationary Stokes equation:

$$\boldsymbol{\nabla} \cdot \mathbf{u} = 0 \tag{3.19}$$

$$-\boldsymbol{\nabla} p + \rho \mathbf{g} + \eta \boldsymbol{\nabla}^2 \mathbf{u} = 0 \tag{3.20}$$

3.4.2 Air domain

In the gob forming process, the gob is surrounded by air. In the air domain, the characteristic values from Table 3.1 give a Reynolds and Froude number of:

$$Re = 10^2 \tag{3.21}$$

$$Fr = 10^{-3} \tag{3.22}$$

Since the viscous forces can be neglected, and together with the characteristic pressure defined as:

$$p_{ref} = \rho U^2 \tag{3.23}$$

this will lead for the conservation of momentum equation (3.11) to the non-linear equation:

$$(\mathbf{u}^* \cdot \nabla^*)\mathbf{u}^* = -\nabla^* p^* + \frac{1}{Fr}\mathbf{g}^* \tag{3.24}$$

However our interest does not lie in the air domain. Therefore the air is replaced with a fictitious fluid, of which the viscosity is of the order of 10^{-3} times the order of the glass viscosity, but with the same mass density as the air. This reduces the Reynolds number for the air domain to $Re = \mathcal{O}(10^{-3})$, so that the stationary inertia terms in equation (3.11) can be neglected, while the pressure drop is still negligibly small compared to the pressure drop in the glass domain, thereby preserving the interaction between the glass and the air flow. This again leads to the time independent continuity equation and the stationary Stokes equation, equations (3.19) and (3.20):

$$\nabla \cdot \mathbf{u} = 0$$

$$-\nabla p + \rho \mathbf{g} + \eta \nabla^2 \mathbf{u} = 0$$

with the advantage that now the equations for the flow problem in the glass and "air" domain are the same. In this thesis, the material surrounding the gob will further be denoted as the fictitious fluid.

3.4.3 Boundary conditions

In the gobform model the gobform process is simulated axisymmetrically. Therefore a cylindrical co-ordinate system is used with co-ordinates r, φ and z. The velocity components are thus described as u_r, u_φ and u_z. Since the flow is considered axisymmetric and rotation free, $\frac{\partial}{\partial \varphi} = 0$ and $u_\varphi = 0$. The remaining boundary conditions are shown in Figure 3.1.

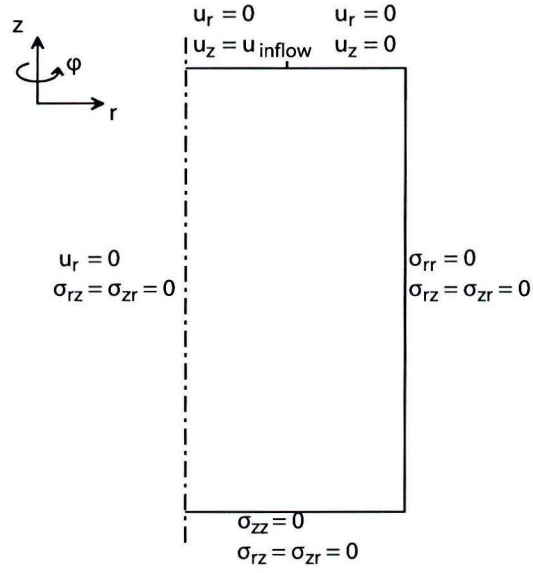

Figure 3.1: Boundary conditions flow problem

with the components of the stress tensor σ defined as:

$$\begin{aligned} \sigma_{rr} &= -p + 2\eta \frac{\partial u_r}{\partial r} \\ \sigma_{zz} &= -p + 2\eta \frac{\partial u_z}{\partial z} \\ \sigma_{rz} = \sigma_{zr} &= \eta\left(\frac{\partial u_r}{\partial z} + \frac{\partial u_z}{\partial r}\right) \end{aligned} \tag{3.25}$$

3.4.4 Interfacial conditions

The boundary conditions that determine the flow at the interface are immiscibility and conservation of momentum. The immiscibility condition is already satisfied by equation (3.3), in which the conservation of identity is guaranteed. The conservation of momentum at the interface, [7], is expressed as:

$$(\boldsymbol{\sigma}_2 - \boldsymbol{\sigma}_1) \cdot \mathbf{n}_{12} = \gamma_{12}\kappa\, \mathbf{n}_{12} \tag{3.26}$$

in which σ denotes the surface tension, subscripts $_1$ and $_2$ the glass and the fictitious fluid respectively, γ the interfacial tension, κ the interface curvature and $\mathbf{n}_{12}$ the normal vector to the interface. Introducing dimensionless variables, equation (3.26) can be written as:

$$(\boldsymbol{\sigma}_2^* - \boldsymbol{\sigma}_1^*) \cdot \mathbf{n}_{12}^* = \frac{1}{Ca}\, \gamma_{12}^*\kappa^*\, \mathbf{n}_{12}^* \tag{3.27}$$

in which the non-dimensional Capillary number is defined as:

$$Ca = \frac{\eta U}{\gamma} \tag{3.28}$$

For the gobforming process, the Capillary number, with $\gamma = \mathcal{O}(10^{-1})\frac{N}{m}$ following [2], is of the order 10^2. This indicates that the interfacial forces can be neglected and equation (3.26) reduces to:

$$\boldsymbol{\sigma}_2 - \boldsymbol{\sigma}_1 = \mathbf{0} \tag{3.29}$$

This condition is already satisfied by equation (3.2), since the material properties are continuous functions of c at the interface.

3.4.5 Numerical method

The model has been implemented in the finite element package SEPRAN. To solve the continuity equation, (3.19), and the Stokes equation, (3.20), a standard Galerkin finite element method is used. After spatial discretisation the system of equations is:

$$\mathbf{LU} = \mathbf{0} \tag{3.30}$$

$$\mathbf{SU} - \mathbf{L}^T\mathbf{P} = \mathbf{F} \tag{3.31}$$

in which:

$$\mathbf{L}_{ij} = \int_\Omega \psi_i\, \boldsymbol{\nabla}\, \phi_i d\Omega \tag{3.32}$$

$$\mathbf{S}_{ij} = \int_\Omega \eta\, \boldsymbol{\nabla}\phi_i \cdot \boldsymbol{\nabla}\phi_j\, d\Omega \tag{3.33}$$

$$\mathbf{F}_j = \int_\Omega \rho g \phi_j d\Omega + \int_\Gamma \Big(\sigma_{nn}(\phi_j \cdot n) + \sigma_{nt}(\phi_j \cdot t)\Big) d\Gamma \tag{3.34}$$

with ϕ_i and ψ_i the shape functions for respectively the velocity and the pressure, σ_{nn} and σ_{nt} components of the stress tensor as defined in appendix B, Ω the computational domain and Γ the boundary of this domain.

In the system of equations, equation 3.30 and 3.31, $\mathbf{U}$ denotes the vector of the velocity unknowns, $\mathbf{P}$ denotes the vector of the pressure unknowns, $\mathbf{SU}$ denotes the discretization of the viscous terms, $\mathbf{LU}$ denotes the discretization of the divergence of $\mathbf{u}$ and $-\mathbf{L}^T\mathbf{P}$ denotes the discretization of the gradient of p. The right hand vector $\mathbf{F}$ contains the contributions of the gravitational force, the boundary integral as well as the prescribed boundary conditions.

The elements used are linear triangles based on Taylor-Hood elements with continuous pressure, restricted to the integrated solution method only. The system of equations is solved by an integrated method, employing both velocities and pressures as unknowns, in combination with an iterative solver.

Linear elements are chosen because the material parameters are initially defined as discontinuous functions of the material labels. As an example, the viscosity depends on the material label c, as follows:

$$\eta = \eta(c) \begin{cases} \eta_{\text{glass}} & \text{if} \quad c \geq 0.5 \\ \eta_{\text{fictitious fluid}} & \text{if} \quad c < 0.5 \end{cases} \tag{3.35}$$

If quadratic elements had been used, the quadratic shape functions could give negative values of the material property at the integration points of the element as shown in Figure 3.2.

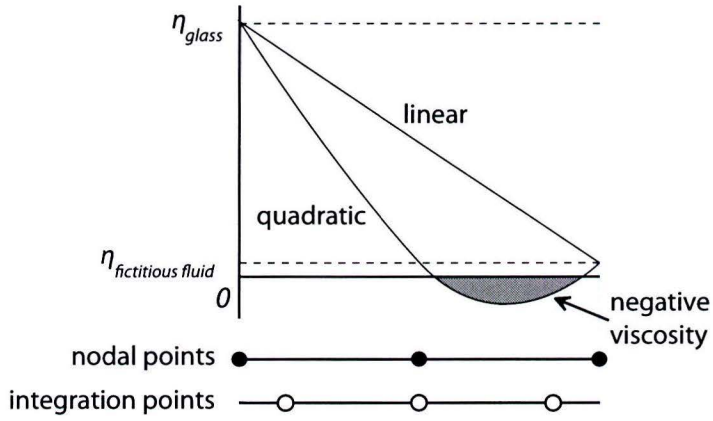

Figure 3.2: Effect of linear and quadratic interpolation of viscosity over an element

3.5 Material label convection problem

3.5.1 Entire domain

The material label convection problem is used to distinguish glass from the fictitious fluid representing air. The material labels are convected through the domain with velocity $\mathbf{u}$. The 'identity' of the label is preserved according to equation (3.3).

To distinguish between glass, the fictitious fluid and the transition between the glass and the fictitious fluid, the so called flow front, the material label is defined as:

$$\begin{array}{ll} 0 \leq c < 0.5 & \text{fictituous fluid (air)} \\ 0.5 \leq c \leq 1 & \text{glass} \end{array} \tag{3.36}$$

with:

$$c = 0.5 \quad \text{flowfront (glass)} \tag{3.37}$$

The material properties can now be determined locally as a function of the material label, updated at every time step.

3.5.2 Initial and boundary conditions

The initial condition $c(t = 0)_\Omega$ defines the glass air distribution. For the gobform simulation, the entire domain is initially set to $c = 0$, the value for fictitious fluid, except at the spout orifice. At the spout orifice, glass enters the domain, thus the material label is set to $c = 1$, the value for glass. Without a prescription for the glass surface position, $c = 0.5$, the linear transition of the material parameter c over the elements at the spout would result in an element dependent position of the glass surface. Therefore the glass surface is explicitly prescribed in an material label distribution routine. In this distribution routine the material label value is calculated with

respect to the distance to the desired glass surface position. The boundary conditions are shown in Figure 3.3.

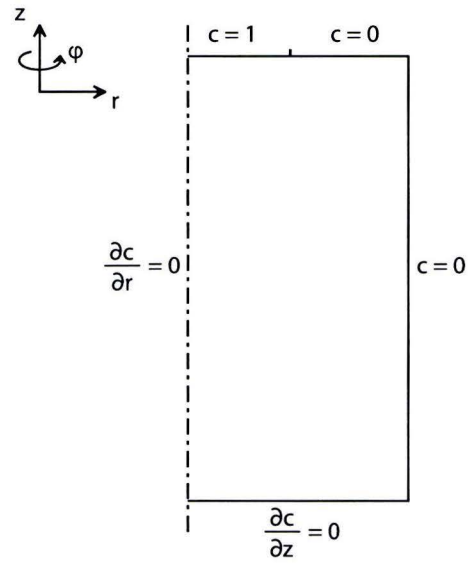

Figure 3.3: Boundary conditions material label problem

3.5.3 Numerical method

To solve the conservation of identity equation, (3.3), a standard Galerkin finite element method is used with a Streamline Upwind Petrov Galerkin (SUPG) scheme for time-dependent problems. After spatial discretisation the equation can be rewritten in the form:

$$\mathbf{M}\dot{c} + \mathbf{N}c = 0 \tag{3.38}$$

in which:

$$\mathbf{M}_{ij} = \int_{\Omega} \tilde{\phi}_i \, \phi_j d\Omega \tag{3.39}$$

$$\mathbf{N}_{ij} = \int_{\Omega} \mathbf{u} \cdot (\boldsymbol{\nabla}\phi_j) \, \tilde{\phi}_i d\Omega \tag{3.40}$$

with $\mathbf{M}$ the mass matrix, $\mathbf{N}$ the stiffness matrix, ϕ_j the classical shape function for the material parameter c and $\tilde{\phi}_i$ the test function extended for the upwinding part, defined as:

$$\tilde{\phi}_i = \phi_i + p_i \tag{3.41}$$

with p_i the time-dependent approximation. The time derivative in equation (3.38) is replaced by a forward difference discretization:

$$\dot{c} = \frac{c^{k+1} - c^k}{\Delta t} \tag{3.42}$$

where k denotes the present time level, $k+1$ denotes the next time level and Δt denotes the time-step size. To solve equation (3.38), a so-called θ-method is used in which $\theta = 0.5$ (Crank Nicolson). After every time step, the material labels are rounded off to either the value 1 or 0 everywhere, except in the elements containing the material interface $c = 0.5$.

For a more detailed discussion on the numerical method with regard to the time-dependent approximation and the numerical solver, the reader is referred to [8].

3.6 Temperature problem

The modelling of the temperature problem starts with the evaluation of the dimensionless numbers in equation (3.13) in the glass and the fictitious fluid domain. For the implementation of the radiation term $\nabla \cdot \mathbf{q_r}$, a distinction is made between internal radiation in the glass and radiation crossing the glass surface. For the internal radiation, a Rosseland conduction approximation is used. For the implementation of the radiation crossing the glass surface, two different methods are developed as discussed in section 3.6.3.

3.6.1 Glass domain

The relevant dimensionless numbers for the temperature problem in glass are the Fourier number, the Peclet number and the conduction-radiation parameter M. In the energy equation, the typical time scale in which the temperature changes in the order of it's magnitude is estimated to be $\tau = 100s$. With the characteristic values defined in Table 3.1, the dimensionless numbers and the conduction-radiation parameter are determined as:

$$Fo = \mathcal{O}(1 - 10^2) \tag{3.43}$$

$$Pe = \mathcal{O}(10^2 - 10^3) \tag{3.44}$$

$$M = \mathcal{O}(1 - 10) \tag{3.45}$$

With the given estimates, we conclude that, in glass, the energy equation is dominated by convection.

We will now discuss the implementation of the radiative heat transfer. This is the $\nabla \cdot \mathbf{q_r}$ term in the energy equation. In the gobform model, a distinction is made between the modelling of the internal radiative heat transfer in the gob and the radiative heat transfer of the gob to the surroundings. The radiative heat transfer to the surroundings is defined as the radiation crossing the glass surface, the glass to air interface in the computational domain. Since this is a moving free surface, this requires a special approach which is discussed in section 3.6.3. For the internal radiative heat transfer in the glass gob a Rosseland approximation is used following [2]. In this approximation the radiative heat transfer is approximated with a radiative heat conduction coefficient, k_r, given by:

$$k_r = \frac{16}{3} \frac{n^2 \sigma T^3}{\alpha} \tag{3.46}$$

with T the mean temperature in [K], σ the Stefan Boltzmann constant, n the refractive index and α the total, thus independent of wavelength, absorption coefficient. The absorption coefficient α can be determined with an empirical relation as a function of the composition of the glass, following [2]. The total heat transfer can now be described by an effective heat conduction coefficient, k_{eff}:

$$k_{\text{eff}} = k + k_r \tag{3.47}$$

with k the conduction coefficient.

For example, for float glass with 0.1 weight percentage Fe_2O_3 with approximately 10% of the ironoxide in Fe^{2+} state, the absorption coefficient $\alpha = 33.4m^{-1}$. This results in a temperature dependent effective heat conduction coefficient of $1.98 \times 10^{-8} T^3$. At 1000 °C, the initial glass temperature in the gobform model, the radiative heat conduction coefficient is then about $19.8 \frac{W}{mK}$. With a conduction coefficient of about $2.0 \frac{W}{mK}$, this gives an effective heat conduction coefficient of $21.8 \frac{W}{mK}$.

In the glass domain the temperature problem can thus be solved with:

$$\rho c_p \left(\frac{\partial T}{\partial t} + \mathbf{u} \cdot \nabla T \right) = k_{\text{eff}} \nabla^2 T \tag{3.48}$$

3.6.2 Air domain

In the gobform model, our interest lies in the glass domain only. In chapter 2, it is discussed how the heat transfer is dominated by radiation, so that the conductive heat transfer in the air can be neglected. The air is replaced by a fictitious fluid, as discussed in section 3.4. Therefore, we can adapt the energy properties of the fictitious fluid to suit the implementation requirements of the radiative heat transfer from the glass to the surroundings, as is discussed in section 3.6.3. In this implementation, the specific heat capacity c_p plays an important role. The value of the specific heat capacity is set to a low value $c_p = 1 \times 10^{-9} \frac{J}{kgK}$ compared to $c_p = 1200 \frac{J}{kgK}$ for glass, so that the fictitious fluid does not contain internal energy. As a result, the temperature of the fictitious fluid is coupled to the glass surface temperature. As a result the characteristic timescale is the same, thus $\tau = 100s$. The initial temperature of the fictitious fluid is set to the initial glass temperature. Since in air the radiative properties can be neglected, we can set up the following dimensionless numbers for the fictitious fluid:

$$Fo = \mathcal{O}(10^{-13} - 10^{-11}) \tag{3.49}$$

$$Pe = \mathcal{O}(10^{-15} - 10^{-14}) \tag{3.50}$$

From these dimensionless numbers, it will be clear that the temperature problem in the fictitious fluid is dominated by diffusion. We can now solve the temperature problem using equation (3.48) in the entire domain, with $k_r = 0$ in the air domain.

3.6.3 Gob surface radiation by TRH and IRH method

As discussed earlier, a distinction is made in the modelling of the internal radiative heat transfer of the gob and the radiative heat transfer of the gob to the surroundings. In this section, the implementation for the radiative heat flux to the surroundings is discussed. The magnitude of the heat flux is approximated using:

$$q_r = \sigma\varepsilon({T_{\text{glass}}}^4 - {T_{\text{ambient}}}^4) \tag{3.51}$$

with ε the total hemispherical emissivity, T_{glass} a uniform approximation for the glass gob temperature, and $T_{ambient}$ the temperature of the surroundings. Two different methods are developed for the implementation in the gobform model, namely the transposed radiation heat flux and the imposed radiation heat flux. These methods are further addressed as the TRH-method, respectively the IRH-method. Credit for the IRH-method goes to Gerard Haagh, a former employee of TNO, for the development and implementation in the gobform model.

Transposed radiation heat flux method

In the TRH-method, the radiative heat flux at the glass surface is transposed to a boundary of choice of the computational domain. For this, in SEPRAN, special boundary elements are implemented. The boundary condition used is of type 2, following [8]. The magnitude of the heat flux can now be prescribed as a Neumann boundary condition:

$$q_{\text{prop}} = \sum_{i=1}^{n}\sum_{j=1}^{n} k_{ij}\frac{\partial T}{\partial x_j}n_i \tag{3.52}$$

with q_{prop} the magnitude of the heat flux proportional to the ratio of the area of the glass surface and the boundary at which the heat flux is prescribed. At all other boundaries, the derivative of the temperature in the normal direction is zero.

The proportional heat flux now prescribed at a boundary of the computational domain, has to contribute as the radiative heat flux, q_r, at the glass surface. The glass surface and the prescribed boundary condition are separated by the fictitious fluid. By setting the internal heat capacity of the fictitious fluid to a small value, $c_p = 1 \times 10^{-9}$, in combination with the prescribed boundary conditions, the heat flux is thus transposed to the glass surface.

Imposed radiation heat flux method

In the IRH-method an expression of the $(\nabla \cdot \mathbf{q_r})$ term in equation (3.4) is derived and added as a source term at the glass surface. In this method, a SEPRAN levelset routine is used in which the grid locally at the glass surface is refined, at every time-step. This way, the glass surface coincides with the nodal points of the temporarily generated elements.

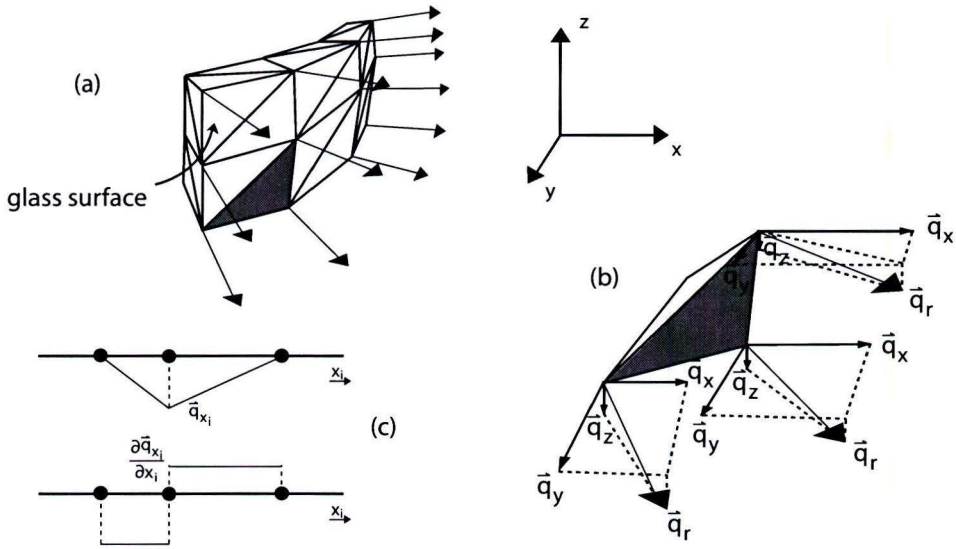

Figure 3.4: Prescription of the radiative heat flux at the glass surface: (a) glass surface elements distribution, (b) transformation of the heat flux in the normal direction of the glass surface to the coordinate system used (c) the derivation of the individual components in the divergence of the heat flux

Consider a glass surface distribution over 3D elements as shown in Figure 3.4 (a). In the IRH-method, the magnitude of the heat flux is prescribed as a heat flux vector on the glass surface pointing outward from the glass in the normal direction. To calculate the heat flux in the normal direction of the glass surface in terms of the directions of the coordinate system used, shown in Figure 3.4 (b), we first have to calculate the concentration gradient ∇c. Since the material label parameter in glass is higher then in the fictitious fluid the negative value of the concentration gradient has to be taken. The heat flux vector is then:

$$\vec{q_r} = q_r \frac{-\nabla c}{||\nabla c||} \tag{3.53}$$

Next the derivative of each component of $\vec{q_r}$ to the corresponding i-th co-ordinate, $\frac{\partial q_i}{\partial x_i}$ is calculated, as schematically shown in Figure 3.4 (c). Once the derivatives are determined, the divergence of the heat flux, $(\nabla \cdot \mathbf{q_r})$ can be calculated. We are only interested in the divergence of the heat flux in the glass. Therefore, only the negative part of the divergence of the heat flux is taken and added to the heat equation as a negative source term.

3.6.4 Initial and boundary conditions

In the air domain a fictive temperature problem is solved. Since the fictitious fluid here is designed to hold no internal energy the initial condition of the fictitious fluid is of minor importance. Immediately after the first time-step, the temperature in the fictituous fluid is determined by the glass surface temperature. Therefore the initial condition is set to the glass surface temperature at $t = t_0$. The boundary conditions of the temperature problem are given in Figure 3.5.

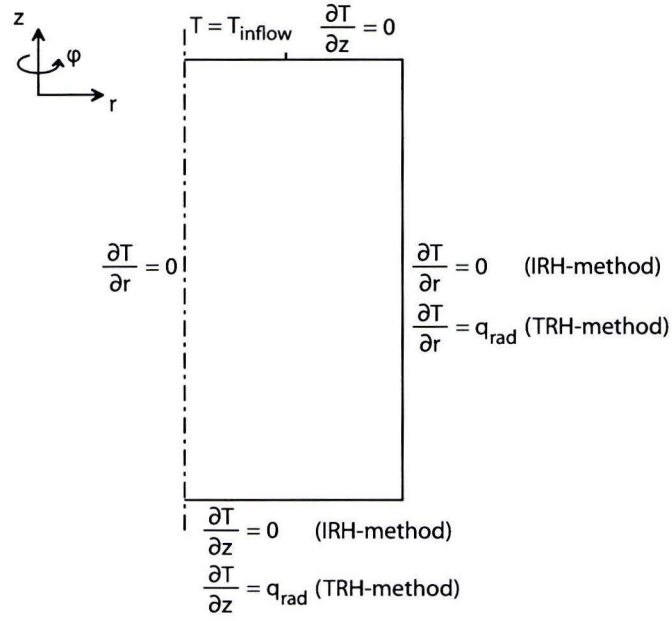

Figure 3.5: Boundary conditions temperature problem

3.6.5 Numerical method

The temperature problem is solved using equation (3.48). Similar to the material convection problem, a Galerkin finite element method is used with a SUPG scheme for time-dependent problems. The time derivative is replaced by a discretization scheme and solved with a so-called θ-method with $\theta = 0.5$ (Crank Nicolson).

A difference with the spatial discretization scheme given in section 3.5.3 is the contribution of the diffusion term $k\nabla^2 T$. Applying Gauss' theorem requires continuous functions. Since the SUPG scheme with test function $\tilde{\phi}_i = \phi_i + p_i$ is used, equation (3.41), Gauss' divergence theorem may only be applied to ϕ_i. Since the mathematical implementation procedure of the discretization is considered out of the scope of this Master's thesis, the discussion is therefore omitted.

3.7 Model structure

The model, as it is described in the previous sections, is implemented in the finite element package SEPRAN. The model structure is shown in Figure 3.6. After start-up, the input is read and the mesh is constructed. Then, all the vectors are initialized and the initial and boundary conditions are applied. These results are written to the output for $t = 0s$. Next the program starts the time loop in which first the time-step is raised. In the gobform model, first the Stokes problem is solved, then the material convection problem an finally the temperature problem. Once the material convection problem is solved, the material properties distribution is updated and the mesh is subdivided at the glass surface interface. In the model structure, a difference can be seen for the chosen implementation method for the radiative glass surface boundary condition. The use of the IRH-method, requires additional calculations for the derivation of the divergence of the radiative heat flux at the glass surface. After the temperature problem is solved, the temperature dependent viscosity is calculated and the temporary mesh subdivision is removed. After every time-step the results are written to the output file. After the final time-step the time-loop is aborted and the program is ended.

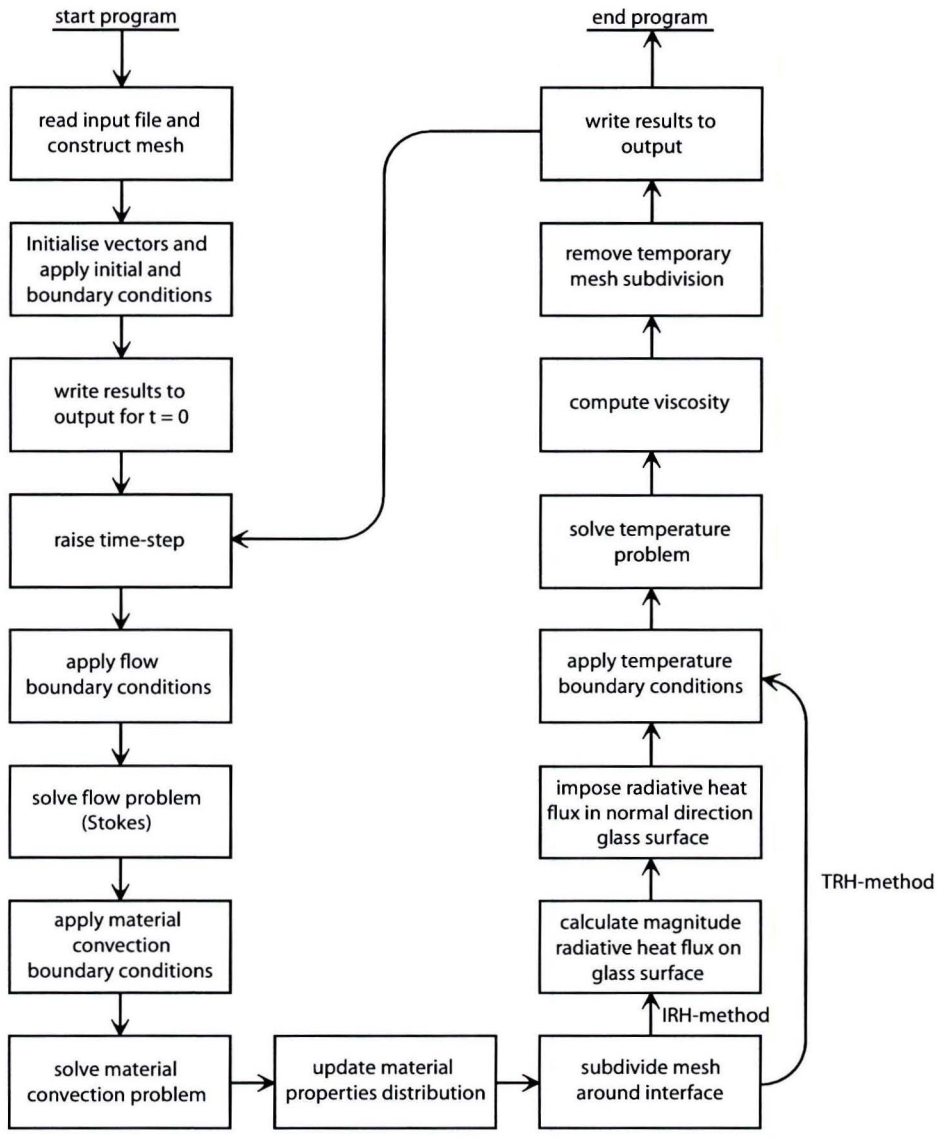

Figure 3.6: Schematical presentation of the model structure

Chapter 4

Determination of glass emissivity

In the gobform model, the magnitude of the radiative heat transfer to the surroundings is approximated by:

$$q = \sigma\varepsilon({T_{\text{gob}}}^4 - {T_{\text{ambient}}}^4) \tag{4.1}$$

with ε the emissivity. Since the heat transfer through the glass surface is directed in all directions outward of the gob the total hemispherical emissivity is required.

In this chapter, the determination of this emissivity, the experimental set-up and a detailed analysis of the experiment is discussed. The emissivity is derived from spectral energy measurements on glass at temperatures below the actual temperatures in a typical gobform process. The results are extrapolated to the required gobform temperature domain. This choice is based on the additional difficulties for emissivity measurements on molten glass, as discussed in section 4.1. The set-up of the experiment is discussed in section 4.2. In section 4.3, the method for the derivation of the total hemispherical emissivity is discussed. Then in section 4.4, an analysis of the experiment regarding the optical alignment, the spectral transformation factor, the ground intensity correction and the reproducibility is discussed. Finally in section 4.5, the determined emissivity of the float glass is discussed.

4.1 Temperature domain measurements on glass

In the experiments discussed here the radiative properties of the glass samples are measured at temperatures between $600 - 800\,^{\circ}\text{C}$, far below the temperatures of glass gobs during the gobform process, about $950 - 1000\,^{\circ}\text{C}$. This way, additional difficulties for measurements on molten glass can be avoided. At the lowered temperatures the glass is self-supporting and a glass sample only has to be supported at the edges. Consequently, the measurement beam is unaffected by any glass support system. To account for the temperature difference the results for the emissivity have to be extrapolated to higher temperatures. This extrapolation can also be translated to the assumption that for the derivation of the total hemispherical emissivity, the variation of the spectral absorption coefficient is negligible, as a result of the difference in temperature. This assumption is studied for the temperature domain from $600 - 1000\,^{\circ}\text{C}$ for float glass, and discussed in section 4.5.2. For typical examples of the spectral absorption coefficient of float glass at different temperatures, the reader is referred to [9].

Glass at temperatures between $950 - 1000\,^{\circ}\text{C}$ is in molten state and a special crucible should have been used to contain the glass melt. This crucible would have been positioned in the optical path of the measurement beam influencing the measured signal. Since a large contribution of the crucible bottom emission in the measurements of the glass must be prevented, either good reflective or transparent bottom properties are favorable. A more detailed description of radiative measurement experiments on glass melts can be found in [10] and [9].

In Nagtegaal, [10], a platinum disk is used to reflect the measurement beam back towards the glass surface, minimizing diffuse reflection of container wall emissions in the direction of the mea-

surement beam. Platinum is used because it is one of the few materials that does not chemically react with glass and has a higher melting point. Since the platinum disk itself also emits, resulting in a mean perpendicular emissivity of about $\varepsilon_m \approx 0.2$ at $1\mu m < \lambda < 4\mu m$, an additional requirement in this method is that the emissivity of the platinum disk has to be measured separately and has to be compensated. This is especially important in glass melt measurements at short wavelengths, where the glass has low absorptive properties. A practical consequence of the use of a platinum disk is that after every experiment, the disk has to be recovered and polished to ensure a smooth surface, and hence specular reflective properties.

A different approach is used in Nijnatten,[9], in which a sample holder is designed based on an Al_2O_3 crucible, with a sapphire window mounted in the center of the bottom. In this crucible, an Al_2O_3 tube having a sapphire window at the end is immersed into the glass melt. All together, this construction creates a controllable measurement volume between the two sapphire windows. A special positioning device was used for setting the optical path length trough the glass sample.

4.2 The experimental set-up

In the emissivity experiment, the radiation emitted by different glass samples at temperatures between 600−800 °C is measured. Therefore a set-up is used with a lay-out schematically presented in Figure 4.1. It consists of one glass furnace, one reference furnace containing a black body, an FT-IR spectrometer and flat and parabolic golden mirrors. In the glass furnace a glass sample is heated and the emitted radiation is directed via a mirror system to the FT-IR spectrometer. To calibrate the measured signal a black body is also heated, separately, in a reference furnace. Radiation emitted by the black body is also directed via golden mirrors to the FT-IR spectrometer. A flipping golden mirror is used to measure either the radiation emitted by the glass sample or the radiation emitted by the black body. In the next subsections, some of the individual parts of the set-up are discussed separately in more detail.

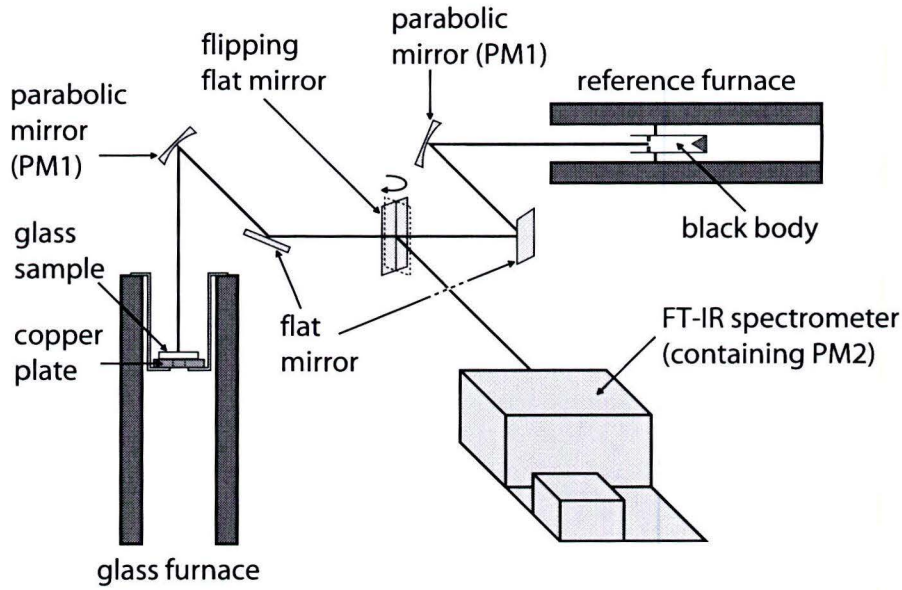

Figure 4.1: Overview of the experimental setup

4.2.1 Heating of the glass samples

The glass samples are heated in the glass furnace, a tube furnace. Inside, the samples are suspended by a sample holder as shown in Figure 4.2. Two sample holders are made to position the glass sample in the furnace at a depth of either $20cm$ or $40cm$. On top of the sample holder, a copper plate is placed on which the glass sample can be positioned. The plate is made from copper to ensure high thermal conductivity. It has an inner and outer diameter of respectively $5cm$ and $12cm$. The inner diameter ensures that no copper is positioned in the optical path of the measurement beam. In the copper plate two holes are present for thermocouples. In one hole, a thermocouple is positioned $1mm$ underneath the copper surface, measured from the top. In the other hole, the thermocouple is positioned against the surface of the glass sample.

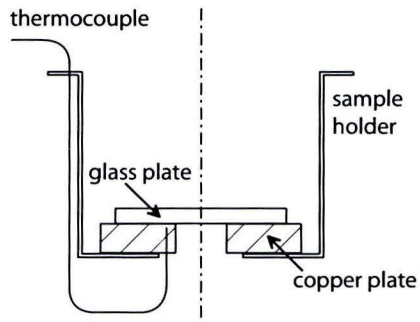

Figure 4.2: Sample holder

The work-tube inside the glass furnace is vertical. As the medium inside is heated, this will lead to a so called 'chimney effect' as a result of natural convection. This is undesirable, since it brings temperature gradients inside the oven and a large amount of heat loss. Therefore the bottom and the top of the furnace are closed with ceramic wool. Because the wool is positioned directly in the optical path of the measurement beam, it has to be removed both at the top and bottom before any measurement. After measurement, it is replaced as quickly as possible. To further minimize heat loss, a radiation shield is placed in the top part of the furnace.

4.2.2 Reference furnace

The reference furnace is a horizontal tube furnace. Inside, a heating element is connected with three variable voltage sources. This set-up creates three control zones to minimize temperature gradients. At the entrance of the furnace, radiation shields are placed to minimize heat loss. The reference furnace contains a black body that is used to calibrate the FT-IR spectrometer. The calibration method is discussed in section 4.2.3. At three positions, a thermocouple (K-type) is placed in the black body. In combination with the variable voltage sources for the three control zones of the reference oven, the temperature gradient over the black body, measured by the thermocouples, is minimized to approximately $1 - 2\,^{\circ}\mathrm{C} \pm 4\,^{\circ}\mathrm{C}$. For more information about the black body used, the reader is referred to Appendix D.1

Contrary to the glass furnace, the temperature in the reference furnace is controlled analogous by hand. This means that when heating the oven, care must be taken to minimize thermal stresses to prevent cracking of the furnace insulation material. At temperatures between $20 - 400\,^{\circ}\mathrm{C}$, this insulation is more brittle than at higher temperatures. Therefore, the advised maximum power of the variable voltage sources is about 40%. At temperatures above $600\,^{\circ}\mathrm{C}$, maximum settings of about 70% are sometimes used. In the emissivity experiments, the first measurement was at $600\,^{\circ}\mathrm{C}$. Therefore, at start up, the power source was set to 35% resulting in a heating time of approximately 4 hours. During heating, an extra heat shield is placed before the entrance of the reference furnace to minimize heat loss. Still, the temperature at the entrance side of the

black body tends to be cooler then at the backside. This temperature gradient is somewhat compensated by setting the manual controller 1% lower at the higher temperature side, and 1% higher at the lower temperature side. The accuracy of the black body temperature measured with the thermocouples is about 4 °C.

4.2.3 FT-IR spectrometer

To derive the emissivity of the glass samples, we have to determine the emitted spectral intensities. For this purpose, we use a Perkin Elmer GX FT-IR spectrometer. The working principle is based on the same principle as the Michelson interferometer, discussed in Appendix D.2.

The measured spectral energy has to be translated to spectral intensity. Since the detector sensitivity, optical path and ambient conditions all influence the measured spectral energy, we need a calibration signal. For this we use the measured spectral energy of a black body, where the measurement beam has the same optical path length and ordinate size as the measurement beam at the glass sample side. The spectral intensity emitted by the glass $i_{\lambda g}$ is determined as follows:

$$i_{\lambda g}(T_g) = s_{\lambda g}(T_g)\ \frac{i_{\lambda b}(T_b)}{s_{\lambda b}(T_b)} \tag{4.2}$$

with $s_{\lambda g}$ the measured signal from the glass sample, $s_{\lambda b}$ the measured signal from the black body, T_g and T_b the temperature of the glass sample, respectively the black body. The intensity $i_{\lambda b}$ of the black body at temperature T_b is calculated using equation (2.6). The term $\frac{i_{\lambda b}(T_b)}{s_{\lambda b}(T_b)}$ is further referred to as the spectral transformation factor.

For more information about the Perkin Elmer GX FT-IR spectrometer, the reader is referred to [11].

4.2.4 Optics

The optics of our experiments are a combination of the optical components inside the FT-IR spectrometer and the components positioned between the FT-IR and the measured glass sample, respectively black body. This distinction is made since the positions of the components inside the FT-IR spectrometer are fixed, and we can only vary the positions of the external components to optical align and direct our measurement beam. This beam is the part of the radiation emitted from a sample or black body that is guided by the optical components through the FT-IR spectrometer towards the detector. For this purpose, we use a combination of plane and curved golden mirrors. The plane mirrors are employed to bend the beam path, while the curved mirrors are used to focus an otherwise diverging beam onto a sample or black body. Golden mirrors are used because of their high reflectivity, up to 99.5% over the entire spectrum of interest, [12]. For focussing, it is also possible to use lenses. However, the most important drawback of lenses is that they tend to have relatively large reflection losses and their spectral range regarding high transmissivity is limited.

For a detailed discussion of the optical components and the optical alignment calculations needed for the positioning of our measurement beam, the reader is referred to Appendix D.3. Note that this optical alignment method follows Nagtegaal, [10], in which the alignment method is based on the position of the b-stop image. The b-stop is an aperture situated inside the FT-IR spectrometer. Since in practice the evaluation of the b-stop image position is difficult and can only be determined accurately to about $\pm 10cm$, a new additional method for the evaluation of the b-stop image position is derived, discussed in section 4.4.1.

4.3 Total hemispherical emissivity derivation method

In the derivation of the total hemispherical emissivity we start with the determined intensity from a glass sample $i_{\lambda g}$. The derivations follow the notation as used in section 2.2.4. Since this

intensity is depending on wavelength λ, direction (θ, φ) and the temperature T the directional spectral emissivity can be calculated using: $\varepsilon(\lambda, \theta, \varphi, T) = \frac{i_\lambda(\lambda,\theta,\varphi,T)}{i_{\lambda b}(\lambda,T)}$, equation (2.27).

The measurement domain of the FT-IR is not infinite. Therefore it is not possible to calculate the directional total emissivity, $\varepsilon_t = \varepsilon_t(\theta, \varphi, T)$, directly with equation (2.30). For wavelengths higher then the maximum measurable wavelength, further denoted as λ_1 an estimation for the directional spectral emissivity is used. At these wavelengths glass radiates almost as a black body with spectral directional emissivity, $\varepsilon_{b,r} = \varepsilon_{b,r}(\lambda, \theta, \varphi, T)$. It only has to be compensated for the reflection. Therefore the subscripts "$_{b,r}$" denote the black body behavior off the glass compensated for the reflectivity in the normal direction. Combined with equations (2.29), (2.30) and (2.31) we can express the directional total emissivity as:

$$\begin{aligned} \varepsilon_t &= \varepsilon_t(\theta, \varphi, T) \\ &= \frac{\int_0^\infty \varepsilon_\lambda \; i_{\lambda b} d\lambda}{\int_0^\infty i_{\lambda b} d\lambda} = \frac{\int_0^{\lambda_1} \varepsilon_\lambda \; i_{\lambda b} d\lambda + \int_{\lambda_1}^\infty \varepsilon_{b,r} \; i_{\lambda b} d\lambda}{\int_0^\infty i_{\lambda b} d\lambda} \\ &= \frac{\int_0^\infty \varepsilon_{b,r} i_{\lambda b} d\lambda - \int_0^{\lambda_1} \varepsilon_{b,r} i_{\lambda b} d\lambda + \int_0^{\lambda_1} \varepsilon_\lambda i_{\lambda b} d\lambda}{\int_0^\infty i_{\lambda b} d\lambda} \\ &= \varepsilon_{b,r} + \frac{\pi}{\sigma T^4} \left[\int_0^{\lambda_1} \varepsilon_\lambda i_{\lambda b} d\lambda \; - \varepsilon_{b,r} \int_0^{\lambda_1} i_{\lambda b} d\lambda \right] \end{aligned} \tag{4.3}$$

With $\varepsilon_\lambda = \varepsilon_\lambda(\lambda, \theta, \varphi, T)$, the directional spectral emissivity. In the measured direction the reflection is about 10%, therefore $\varepsilon_{b,r} \approx 0.9$.

In the determination of the total hemispherical emissivity we use the directional total emissivity in the normal direction of the glass surface. Therefore we have to compensate for the directional variation of the emissivity. This variation is the result of the increase of the glass surface reflectance at steeper incident angles. The characteristic behavior of the directional variation of the surface emittance is derived from [12]. This information is fitted in Figure 4.3. Here the information about the decline of the emissivity is translated into a cut out in the cross-section of a unit hemisphere.

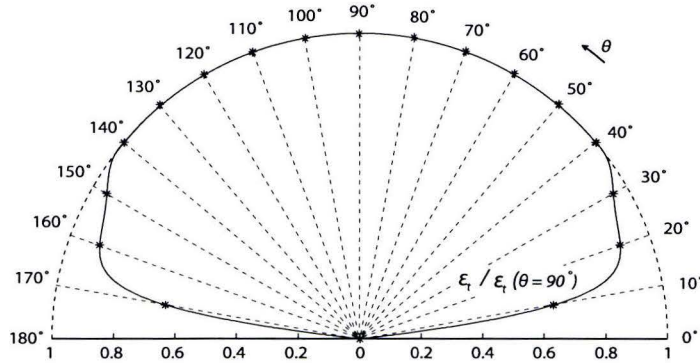

Figure 4.3: The directional variation of the surface emissivity projected on a unit hemisphere

The compensation for the directional variation of the emissivity can be found by calculating the ratio of the remaining volume with respect to the unit hemisphere. This ratio is approximately 0.72. The total hemispherical emissivity, ε_{th} at the glass surface of the gob is thus:

$$\varepsilon_{th} = \varepsilon_{th}(T) = 0.72\varepsilon_t \tag{4.4}$$

4.4 Experimental analysis

4.4.1 Optical alignment

The optical alignment method from [10], as discussed in appendix D.3, is based on the position of the b-stop image. This position is the defined position for the measurement spot in the emissivity experiments. To calculate this position the distance between the parabolic mirrors PM1 and PM2 has to be known. This distance is estimated since the position of PM2 inside the FT-IR is unknown. Consequently, the position of the b-stop image is an estimate as well and preferably has to be evaluated. However the evaluation of the position of the b-stop image, proved to be a difficult problem. In practice it was based on a rough estimate of the size and intensity of the measurement spot. Therefore a new evaluation method is derived based on the lens formula and an object image as discussed below.

Method for the evaluation of the b-stop image position

An object, for example a slide illuminated with a slide projector, is placed in the set-up as sketched in Figure 4.4.

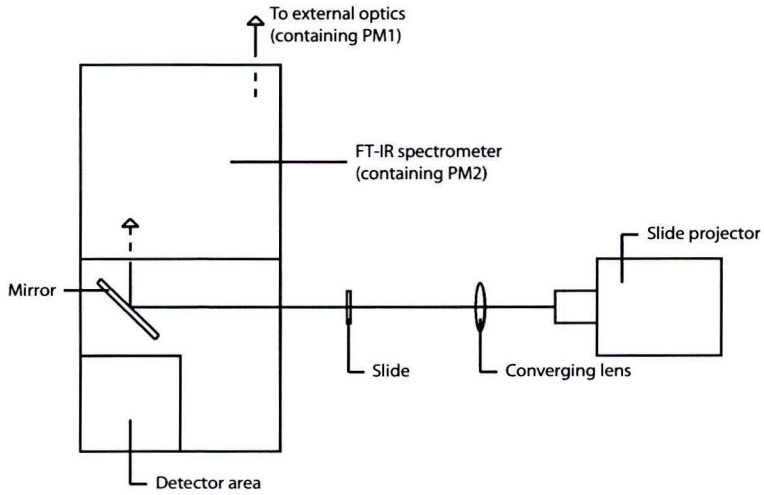

Figure 4.4: Set-up for the evaluation of the b-stop image position

The advantage of the use of a slide is that the image position can be found relatively accurate, contrary to the b-stop image. The contrast of the slide image will vary from fuzzy to clear back to fuzzy, when we view the projected image of the slide along the optical path. In the image of the b-stop the same effect is present but not visible.

By making use of the lens formula, we can calculate the position of the slide image with respect to parabolic mirror PM1, as function of the distance between PM1 and PM2, for different positions of the slide with respect to parabolic mirror PM2. However we can only measure the position of the slide with respect to the window of the FT-IR. The result is shown in Figure 4.5. It can be seen that by increasing the distance between the slide and PM2, the slide image position converges. Therefore, if we choose the distance of the slide with respect to the FT-IR window large enough ($> 70cm$) we can neglect the unknown distance of the window to PM2 and the distance between PM2 and PM1 can be accurately determined. This results in a position determination of the b-stop image, accurately at about $\pm 1cm$, based on a measurable slide image position. This is sufficient enough for an accurate optical alignment.

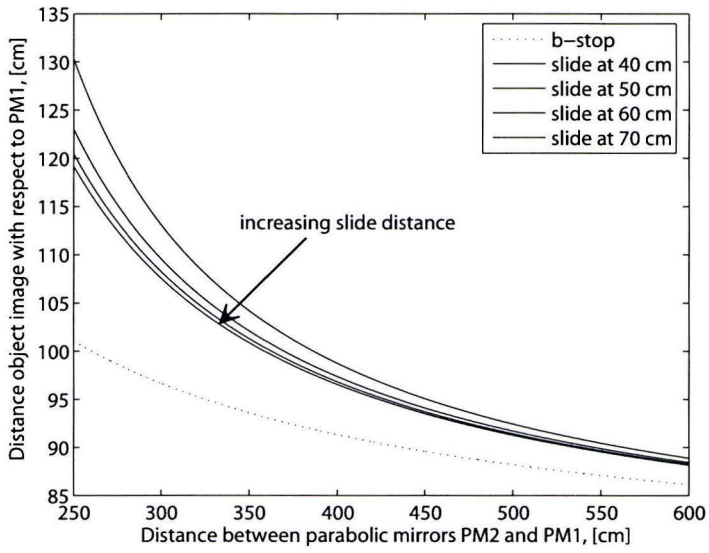

Figure 4.5: Distance slide and b-stop image with respect to PM1

Measurement spot size

An inaccuracy in the determination of the b-stop image position can lead to a difference in measurement spot size between the glass sample and the black body. Furthermore, the measurement beam will always be slightly converting or diverting. Consequently, differences in optical path length will effect the size of the measurement spot as well. A larger measurement spot will lead to a higher spectral energy measurement. This also has an effect when measuring relatively thick glass samples, since especially at small wavelengths the glass is optically thin. A glass sample is measured in the oven at $200mm$ and at $400mm$ depth. The effect of the variation of measurement spot size on the measured spectral energy is shown in Figure 4.6.

In the emissivity experiments, only relatively thin glass samples are used $3.0mm \leq s \leq 19mm$, with s the glass sample thickness. It will be clear from Figure 4.6, that the effect of the difference in measurement spot size on the measured spectral energy, in the glass sample along the optical path, is small.

4.4.2 Spectral transformation factor

The spectral transformation factor $\frac{i_{\lambda b}(T_b)}{s_{\lambda b}(T_b)}$, as discussed in section 4.2.3, is used to determine the spectral intensity emitted from a sample in the glass furnace. An independent relation with respect to the temperature is assumed. If not, the spectral transformation factor would have to undergo a complicated evaluation experiment, in which the dependency with respect to the emitted energy would have to be determined.

To evaluate the adopted assumption, the spectral transformation factor is composed from different blackbody measurements with varying temperatures. An example of the transformation factor is shown in appendix C. The spectral ratio of the difference between the composed spectral transformation factors at 600 °C and 1200 °C is given in Figure 4.7.

It can be seen that the spectral transformation factor is consistent and can be considered temperature independent for $1.5\mu m < \lambda < 4.1\mu m$ and $4.4\mu m < \lambda < 8.0\mu m$. At all other wavelengths, the spectral transformation factor is inconsistent as a result of poor signal to noise ratio. This is probably caused by a combination of low detector sensitivity at wavelengths $\lambda < 1.5\mu m$ and concentrations of gasses in the air. For example carbon dioxide has an absorption band at 2.7

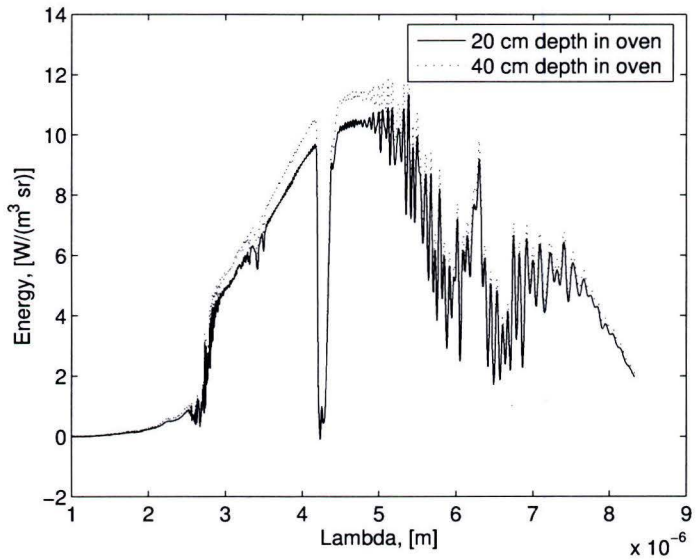

Figure 4.6: Measurement spectral energy glass sample, with a temperature of 700 °C and thickness s = 8 mm, with different measurement spot size

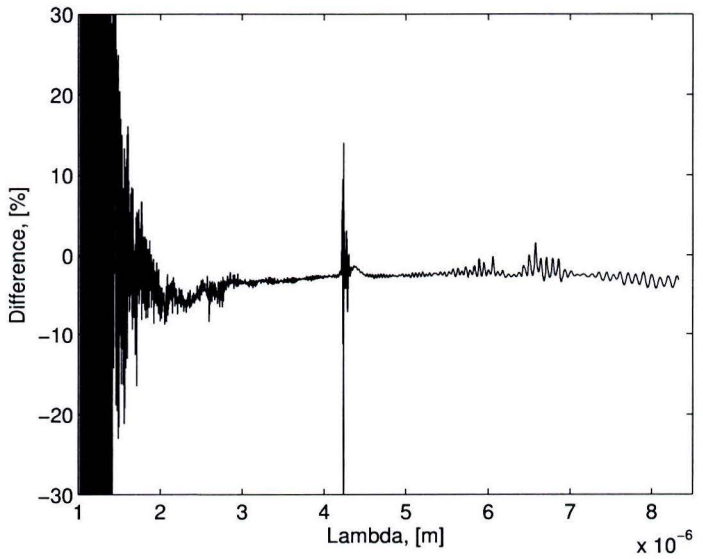

Figure 4.7: Variance spectral transformation factor for T = 600 - 1200 °C

and $4.3\mu m$. In Figure 4.7 a clear deviation in the spectral transformation factor can be seen at $\lambda = 4.3\mu m$.

4.4.3 Ground intensity correction

In the emissivity experiments, the spectral energy emitted from a glass sample at a distance d_{sample} with respect to $PM1$ is measured. Since glass is a transparent material, spectral energy emitted at a distance $d > d_{sample}$ also has to be evaluated. As the glass furnace is heating up, the bottom is closed with insulation material. The spectral energy emitted by this insulation is higher

than the energy emitted by a glass sample. Therefore, during measurements this insulation is removed. As a result the ground underneath the furnace is in the optical path of the measurement beam. Since the ground emits also, the contribution to the measured spectral energy must be evaluated. The spectral energy from the ground contributes as $i_\lambda(0)$ in the intensity definition of the glass, equation (2.15): $i_\lambda(S) = i_\lambda(0)\, e^{-\alpha_\lambda S} + \left(1 - e^{-\alpha_\lambda S}\right) i_{b\lambda}$. In this section, an estimate is derived for the contribution of the ground intensity in the glass intensity measurements, and the effect on the calculated emissivity is shown. In this analysis, the ground intensity was measured at oven temperatures of $T = 600, 700, 800\,°\mathrm{C}$. This is the same temperature domain as for the measurements on the glass samples. In the analysis, an estimate for the glass absorption coefficient is used as determined by TNO in [9].

To measure the spectral intensity of the ground, the glass oven was heated without the presence of a glass sample. During the experiment the top and the bottom of the vertical sample oven are closed to prevent natural convection. Following the procedure in section 4.2.1, the top and bottom of the oven are only opened when the spectral energy is measured. This has the additional benefit that the ground is only heated by the oven during measurements. Since a lower temperature results in a lower emitted energy distribution this is favorable to keep the contribution of the ground in the measurements as small as possible. The measured spectral energy of the ground as well as the measured spectral energy at the top of a glass sample at $T = 700\,°\mathrm{C}$ is shown in Figure 4.8. It can be seen that the ground intensity has a notable contribution at wavelengths $1.5 < \lambda < 2.7$ where the glass is optically thin.

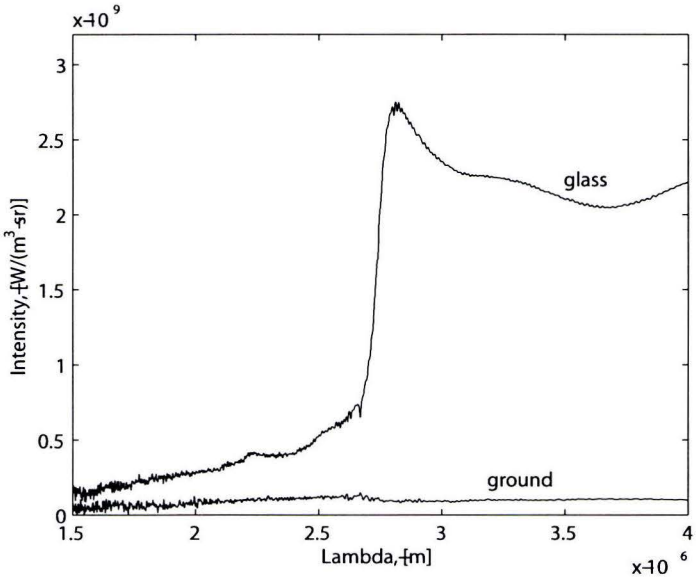

Figure 4.8: Measured intensity float glass, with thickness s = 3 mm, T = 700 °C, and intensity ground

In a glass experiment, the ground intensity enters a glass sample at the bottom. Measurement takes place at the top. As a result of absorption in the glass the ground intensity decreases with glass thickness. The emitted intensity of the glass itself is a function of temperature. Since glass is a transparent material, the measured intensity in the conducted experiments is a combination of the emitted intensity by the glass and the transmitted intensity of the ground. As the temperature of the glass increases, the emitted intensity by the glass increases as well. As a result the contribution of the transmitted intensity of the ground decreases. The portion of the ground intensity in the measurements of the glass intensity is shown for a sample at 700 °C in Figure 4.9.

From Figure 4.9 it becomes clear that the contribution of the ground intensity in the measured intensity is highest at the low absorption region $\lambda < 2.7\mu m$. This region also emits poorly, which

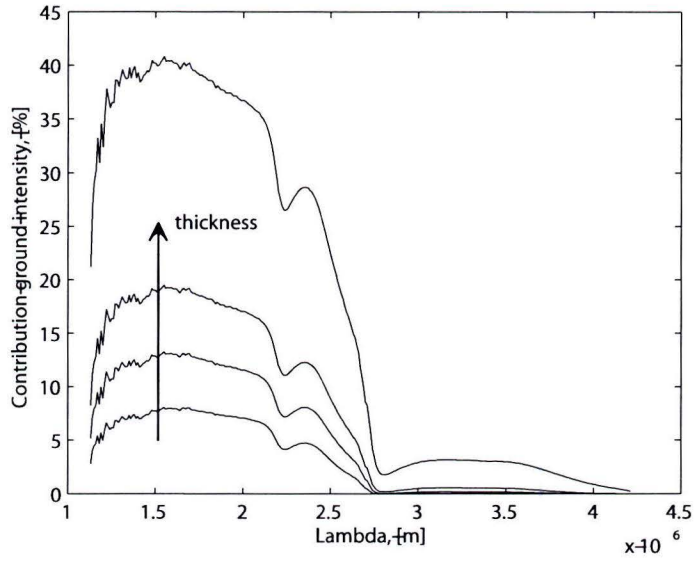

Figure 4.9: Contribution ground intensity in measured intensity for float glass with thickness s = 3, 8, 12, 19 mm at T = 700 °C

explains the relative high influence of the ground intensity. The thinner the glass sample, the lower the absorbed amount of ground intensity, resulting in a contribution of the ground intensity up to 40% at $\lambda \approx 1.5\mu m$ for the thinnest glass sample.

The intensities are measured to determine the spectral emissivity of the glass. In Figure 4.10 the spectral emissivity is shown for different glass thickness with and without correction for the ground intensity.

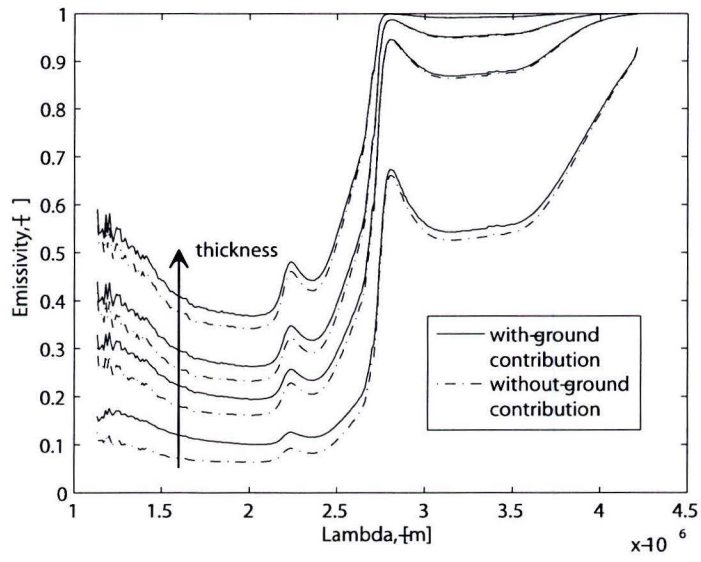

Figure 4.10: Contribution of ground intensity in determined spectral emissivity of float glass with thickness s = 3, 8, 12, 19 mm at T = 700 °C

The contribution of the ground intensity on the spectral intensity can clearly be seen for

$\lambda < 2.7\mu m$. At higher wavelengths $\lambda > 2.7\mu m$, the glass absorptance is high and the contribution of the ground intensity is only worth mentioning for the thinnest glass sample. Since our interest lies in the total hemispherical emissivity, our analysis has to go one step further. The difference in the calculated total hemispherical emissivity as a result of the ground intensity contribution during measurement is derived and amounts to a small 1.5%. Therefore the ground intensity can be neglected in the determination of the total hemispherical emissivity.

4.4.4 Reproducibility

In this section we discuss the reproducibility of the spectral energy measurements of glass for $1.5\mu m < \lambda < 4.1\mu m$ and $4.4\mu m < \lambda < 8.0\mu m$. For all other wavelengths the signal to noise ratio resulted in poor reproducibility as discussed in section 4.4.2

The reproducibility of the experiments is an important factor in the evaluation of the results. The results are affected by, in order of importance, deviations in the optical alignment, inaccuracies in the temperature measurements and changes in ambient conditions. Deviations in the optical alignment can easily be introduced during measurements as a result of the moving mirror incorporated in the set-up. Small changes in the orientation of this mirror can have a drastic effect on the results. To test the reproducibility the same glass sample measurement has been conducted two times on different days. The results for the emitted intensity at different temperatures are shown in Figure 4.11. The outcome of this test shows similar intensity results and demonstrate

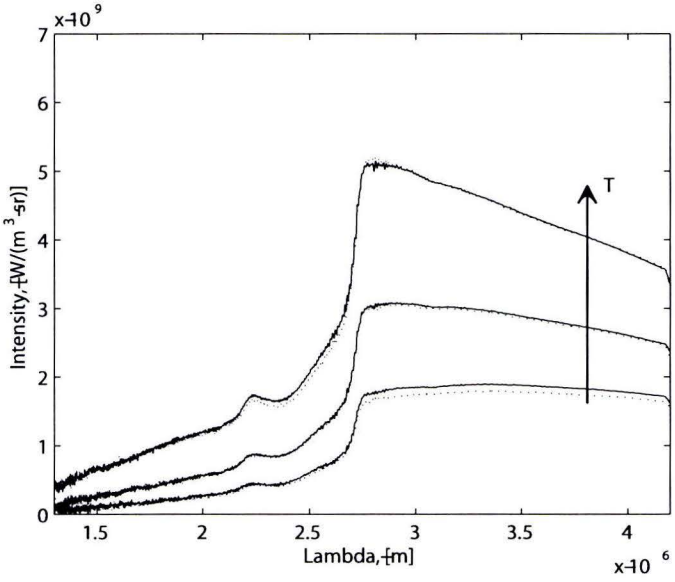

Figure 4.11: Reproducibility test: intensity glass sample with thickness 12 mm at T = 600,700,800 °C

the reproducibility of the experiments. However the intensity measured at 600 °C shows a more deviating result. A short analysis on the origin of this difference will now be conducted.

When we look at Figure 4.11 it can be seen that the calculated intensity from the first experiment at 600 °C is higher than from the second experiment. To understand this we first have to consider the equation for the intensity calculation, equation 4.2:

$$i_\lambda(T_g) = s_{\lambda g}(T_g)\,\frac{i_{\lambda b}(T_b)}{s_{\lambda b}(T_b)} \tag{4.5}$$

with $s_{\lambda g}$ and $s_{\lambda b}$ the measured spectral energy from respectively the glass sample and the blackbody and $i_{\lambda b}(T_b)$ the theoretical intensity of a blackbody with temperature T_b. T_g is the measured

temperature of the glass sample. T_b and T_g are measured in respectively the blackbody and the glass sample oven. Note that the spectral transformation factor $i_\lambda(T_b)/S_{\lambda b}(T_b)$ is independent of temperature but dependent on inaccuracies in measurements of T_b.

A close examination of the spectral transformation factor reveals a deviating result for the first experiment at 600 °C. It was higher at all wavelengths compared to the other spectral transformation factors. A sensitivity analysis of T_b on $i_\lambda(T_g)$ is performed to rule out that this deviation is the result of an error in the measurement of T_b. It showed that a measurement error in T_b of about 15 °C is needed to cause a shift in the intensity as calculated for the second experiment at 600 °C. However the defined accuracy in the measurement of T_b is approximately 4 °C. Furthermore, if a measurement error of 15 °C is taken into account, this would result in an spectral transformation factor which would be substantially lower than from the other experiments. Therefore we focus on inaccuracies in the measurement of the remaining term in the spectral transformation factor, $S_{\lambda b}$.

If during measurement the optical path is not aligned properly this could result in measurement area partly at the outer side of the black body, as shown in Figure 4.12. Then the measured $s_{\lambda b}(T_b)$ would be lower and hence result in a higher spectral transformation factor and consequently a higher calculated intensity. Therefore from this analysis we have to conclude that the difference in measured intensity at 600 °C is the result of a divergence in the optical path to the black body. This is probably caused by a misalignment of the flipping mirror and would result in a deviation in the total hemispherical emissivity less then 3%. Although this deviation is small, care must be taken to minimize deviations in the orientation of the flipping mirror during measurements. If they are excluded we can state that the experiments have a high reproducibility.

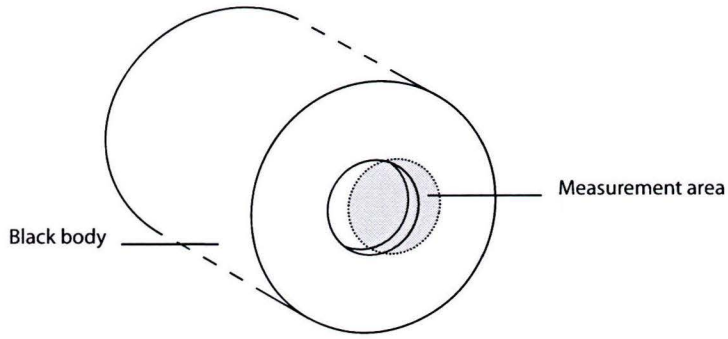

Figure 4.12: Consequence of misalignment on measurement position at black body entrance

4.5 Emissivity float glass

In this section the total hemispherical emissivity of the float glass samples, with a thickness of 3.0, 8.0, 12.0 and 19 mm at 600, 700 and 800 °C, is derived from the results of the experiments. The method is followed as discussed in section 4.3. These calculated emissivities are compared to the derived emissivities from data describing the spectral absorption coefficient of float glass, [9]. Also, this data is used to calculate the total hemispherical emissivity from glass samples from 600 °C up to 1200 °C with a thickness up to 400mm. This is especially interesting since the glass gob has a temperature of about 1000 °C, a diameter of about $50 - 150mm$ and a length up to 400mm.

4.5.1 Spectral directional emissivity

We start with the calculation of the spectral directional emissivity in the normal direction of a glass sample for the $0 \leq \lambda \leq 8\mu m$ domain. As a result of the sensitivity of the apparatus we can

not use measurement data in the entire wavelength domain. Therefore the domain is divided in five parts:

$$\begin{aligned} 0 \leq \lambda \leq 0.2\mu m, \quad & \varepsilon_1 = 0.90 \\ 0.2\mu m < \lambda < 1.5\mu m, \quad & \varepsilon_2 = \varepsilon_{3,\lambda=1.5\mu m} \\ 1.5\mu m \leq \lambda \leq 4.1\mu m, \quad & \varepsilon_3 = \varepsilon_{m,\lambda} \\ 4.1\mu m < \lambda < 4.4\mu m, \quad & \varepsilon_4 = \varepsilon_{3,\lambda=4.1\mu m} \\ 4.4\mu m \leq \lambda \leq 8.0\mu m, \quad & \varepsilon_5 = \varepsilon_{m,\lambda} \end{aligned}$$

with $\varepsilon_{m,\lambda}$ the calculated emissivity from measurement data. An example is shown in Figure 4.13. The values of ε_1, ε_2, ε_4 are based on spectral radiation measurements on glass as discussed in [13], [12], and taking into account a reflectivity in the normal direction of about 10%. From Figure 4.13

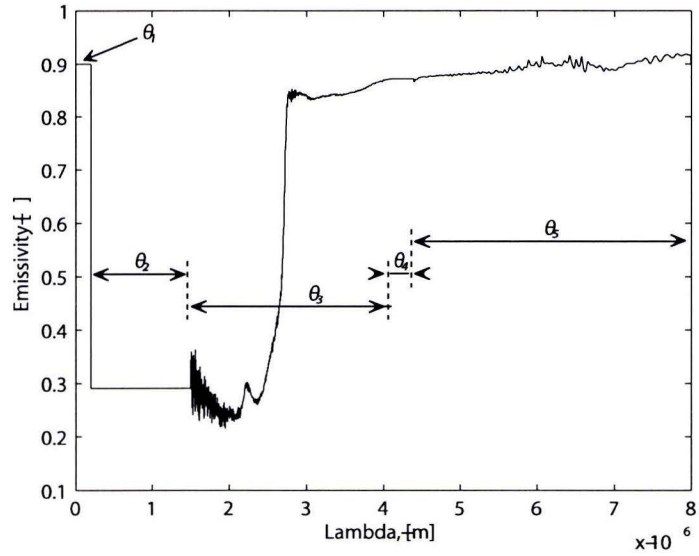

Figure 4.13: Spectral emissivity of a float glass sample with thickness 12 mm at T = 700 °C

it might seem that the imposed approximations for the spectral emissivity, (ε_1, ε_2 and ε_4), can have great impact on further calculations and could be at least arguable. However, a translation back to intensities, Figure 4.14, shows the favorable results of the approximation. It will be clear that small errors in the approximation will have a negligible effect in further derivation of the total hemispherical emissivity.

4.5.2 Total hemispherical emissivity

With the derived spectral emissivity we can now calculate the total hemispherical emissivity from the glass samples as discussed in section 4.3. The total hemispherical emissivity from the glass samples is shown in Figure 4.15 as dotted lines. Note that an approximation for the directional reflectancy is taken into account, following [13] and [12], since only measurements perpendicular to the glass samples have been performed. The total hemispherical emissivity, calculated from information of the absorptance of float glass from [9], is derived in the same way. The only difference is that first the spectral intensity has to be calculated using the intensity definition of the glass, equation (2.15), without ground contribution: $i_\lambda(S) = \left(1 - e^{-\alpha_\lambda S}\right) i_{b\lambda}$. The calculated total hemispherical emissivity from [9], is shown in Figure 4.15 as solid lines.

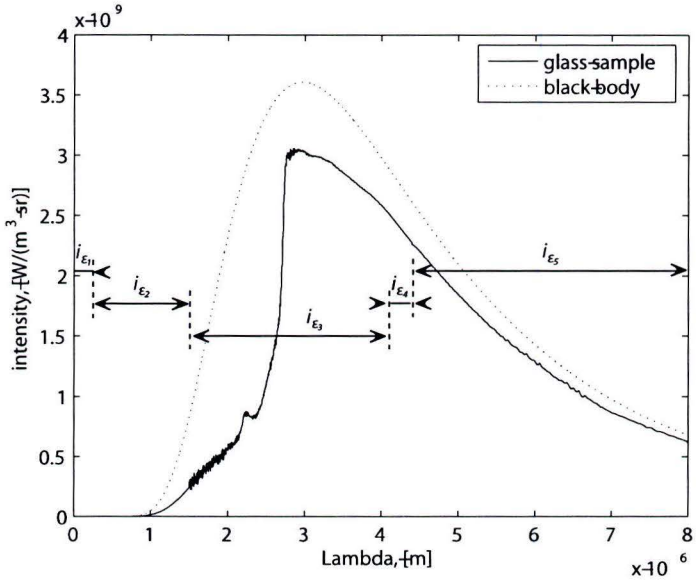

Figure 4.14: Recalculated intensity glass of a float glass sample with thickness 12 mm at T = 700 °C

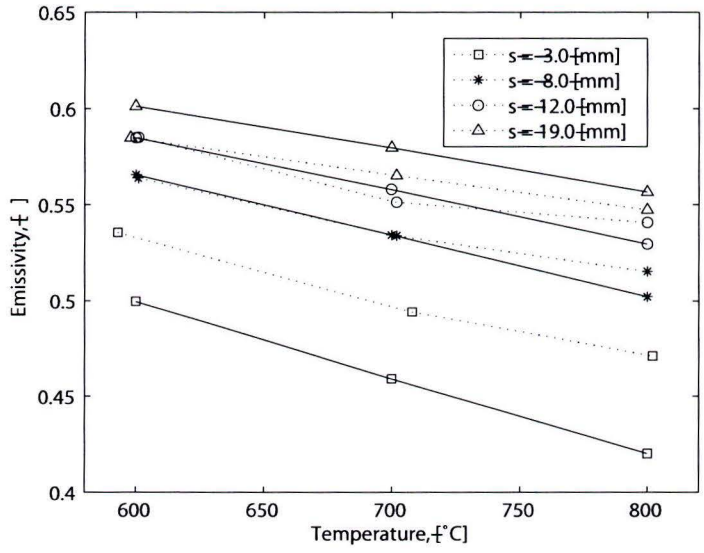

Figure 4.15: Total hemispherical emissivity of float glass, with thickness s = 3,8,12,18 [mm]

It can be seen that the emissivity decreases by increasing temperature. As a result of the increase in temperature the maximum intensity peak of a black body is shifted towards the smaller wavelengths, as described by Wien's displacement law, equation 2.8. At these wavelengths the glass emits poorly resulting in a drop in emissivity.

Also, it can be seen that the emissivity calculated from the experiments and from the absorptance data are similar. Small deviations occur, possible as a result of measurement errors. The deviation is the highest for the thinnest glass sample. At 800 °C all determined emissivities from the experiments seem too high, deviating from the expected value compared to the emissivity calculated from the absorptance data. This is thought to be the result of a contribution of the

oven wall emission in the measurement of the glass sample emission, explained as follows. At 800 °C the glass sample starts to melt and deforms under gravity. This results in a bowl shaped glass sample in which in combination with the reflectance of the glass, possibly wall emissivity is reflected in the direction of the measurement beam, as shown in Figure 4.16. This results in a higher measured spectral energy and finally in a higher calculated emissivity.

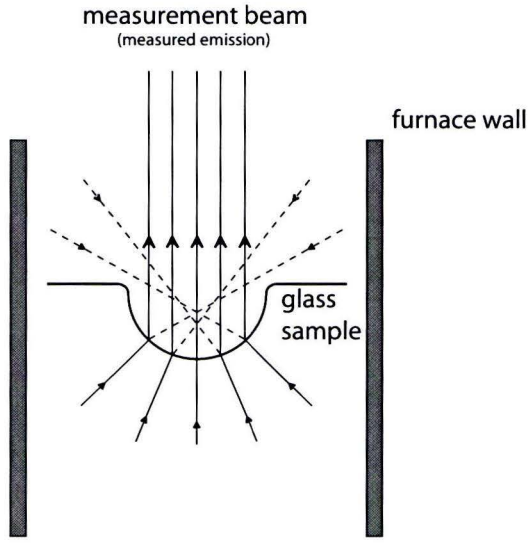

Figure 4.16: Deformation of the glass sample at $T = 800\,°C$

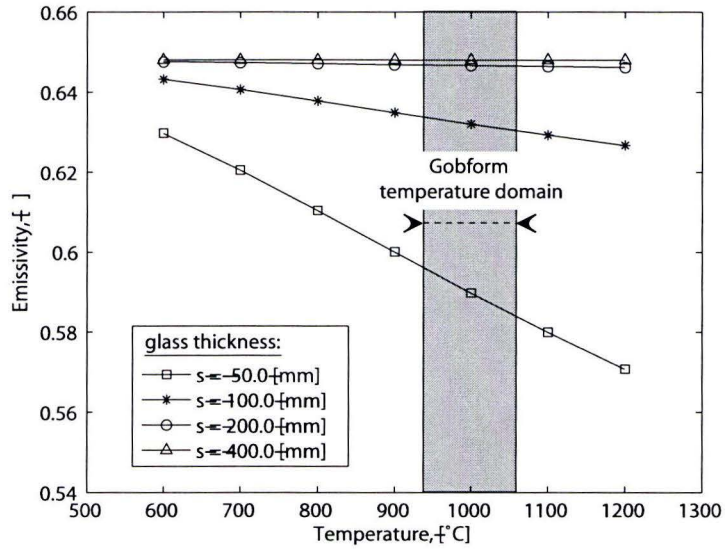

Figure 4.17: Total hemispherical emissivity of float glass, with thickness s = 50, 100, 150, 400 [mm]

Now, let's take a look at the emissivity calculated for a glass thickness comparable to a gob in a gobform process, as shown in Figure 4.17. It can be seen that the total hemispherical emissivity decreases with increasing temperature. However this temperature dependency decreases with

increasing glass thickness. Also, the thicker the glass sample, the higher the emissivity. The theoretical maximum value of the emissivity is 1[−]. This is when the glass has a thickness such that it emits as a blackbody. However reflectancy has to be taken into account resulting in a drop of emissivity. In this case, an approximated reflectance in the normal direction of about 10% corrected for the hemispherical reflectance dependency, about 0.72% as discussed in 4.3, resulted in a maximum value for the total hemispherical emissivity of about $0.90 \times 0.72 = 0.648[-]$. It will be clear from Figure 4.15 that the emissivity of a sample thickness $> 200mm$ of the type op float glass discussed here varies little and follows this maximum value closely. This is a favorable result since radiation crossing a point at the gob surface is a summation from radiation inside the gob out of different directions with different optical path lengths. When we look even more closely in the temperature area comparable with gob temperatures during the gobform process, 950 °C – 1000 °C, the variation in total hemispherical emissivity for a glass sample with a thickness of $50 - 400mm$ is less then $\approx 1\%$.

In the derivation of the total hemispherical emissivity the assumption is made that the variance of the emissivity as a result of the temperature dependent property of the absorption coefficient is negligible. To verify this assumption the difference in the emissivity is derived based on calculations with an absorption coefficient measured at $T = 20\,°C$ and at $T = 1000\,°C$. This difference is shown in Figure 4.18 for a glass sample with thickness $50 - 400mm$, comparable to a gob during the gobform process. It can be seen that the temperature dependence of the absorption coefficient has only a small influence on the emissivity. In the temperature domain of the gobform process, 1000 °C, this influence is less then 2%.

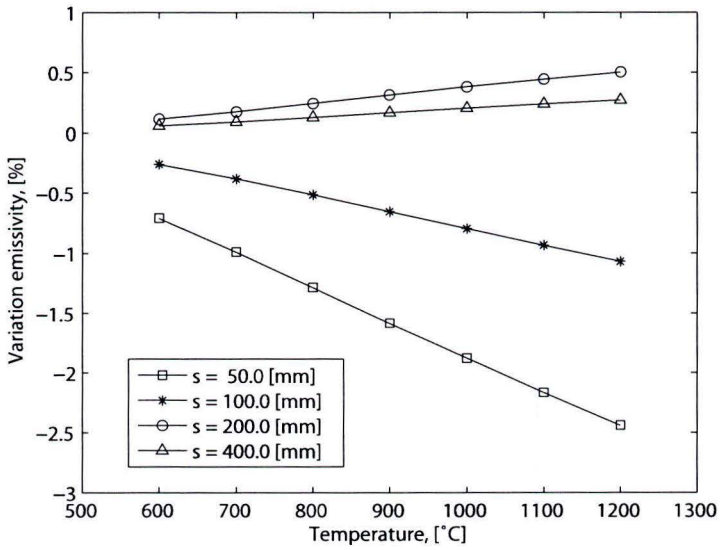

Figure 4.18: Variation of the total hemispherical emissivity as a result of the variation of the absorption coefficient at T = 20 °C and at T = 1000 °C

In this chapter the determination method for the total hemispherical emissivity of float glass is discussed. This method can be used for different types of glass. With the emissivity determined we are able to implement the magnitude of the heat flux of the gob to the surroundings in the gobform model using equation 4.1.

Chapter 5

Validation and results

The gobform model predicts shape and temperature characteristics of a gob during the gobform process. To validate the model, we would like to compare numerical results with experimental data. Special interest lies in an accurate description of the temperature profile throughout the gob. However the optical characteristics of glass melts in combination with the radiative heat transfer properties complicate accurate non-intrusive measurement methods. Effort has been made [10] to develop an optical method for temperature profile measurements in glass melts. As a result of the complexity and inaccessibility of a gobform installation the adaptation of this method to suit the conditions required is abandoned. Alternatively, validation on different parts of the gobform model have been performed. In the validation method a distinction is made between numerical validation and experimental validation.

The outline of this chapter is as follows. First different numerical tests on material convection, temperature convection and the radiative boundary condition are described to validate the numerical behavior of parts of the gobform model. Each group isolates a particular numerical implementation of a physical phenomenon in the gobform process. By testing the groups individually the cause and effect relations in the results are singled out as far as possible and these can subsequentely, be interpreted more easily. Finally an experiment to validate the computed gob shape of the gobform model is discussed.

5.1 Numerical validation

5.1.1 Material convection

In the gobform model the gob is simulated with a moving free surface in a fixed predefined mathematical domain. This means that the gob only partly occupies the computational domain. The other part of the domain is occupied by a fictitious fluid to account for the air surrounding a gob, as discussed in section 3.5. To distinguish between the glass and the fictitious fluid a material parameter is used ($0 \leq c < 0.5$ fictitious fluid, $0.5 \leq c \leq 1$ glass with $c = 0.5$ as the glass surface). The glass displacement in time is therefore described by the convection of this material parameter. In this section, the material convection algorithm is validated. The influence of the number and orientation of elements on the accuracy of the solution are tested.

1D: Uniform glass inflow

Consider a domain as shown in Figure 5.1 (a). At $t = t_0$, glass flows through the inflow boundary at the top with a uniform velocity of $0.05m/s$. At the sides the velocity in the normal direction and the tangential stress component are prescribed as respectively $u_n = 0$ and $\sigma_{nt} = \frac{1}{Re}(\frac{\partial u_n}{\partial t} + \frac{\partial u_t}{\partial n}) = 0$. At the bottom of the domain stress free outflow is prescribed, $\sigma_{nt} = 0$ and $\sigma_{nn} = -p + \frac{2}{Re}\frac{\partial u_n}{\partial n} = 0$. The domain is divided in part S_1 and S_2. Initially S_1 is filled with glass and S_2 is filled with the fictitious fluid. The amount of elements in S_1 is constant while in S_2 these are varied for the

different tests. The initial condition for the material parameter at the top curve and bottom curve of S_1 are respectively $c = 1$ and $c = 0.5$. Hence the initial position of the flowfront is guaranteed. The time step size is $0.1s$. Two different orientations of the elements in S_2 are used as shown in Figure 5.1 (b) and (c).

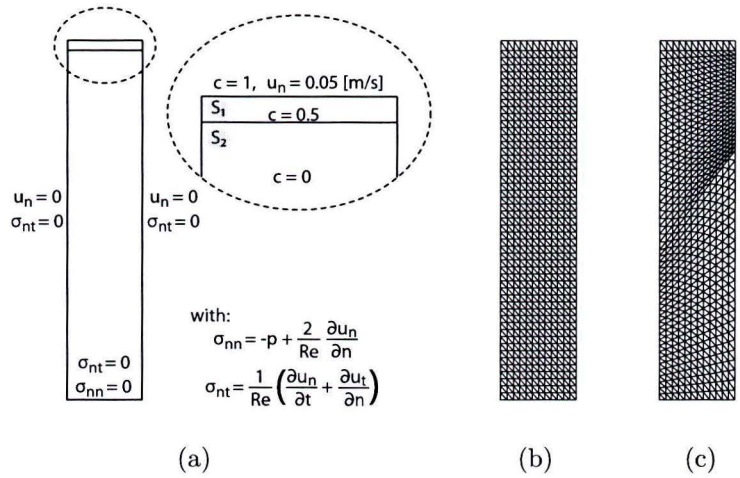

Figure 5.1: 1D uniform glass inflow: (a) initial and boundary conditions, (b) mesh uniform elements distribution and (b) mesh non-uniform elements distribution

We will discuss the displacement of the glass surface calculated with the straight mesh shown in Figure 5.1 (b). The calculations with the mesh in Figure 5.1 (c) give similar results. Since the difference is minimal they are shown in appendix E. The glass surface position is studied at the vertical centerline. In Figure 5.2 the displacement in time is shown for 30, 120, 600 and 900 elements as well as the analytical solution.

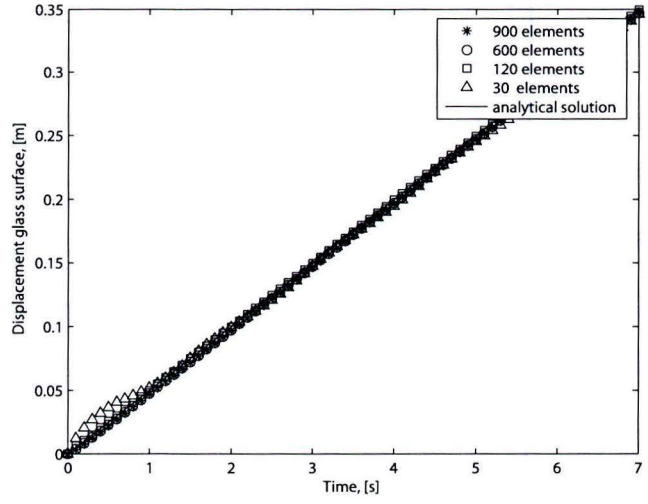

Figure 5.2: Glass surface displacement

It can be seen that the simulations follow the analytical solution accurately. Only at start-up some deviation occurs. Deviations are highest for the mesh generated with 30 elements. The influence of the amount of elements on the solution can be further examined. For this we look at

the calculated displacement of the glass surface per time-step compared to the analytical solution, shown in Figure 5.3. Here, the error can be seen as a function of time.

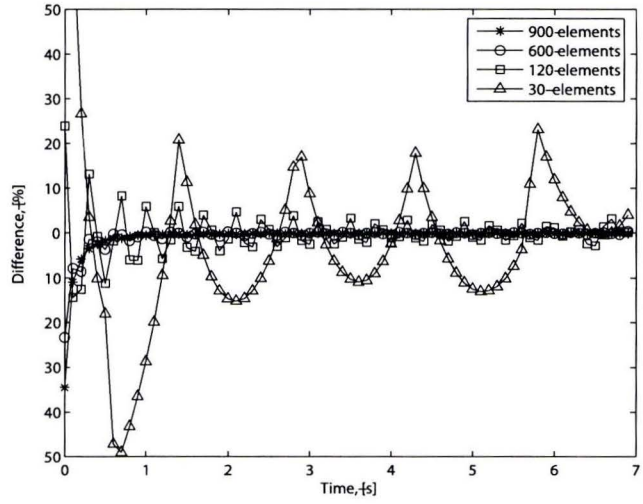

Figure 5.3: Glass surface displacement per time step in proportion to the analytical solution

It will be clear that the amount of elements used in the mesh generation influences the solution of the displacement of the flowfront. The error is the highest at start-up, 150% using 30 elements, 25% using 120 elements, 25% using 600 elements and 35% using 900 elements. After start-up, these errors decrease and oscillations around the analytical solution occur. The amplitude and the period of these oscillations decrease with an increasing number of elements.

2D: Settling glass surface under gravity

In this simulation an unbalanced glass surface within a container is subjected to gravity. The objective of this simulation is to examine the glass surface behavior in a 2D test problem. The initial condition of the glass surface and the boundary conditions are shown in Figure 5.4. On the sides and the bottom of the container $u_n = 0$ and $\sigma_{nt} = 0$ are prescribed. On the top the flow is stress free.

At $t = t_0$ the glass is subjected to gravity and will move in search of equilibrium. The equilibrium position is situated at a height of $-0.05m$. The settling of the glass surface position at the left side (side A) and at the right side (side B) of the glass container are shown in Figure 5.5. The shape of the glass surface is shown at $t = t_0$, $t = 5s$ and $t = 100s$ in Figure 5.6.

At start-up the height difference of the glass surface results in a pressure difference acting in the glass. This pressure difference causes the glass to flow. As the surface settles in search of equilibrium, the height difference of the surface decreases. Consequently, the pressure difference decreases as well. When we take a look at Figure 5.5 it can be seen that at side A and side B this decrease of flow velocity results in positions just underneath respectively above the equilibrium position at $t = 100s$.

Influence of velocity gradient in air on static glass surface position

The movement of glass in the fictitious fluid is modelled with the use of a discrete material parameter which is convected through the domain. In the gobform model, local velocity profiles can influence the defined material parameter gradient. These could theoretically distort the gradient of the material parameter to such an extend that the position of the glass surface is affected, deteriorating accuracy. In this testcase this effect is examined. Consider a container in equilibrium

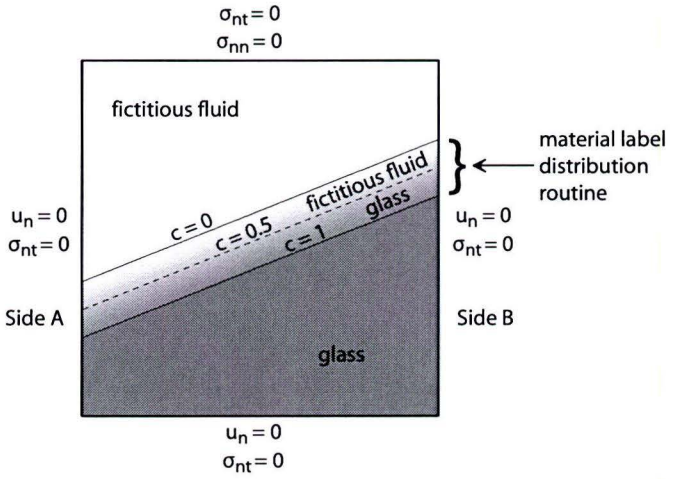

Figure 5.4: Initial and boundary conditions: Settling glass surface under gravity

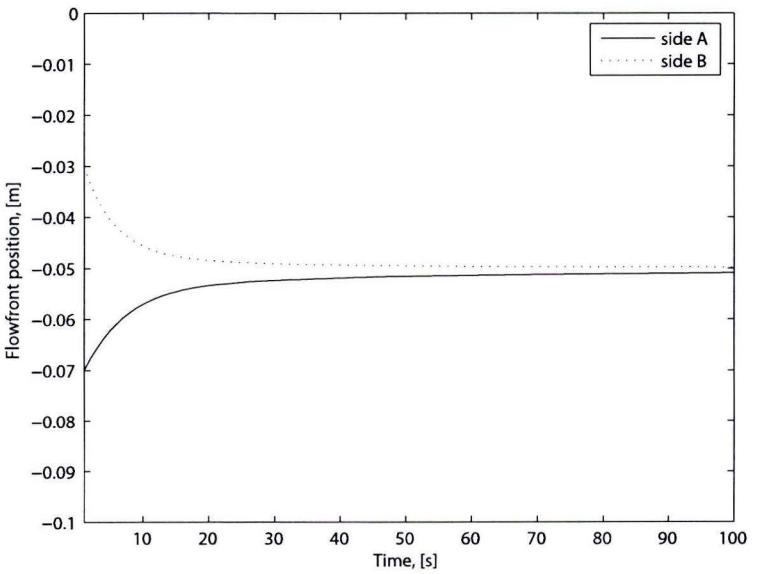

Figure 5.5: Glass surface at container side: left side (side A) or right side (side B)

partly filled with glass as shown in Figure 5.7. The glass is contained by the wall's, $u_n = 0$. At $t = t_0$ fictitious fluid flows from the left to the right just above the glass surface.

The velocity profile in the fictitious fluid convects the material parameter, shown in Figure 5.8 (a), (b) and (c). This convection distorts the initial gradient of the material parameter. Ultimately this leads to an inaccurate description of the glass surface position as shown in Figure 5.9.

The effect discussed above can also occur in simulations of the gobform process. Consider an axisymmetric domain as shown in Figure 5.10. Both the glass and the fictitious fluid are subjected to gravity. As a result outflow occurs at the bottom of the domain. Since both media are simulated incompressible this outflow is compensated by the inflow of fictitious fluid at the right hand side of the domain. This inflow influences the gradient of the material label parameter. The closer this inflow is situated to the gob the more it compresses the material label gradient. This can lead to

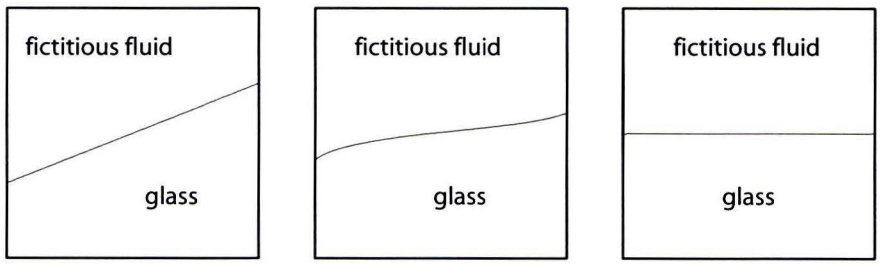

Figure 5.6: Glass surface position (a) at $t = t_0$, (b) at $t = 5[s]$ and (c) at $t = 100[s]$

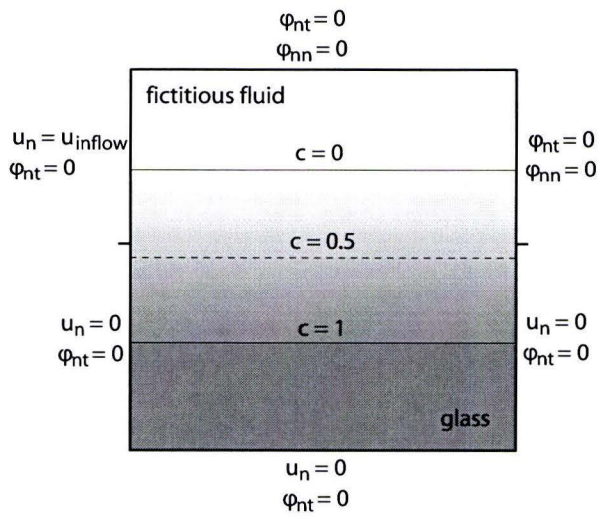

Figure 5.7: Initial and boundary conditions: Influence of velocity gradient in air on static glass surface position

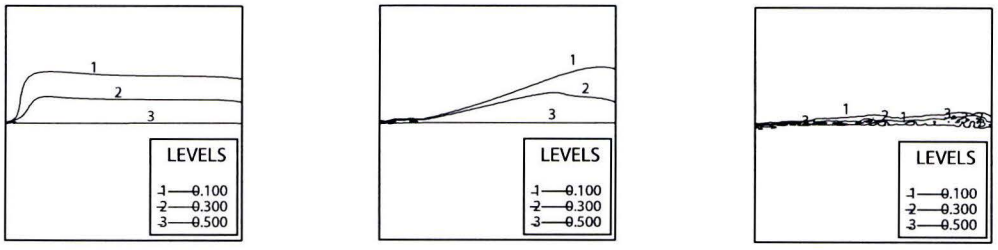

(a) (b) (c)

Figure 5.8: Material parameter distribution at time = t1 < t2 < t3 (a) t1, (b) t2, (c) t3

the convection of a steep gradient at the glass surface in the direction of the glass flow. To prevent an inaccurate description of the glass surface position this effect has to be minimized. In practice this is achieved by enlarging the domain in the radial direction, decreasing the influence of the inflow of fictitious fluid on the material label parameter gradient.

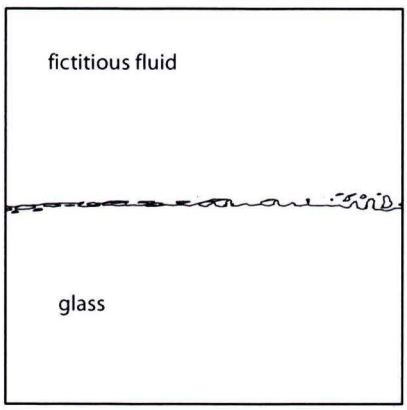

Figure 5.9: Distorted glass surface

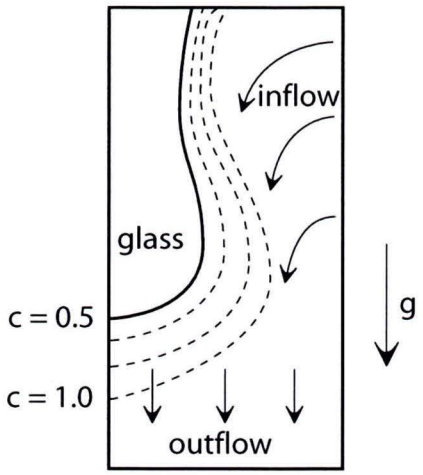

Figure 5.10: Convection of material parameter as a result of the inflow of fictitious fluid

5.1.2 Temperature convection

In this section we focus at glass temperature convection through the domain. In a gobform process the high temperature of the gob, 1000 °C, relative to the low temperature of the surrounding air, 20 °C, results in a large temperature gradient in a small air film close to the gob surface. During simulation, the convection of this local steep gradient of the temperature can lead to numerical diffusion, affecting the solution in the entire domain.

In the following simulations we examine the effect of this diffusion on the solution for a steep respectively a more moderate temperature gradient. To isolate the temperature convection, no heat exchange in the glass or in the fictitious fluid is allowed. Without heat exchange in the glass the effect on the solution can not spread out and can be visualized more easily.

1D: Uniform glass inflow with temperature transition

Consider the domain as discussed in section 5.1.1 and shown in Figure 5.1 (a). All the conditions are identical accept now that temperature is calculated as well. Two different simulations are performed with different initial condition for the temperature in the fictitious fluid. In the first simulation the transition of the glass temperature (1000 °C) to the ambient temperature (20 °C) is

initially prescribed over one element in the normal direction of the surface. This results in a steep temperature gradient at the glass surface. In the second simulation the transition is prescribed over a number of elements, resulting in a more moderate temperature gradient. The effect of the numerical diffusion on the glass temperature as a result of the convection of the steep respectively the moderate temperature gradient at the glass surface is shown in Figure 5.11.

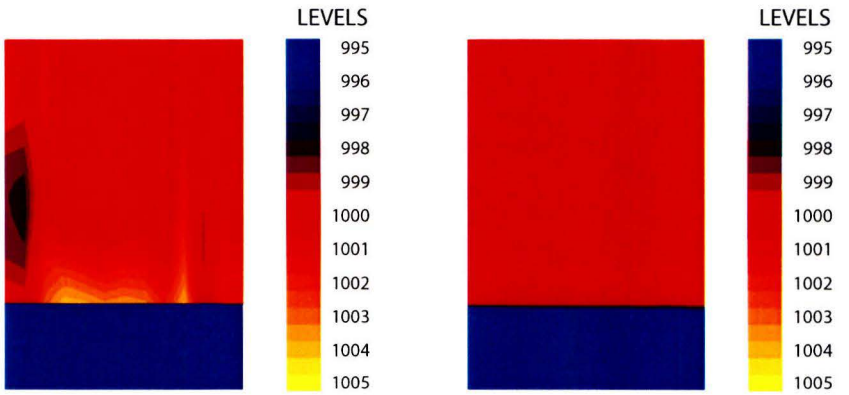

(a) (b)

Figure 5.11: Temperature solution glass (a) with steep gradient, (b) with moderate gradient

The results show that the temperature of the glass can be affected solely by the convection of the temperature gradient at the glass surface. The initial glass temperature was 1000 °C. In the simulation with the steep temperature gradient, Figure 5.11 (a), it can be seen that temperature deviations of about 4 °C occur. In the simulation with the more moderate temperature gradient, Figure 5.11 (b), it can be seen that the temperature of the glass is hardly affected. Here the temperature deviations are smaller than 1 °C.

Axisymmetric: Glass inflow with temperature transition

The numerical diffusion effect, discussed above, is studied here in a domain more comparable to a gobform simulation. Again, two simulations are performed with no heat exchange in the glass or fictitious fluid allowed. In the one simulation a steep gradient is prescribed in the fictitious fluid at the glass surface, in the other a more moderate temperature gradient is used.

Consider an axisymmetric domain similar to a gobform process, shown in Figure 5.12. Glass enters the domain with a temperature of 1000 °C. The abient temperature is 20 °C.

The domain of the simulation, with the initially prescribed moderate temperature gradient, is extended to compensate for the inflow of fictitious fluid on the right side of the domain. This inflow is the result of the outflow at the bottom of the domain as shown in Figure 5.10. In a small domain this inflow compressed the temperature gradient to such extend that it was comparable with the initial condition of the steep temperature gradient simulation. By extending the domain a more moderate temperature gradient was guaranteed. The results are shown in Figure 5.13.

In the simulation with the steep temperature gradient, Figure 5.13 (a), temperature deviations up to about 15 °C occur solely by the convection of the steep temperature gradient. This is comparable with the cooling of a gob skin during gob formation in a glass production plant. In the simulation with the moderate temperature gradient, Figure 5.13 (b), these temperature deviations are much smaller, less then 1 °C. Therefore, in the gobform model, the convection of steep temperature gradients has to be prevented by imposing a more moderate temperature gradient in the fictitious fluid. This is justified since the heat exchange to the environment is dominated by radiation and modelled separately.

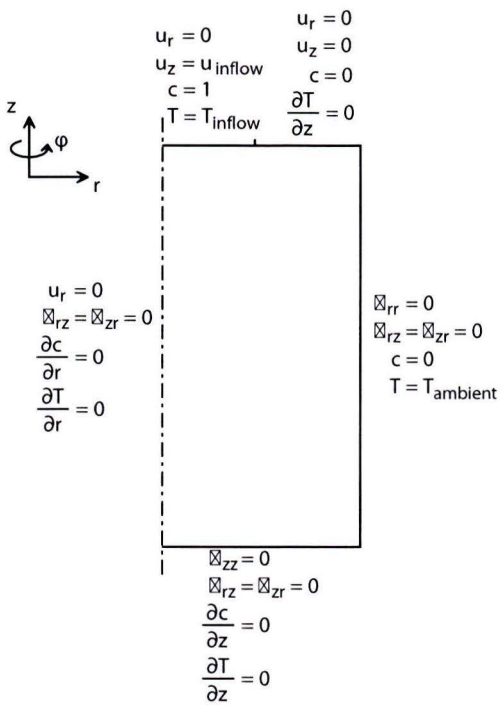

Figure 5.12: Initial and boundary conditions: Axisymmetric glass inflow with temperature transition

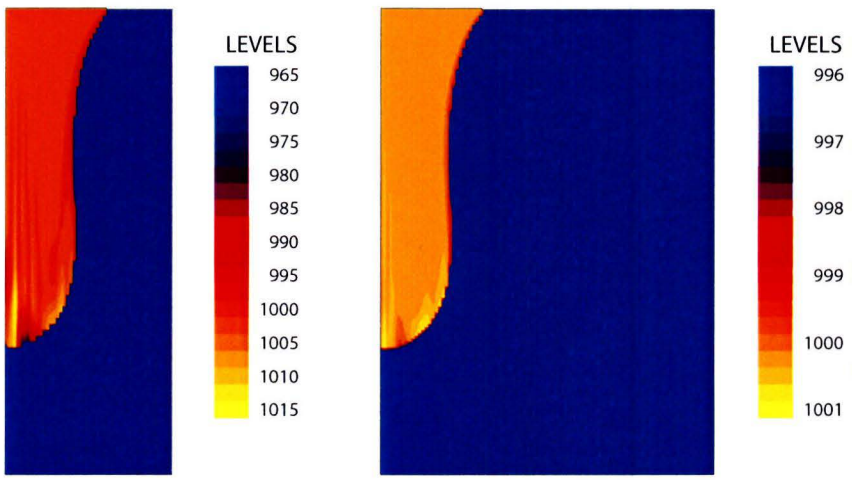

(a) (b)

Figure 5.13: Temperature solution gob (a) with steep gradient, (b) with moderate gradient

5.1.3 Radiative boundary condition

In this section the applicability of the implemented method for the simulation of the radiative heat transfer of the glass to the surroundings is examined. Since there is no straight forward method for imposing radiative heat transfer locally on a moving free surface, two different methods are developed as discussed in section 3.6. These are the transposed radiation heat flux method,

(TRH-method), and the imposed radiation heat sink method, (IRH-method). In this section these methods are compared to a reference simulation in a domain existing solely out of glass, consequently without a free surface, where the heat flux can be prescribed directly at the glass surface. Note that this section covers the radiative boundary condition only. At this point Rosseland is omitted and replaced with a uniform conductive property (30 $[\frac{W}{mK}]$) in the glass. In this way, the effect of the implemented method can be visualized in the computed temperature profile. Again our interest only lies in the glass domain. In the fictitious fluid the same conductivity is prescribed as in the glass. For the properties of the fictitious fluid the reader is referred to section 3.6. Static testcases regarding the flow are used in which the time dependent radiative heat transfer is calculated.

1D

Consider a container partly filled with glass as shown in Figure 5.14 (a). Initially the glass and fictitious fluid have a temperature of 1000 °C. The fictitious fluid is designed to have no internal energy capacity. The results are compared with the reference simulation as shown in Figure 5.14 (b). Here the same initial glass conditions are modelled without the presence of a fictitious fluid. Now the top of the domain represents the glass surface and the heat flux can be directly prescribed on the glass skin using boundary elements.

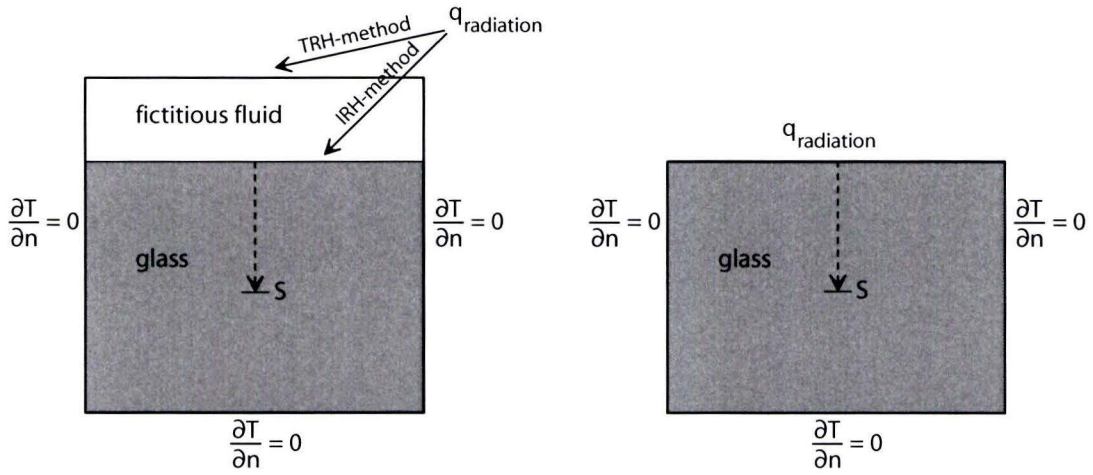

(a) (b)

Figure 5.14: Initial and boundary conditions 1D radiation testcase: (a) Transposed radiation heat flux method, TRH-method, respectively imposed radiation heat flux method, IRH-method, (b) reference simulation

The temperature profile, shown in Figure 5.15, is evaluated at the position and the direction denoted with the vector S in Figure 5.14. It can be seen that the TRH-method and the IRH-method both follow the reference simulation closely. The deviation is less then 1 °C. Only at the glass surface a more notable deviation of about 3 °C can be seen in the temperature solution of the IRH-method. This is the result of the prescription of the heat flux in the nodal points at the glass surface. In an element belonging to one of these nodal points this heat flux decreases linear over the element sides. As a result the heat flux is spread over the entire element resulting in the deviation as seen in Figure 5.15. By increasing the number of elements this effect on the temperature profile can be minimized.

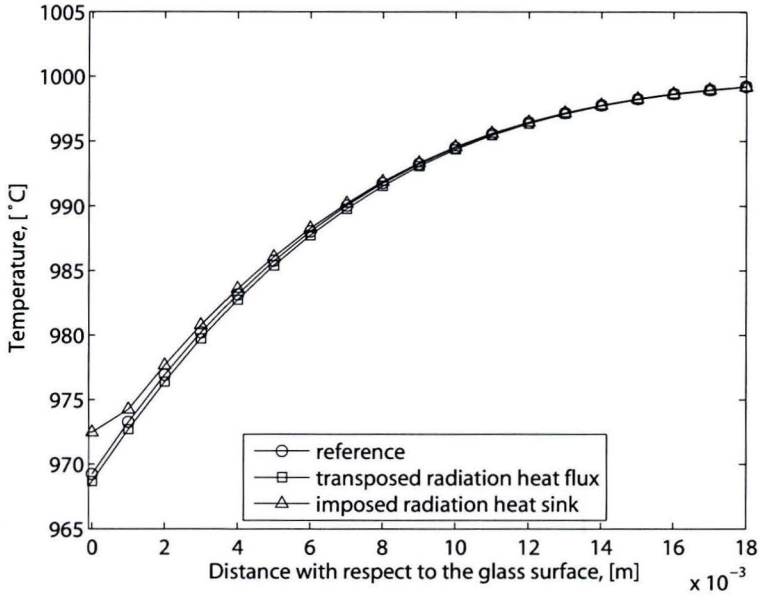

Figure 5.15: Temperature profile 1D radiation simulation at $t = 4.5s$

2D: Symmetric

In the following testcase special interest lies in the behavior of the transposed radiation heat flux. Since in this method the heat flux is not prescribed on the surface of the glass, orientation plays an important role. Furthermore, by transposing the heat flux in the TRH-method from the glass surface to another boundary the difference in boundary length has to be accounted for. This is done by multiplying the calculated glass surface heat flux with the ratio of the length of the glass surface with respect to the length of the boundary at which the heat flux is prescribed.

The domain is shown in Figure 5.16 (a). In the entire domain the initial temperature is 1000 °C. The same properties apply as above. In the transposed radiative heat flux method, the heat flux is prescribed at the top and right curve of the domain. Reference test is the domain as shown in Figure 5.16 (b). The same initial glass conditions apply without any presence of fictitious fluid. The hypothenuse represents the glass surface.

The vector S in Figure 5.16 denotes the position and the direction of the evaluated temperature profile as shown in Figure 5.17. It can be seen that in this 2D testcase the TRH-method as well as the IRH-method follows the reference simulation closely, with a deviation less then 1 °Ci in the TRH-method. Again in the temperature solution of the IRH-method a temperature deviation of about 3 °C can be seen at the glass surface. As discussed before this is the result of the linear distribution of the heat flux over an element at the glass surface. This effect can be minimized by increasing the number of elements.

The influence of the orientation of the heat flux boundary condition relative to the glass surface is tested for the TRH-method. This is done by performing the same simulation with the TRH-method as discussed above but now with the heat flux prescribed only at a single side, the top boundary. The difference on the temperature profile in glass as a result of a single side (top boundary) asymmetric heat flux or a dual side (top and right boundary), symmetric heat flux prescription is shown in Figure 5.18. Clearly a directional influence on the temperature profile can be seen. As a result the orientation of the temperature gradient is shifted somewhat in the asymmetric prescribed heat flux simulation in the direction of the top boundary. Therefore in the gobform model this orientation of the boundary condition must be taken into consideration. By enlarging the computational domain and spreading the heat flux evenly over the domain

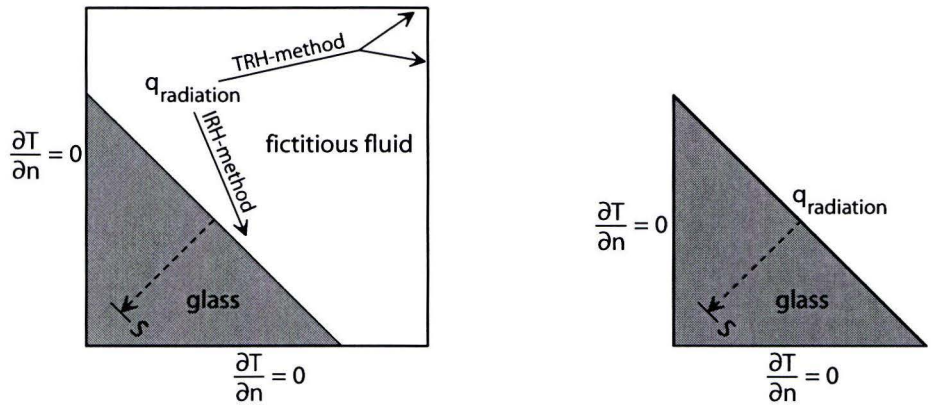

Figure 5.16: Initial and boundary conditions 2D symmetric radiation testcase: (a) Transposed radiation heat flux method, TRH-method, respectively imposed radiation heat flux method, IRH-method, (b) reference simulation

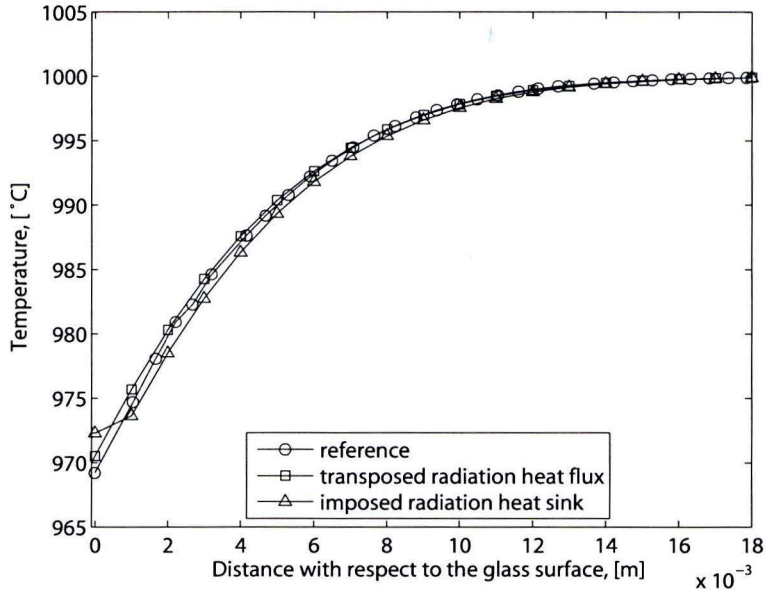

Figure 5.17: Temperature profile 2D symmetric radiation Test

boundaries, this effect can be reduced. Currently, the TRH-method and the IRH-method both give similar statisfactional results. Therefore, at this point no preference can be given. This will depend on the ease of use and the results in an axisymmetric gobform simulation.

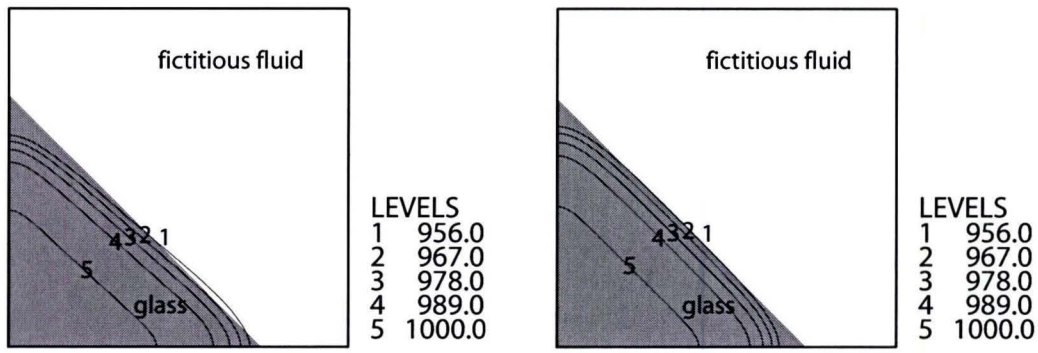

Figure 5.18: Temperature profile in glass with prescribed transposed heat flux method (a) asymmetric, (b) symmetric

5.2 Experimental validation

5.2.1 LG.Philips gobform experiment

Approach

A validation method of the computed shape of the gob has been carried out in cooperation with LG.Philips. Experimental data has been made accessible in [14] in which a model fluid was used in a scaled model of a continuous gobform process. The fluid properties were scaled to simulate the flow behavior of the glass under gobform conditions. The experimental set-up is mathematically simulated in a model of the spout, developed by TNO, to compute the input parameters for the gobform model. Results of computed gob shape are compared to the measured values of the experiments.

Set-up

The experiments, carried out in 1995 by LG.Philips, are done with a 1 : 2 scale model. The scale model consists of a feeder filled with a model fluid. The feeder is connected to a spout. In the spout a pin-tube mechanism controls the outflow through the orifice of the spout. Just underneath the orifice a cutting mechanism is installed to cut individual gobs in a continuous process. The fluid is collected in a tank and pumped back to the feeder. The model itself is not isotherm. In the tank the fluid is heated to about 37 °C and the surrounding temperature is about 20 °C.In the spout an insert piece just above the orifice is cooled at 21 °C, to simulate a gob with a cold skin.

In total the following experiments are described:

Case A) making a small gob with a small pin-tube
Case B) making a small gob with a big pin-tube
Case C) making a big gob with a small pin-tube
Case D) making a big gob with a big pin-tube

The lay-out with the dimensions of the spout with pin-tube mechanism is given in [14].

Model liquid

The model liquid used sucrose acetate isobutyrate (SAIB). It has a density of $1140 kg/m^3$, a specific heat capacity of $1470 J/kgK$ and a thermal conductivity of about $0.2 W/mK$. The viscosity is a

function of temperature and measured with a rotation viscosity meter, given in Table 5.1. For the simulation of the temperature dependency of the viscosity the Vogel-Fulcher-Tammann (VFT) relation is used as discussed in [2]. The approximation of the viscosity with the VFT relation is shown in Figure 5.19.

Table 5.1: Dynamic viscosity SAIB as function of temperature

Temperature [°C]	Viscosity [$Pa.sec$]
28.5	1152
30.8	423
34.7	216
36.8	181
41.0	68
45.0	53

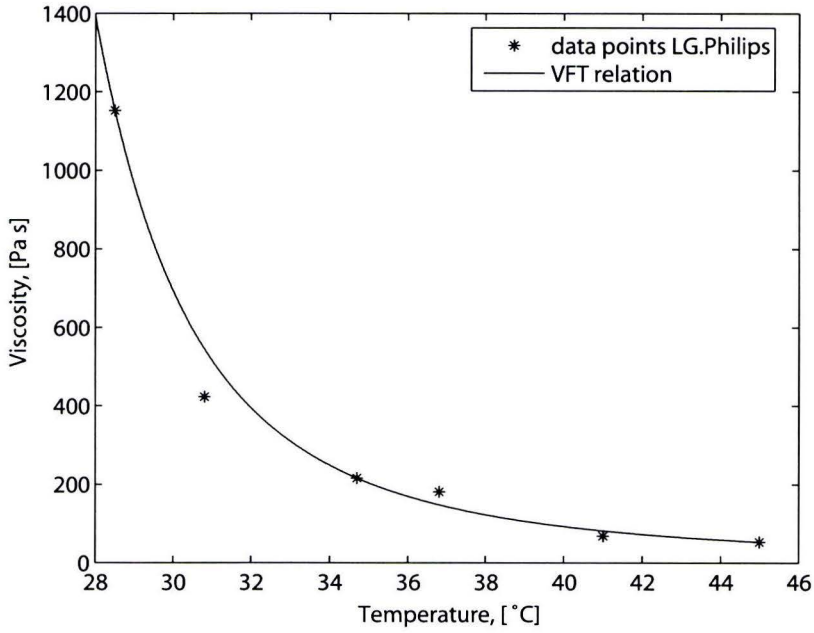

Figure 5.19: The temperature dependent dynamic viscosity approximated with the VFT relation

Results gob shape LG.Philips

The results of the experiments are studied with respect to the gob shape and weight. The gob shape was measured with a camera system just before the gob was cut. The difficulty to get reliable data with this measurement system was noted. The gob shape has been evaluated at characteristic lengths as shown in Figure 5.20. The results are shown in Table 5.2.

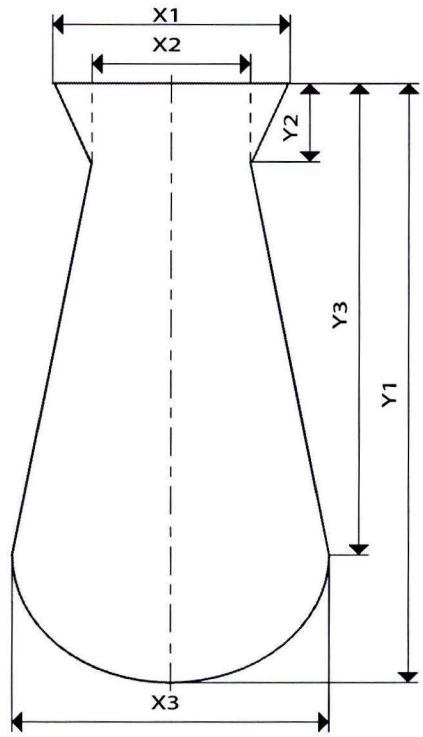

Figure 5.20: Characteristic gob shape definitions

Table 5.2: Results LG.Philips gobform experiment

Case	A	B	C	D
Results	small gob with small pin-tube	small gob with big pin-tube	big gob with small pin-tube	big gob with big pin-tube
Gob weight [kg]	0.221	0.275	0.604	0.638
X_1 [mm]	n.a.	n.a.	65	68
X_2 [mm]	40	45	61	62
X_3 [mm]	45	51	66	72
Y_1 [mm]	114	87	162	150
Y_2 [mm]	n.a.	n.a.	22	24
Y_3 [mm]	n.a.	n.a.	100	90

5.2.2 Results

In this section the validation procedure is discussed and the results of the experiments from LG.Philips are compared to the simulations with the gobform model. The validation procedure starts with the simulation of the different spout set-ups in a spout model from TNO. The spout model generates the fluid conditions regarding temperature and velocity at the spout orifice during a gobform cycle. With the velocity condition the mass of the gob is calculated which is used as a check for the results of the spout model. The calculated fluid conditions are used as a time dependent boundary condition at the spout orifice in the gobform model. The simulated and experimental gob shapes are compared on the basis of the characteristic gob shape definitions given in Table 5.2 and in Figure 5.20. In Figure 5.21 the different gob shapes are shown for case A to D.

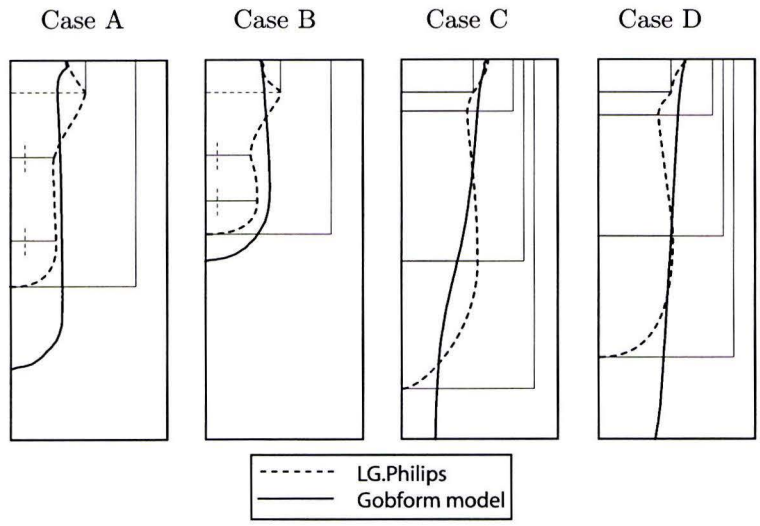

Figure 5.21: Comparison gob shapes

Table 5.3: Mass gobform experiment

	Mass experiment [kg]	Mass spout model [kg]	Mass difference
Case A	0.221	0.34	54 %
Case B	0.275	0.29	5 %
Case C	0.604	0.92	52 %
Case D	0.638	0.90	41 %

It can be seen that there is a considerable difference between the experimental and the simulated gob shape. The cause for this difference is believed to be a combination of an inaccurate boundary condition at the spout orifice and the unaccounted influence of the cutting mechanism on the gob shape. Their effect on the gob shape are discussed in the following.

Spout orifice condition

The spout orifice condition is calculated separately from the gobform domain in a spout model from TNO. In Figure 5.22 an example of the spout model domain is shown. It can be seen that the spout orifice lies at the edge of the domain. The assumption was made that during the gobform cycle only fluid passes this boundary. This assumption was translated in an essential boundary condition with respect to the material label parameter. However, simulation in the gobform model shows that the fluid underneath the spout, after gob cut, is pulled back by the movement of the pin in the pin-tube mechanism, resulting in a combined fluid and air flow across the spout orifice. In Figure 5.23 the fluid to air interface, the gob skin, is shown as it is pulled into the spout. The difference in the prescribed orifice condition can have a large influence on the simulated gob shape. Therefore, the mass flow through the orifice, computed with the spout model, is calculated during a gobform cycle to validate the magnitude of the fluid flow in time. After each cycle the total mass flow is the equivalent of the gob weight at time of cut. These values are compared to the experimental values in Table 5.3.

It can be seen that the output of the spout model differs considerably from the experimental values for three out of the four simulations. Since this output functions as input for the gobform

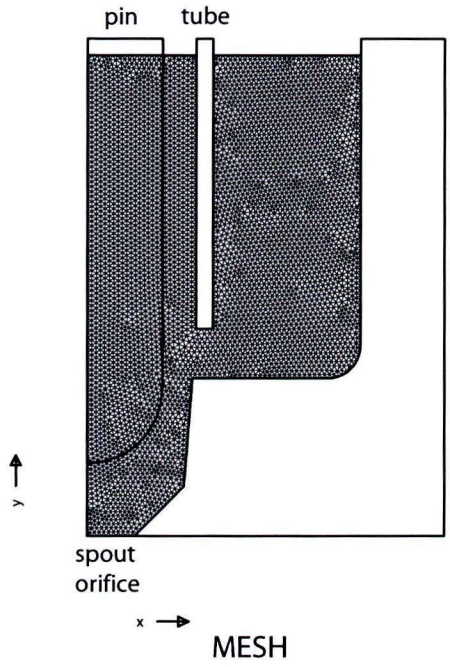

Figure 5.22: Example of spout geometry (case B)

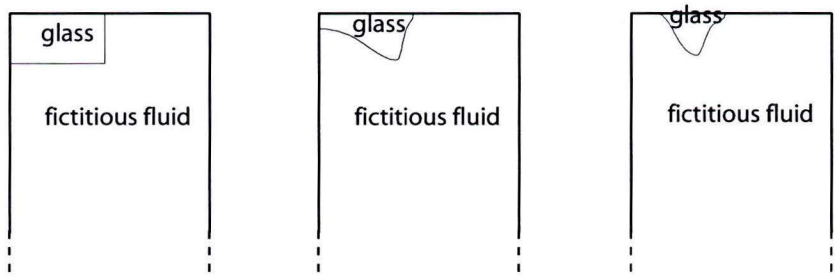

Figure 5.23: Retraction of the gob into the spout

model it will be clear that on ground of the difference in calculated mass only the simulation with a mass difference of about 5% can be used in the validation of the gobform model. Unfortunately, from this simulation not all the characteristic lengths are available as shown in Table 5.2. Furthermore an influence of the cutting mechanism on the gob shape could be seen as discussed below.

Influence cutting mechanism on gob shape

After each cycle time the cutting mechanism cuts individual gobs. From the results of the experiments performed by LG.Philips the question arose whether the cutting mechanism influenced the gob shape. Most probably the fluid had stick to the cutting shears, influencing the gob shape.

To test this influence two simulations are carried out in which the results of a gobform cycle with, and without fluid sticking to the shears are compared. The influence of the shears is simulated by prescribing a sticking condition of the fluid at the retracted shear position. The influence on the form of the gob is shown in Figure 5.24.

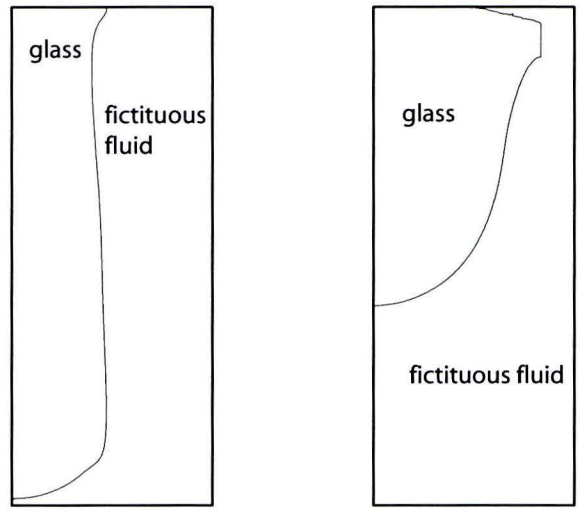

Figure 5.24: Gobform simulation (a) without fluid sticking on shears, (b) with fluid sticking on shears

It can be seen that the gob shape is drastically changed and the sticking behavior of the fluid on the shears plays an important role in the gobform experiment. Because a description of the cutting mechanism, used in the experiments from LG.Philips, is absent this feature can not be implemented in the validation simulations.

Chapter 6

Conclusions and recommendations

6.1 Conclusions

In this thesis, a model for the simulation of the glass gobforming process is developed in the finite element package SEPRAN. To avoid elaborate remeshing, a non-adaptive grid is used in the calculations. This causes the necessity to implement a method to determine the material position. For this a pseudo-concentration method is used. The essence of this method is that a so-called material label is assigned to every particle in the computational domain to designate its material identity. As a consequence, the physical properties of media in the domain are a function of the material label and the governing equations have material-dependent coefficients.

The media surrounding the gob has to be defined as a result of the fixed grid approach. In a glass production plant this is always air. In our simulations the air is represented by a fictitious fluid with viscosity of $\mathcal{O}(10^{-3})$ times the order of the glass viscosity but with the same mass density. In this way the Reynolds number in the air domain is reduced while the interaction between the fluid and the glass is preserved. The advantage of this replacement is that, due to the reduced Reynolds number in air, the non-linear terms in the conservation of momentum equation can be neglected in the entire domain.

The gobform process is simulated in a series of time-steps for which a flow problem, material label convection problem and a temperature problem have to be solved. A dimension analysis for the separate problems has shown that we can solve a (quasi-stationary) Stokes equation at every time-step. The material convection is modelled using a time dependent convection equation and the temperature is modelled using a time-dependent convection-diffusion equation.

In a glass production plant the gob surface will cool down from 1000 °C to about 950 °C during formation, depending on the time-scale. At these temperatures the heat transfer is dominated by radiation. Since the fixed grid approach results in a material transition at the glass surface, the applicability of known radiation models proved difficult. At this point radiation models based on the DOM-method as for example the improved diffusion approximation of Lentes and Siedow, are not yet able to deal with material interfaces. The fact that the glass surface acts as a moving free surface makes the adaptation even more difficult. Therefore a method is derived in which two parts are distinguished in the implementation of the radiative heat transfer of the glass. In the one part the internal heat transfer is prescribed using the Rosseland approximation. In the other the radiative heat transfer to the surroundings is prescribed as a glass surface boundary condition. For the implementation of this boundary condition, two different methods were developed. In the one, the TRH-method, the boundary condition is prescribed as a proportional heat flux at a boundary of choice of the computational domain. In the other, the IRH-method, the boundary condition is prescribed as a heat sink at the glass surface. In both methods the magnitude of the heat flux is approximated using $q_r = \sigma\varepsilon(T^4_{glass} - T^4_{ambient})$. Therefore the emissivity ε has to be determined. In our case, this is the total hemispherical emissivity.

This emissivity has to be determined at gob formation temperatures of about 1000 °C. How-

ever, in this temperature domain glass is in liquid state complicating accurate measurement procedures. Therefore measurement are performed at 600, 700 and 800 °C. The results are extrapolated to the desired temperature domain. This extrapolation requires that the variance in the absorption coefficient with temperature has a small effect in the calculation of the total hemispherical emissivity. An analysis showed that the use of an absorption coefficient measured at $T = 20\,°C$ in comparison with one measured at $T = 1000\,°C$ gave a maximum difference of about 2.0% in the calculated emissivity at $T = 1000\,°C$.

In an experimental set-up, the emissivity was derived from spectral energy measurements. In this derivation, the directional dependency had to be accounted for. Since measurements took place in one direction, perpendicular to the glass surface, the directional dependency was derived from literature values. This resulted in a drop of total hemispherical emissivity of about 28%. A similar procedure was followed for the derivation of the emissivity from data from TNO, [9], of the absorption coefficient from a comparable glass type. Comparison between the two showed similar results. An analysis of the emissivity showed that at gobform conditions a uniform emissivity could be chosen in the entire domain. To verify the experimental results an experimental analysis has been performed with respect to the optical alignment, the spectral transformation factor, the ground intensity correction and the reproducibility.

To validate the gobform model, numerical tests are performed on the individual parts of the model. Simulations with the material convection and the temperature convection algorithm showed good results if moderate gradients at the glass surface are considered. The results regarding the radiative boundary condition showed corresponding results between the TRH-method, the IRH-method and the reference simulation. An experimental validation simulation has been performed using data from a scaled LG.Philips gobform experiment. In this experiment the glass was replaced by a model fluid with scaled properties to simulate the flow behavior of the glass under gobform conditions. For the simulation in the gobform model a spout model of TNO has been used to calculate the necessary boundary flow conditions of the spout. A calculated gob mass difference between the spout model simulation and the LG.Philips experiment was used as a verification of the spout model. It showed that three out of four simulations could not be used in the validation process as a result of the difference in mass which was in excess of 40%. In the one remaining simulation some of the characteristic gob length information was missing in the received data from LG.Philips. Furthermore, the simulation showed a major influence of the cutting mechanism, used in the experiment to cut individual gobs. Since detailed information about the cutting mechanism and its dynamical behavior was absent, this feature has not been implemented in the simulation. Hence the gobform model could not yet be validated with regards to the measured gob shape.

In conclusion, we can state that the gobform model is able to approximate gob shape and temperature profiles in a gobforming process. In contradiction to models based on DOM-methods such as the non-spectral DOM-model and the improved diffusion approximation of Lentes and Siedow, the implementation of the radiative heat flux using Rosseland in combination with either the IRH-method or the TRH-method is able to deal with the moving free surface of the gob. The numerical test, used as a first validation method for the individual parts of the gobform model showed promising results. Currently, the TRH-method and the IRH-method both give similar satisfactional results. Therefore, at this point no preference can be given. This will depend on the ease of use and the results in an axisymmetric gobform simulation.

6.2 Recommendations

Although the gobform model that has been developed showed promising results, still some challenges remain. Some of these challenges will now be discussed in the following recommendations.

The numerical test performed have shown the necessity for moderate material parameter or temperature gradients. The convection of steep gradients has to be avoided to preserve accuracy at the glass surface. Since in general the convection of steep gradients represent an important numerical problem in numerical simulations it is recommended to further examine this type of problem in search of a possible solution.

At this point the use of a Rosseland approximation for the internal radiative heat transfer results in a validity range in which optically thin glasses are excluded. It would be interesting to examine the magnitude of the error in the temperature profiles for these types of glasses. To further increase the accuracy of the gobform model we would like to incorporate a more extensive radiation model based on the DOM-method. However as long as these are not able to deal with a moving free surface, and computational times are large, this cannot be done. This would signify a enlargement of the validity range with respect to the optical properties of the glass.

In the TRH-method, a heat flux proportional to the heat flux at the glass surface, has to be prescribed at the domain boundaries. This proportionality has to account for the difference in surface area. Curently, a time-dependent approximation is used. In the future, it would be preferrer to incorporate a numerical subroutine which evaluates the glass surface area at every time-step, hence the proportionality can be calculated.

Bibliography

[1] Olaf op den Camp, Dries Hegen, Gerard Haagh, and Maurice Limpens. TV-panel production: the simulation of the forming process. 63rd Conference on Glass Problems, Charles H. Drummond 3rd Editor, October 22-23, 2002. Columbus Ohio, USA.

[2] H. de Waal and R.C.G. Beerkens. NCNG-glascursus. Technical report, NCNG, 1997.

[3] Adrian Bejan. Heat transfer. John Wiley & Sons, Inc., 1993.

[4] Maurice P.M.A. Limpens. A design tool for conveyor belt furnaces. PhD thesis, Eindhoven University of Technology, 2000. ISBN 90-386-2562-6.

[5] F Lentes and N Siedow. Three-dimensional radiative heat transfer in glass cooling process. Glastech. Ber. Glass Sci. Technol. 72, 6:188–196, 1999.

[6] A.M. Lankhorst and B.D. Paarhuis. Radiation model versus rosseland. Technical Report DMP-MEM-030000, TNO Institute of Applied Physics, 2003. Confidential.

[7] Gerard Haagh. Simulation of gas-assisted injection moulding. PhD thesis, Eindhoven University of Technology, 1998. ISBN 90-386-0620-6.

[8] G Segal. Sepran standard problems. Ingenieursbreau SEPRA, NL, 2005.

[9] P.A. Nijnatten. Radiative heat transfer in industrial glass melts. Technical Report HAM-RPT-00-141, TNO Institute of Applied Physics, 2000. Confidential.

[10] Marco Nagtegaal. Optical method for temperature profile measurements in glass melts. PhD thesis, Eindhoven University of Technology, 2002. ISBN 90-386-2694-0.

[11] Perkin-Elmer. Spectrum GX FT-IR Users Guide. Perkin-Elmer Corporation, UK, 1998.

[12] Michael F. Modest. Radiative heat transfer. Academic Press, 1993.

[13] R. Siegel and J.R. Howell. Thermal radiation heat transfer. Taylor & Francis, 2002.

[14] W. van Schaik. Data of 1:2 scale model gobforming. Technical Report GLI-614-05-V0295, LG.Philips Displays, 2005. Memo.

[15] F.L Pedrotti and L.S. Pedrotti. Introduction to optics. Prentice Hall, 1993.

Appendix A

Radiation constants

Symbol	Definition	Value
C_1	Constant in Planck's spectral energy (or intensity) distribution	$0.59552137 \times 10^{-16}\ Wm^2/sr$
C_2	Constant in Planck's spectral energy (or intensity) distribution	$0.014387752\ mK$
C_3	Constant in Wien's displacement law	$0.0028977686\ mK$
h	Planck's constant	$6.62606876 \times 10^{-34}\ Js$
k	Boltzmann's constant	$1.3806503 \times 10^{-23}\ JK^{-1}$
σ	Stefan-Boltzmann constant	$5.670400 \times 10^{-8}\ W/(m^2K^4)$

Appendix B

Definitions for axisymmetric flow

Here some of the definitions for the flow are given in cylindrical coordinates:

$$\nabla v = \left(\frac{\partial v}{\partial r},\ \frac{1}{r}\frac{\partial v}{\partial \varphi},\ \frac{\partial v}{\partial z}\right)^T \tag{B.1}$$

$$\nabla \cdot \mathbf{u} = \frac{1}{r}\left(\frac{\partial r u_r}{\partial r} + \frac{\partial u_\varphi}{\partial \varphi} + \frac{\partial r u_z}{\partial z}\right) \tag{B.2}$$

$$\sigma_{rr} = -p + 2\eta\frac{\partial u_r}{\partial r} \tag{B.3}$$

$$\sigma_{\varphi\varphi} = -p + 2\eta\left(\frac{u_r}{r} + \frac{1}{r}\frac{\partial u_\varphi}{\partial \varphi}\right) \tag{B.4}$$

$$\sigma_{zz} = -p + 2\eta\frac{\partial u_z}{\partial z} \tag{B.5}$$

$$\sigma_{r\varphi} = \sigma_{\varphi r} = \eta\left(r\frac{\partial}{\partial r}\left(\frac{u_\varphi}{r}\right) + \frac{1}{r}\frac{\partial u_r}{\partial \varphi}\right) \tag{B.6}$$

$$\sigma_{\varphi z} = \sigma_{z\varphi} = \eta\left(\frac{1}{r}\frac{\partial u_z}{\partial \varphi} + \frac{\partial u_\varphi}{\partial z}\right) \tag{B.7}$$

$$\sigma_{rz} = \sigma_{zr} = \eta\left(\frac{\partial u_r}{\partial z} + \frac{\partial u_z}{\partial r}\right) \tag{B.8}$$

Appendix C

Spectral transformation factor

The spectral transformation factor, $\frac{i_{\lambda b}(T_b)}{s_{\lambda b}(T_b)}$, is discussed in section 4.4.2. Here the spectral transformation factor is shown from measurements between $T = 600 - 1200\,°C$.

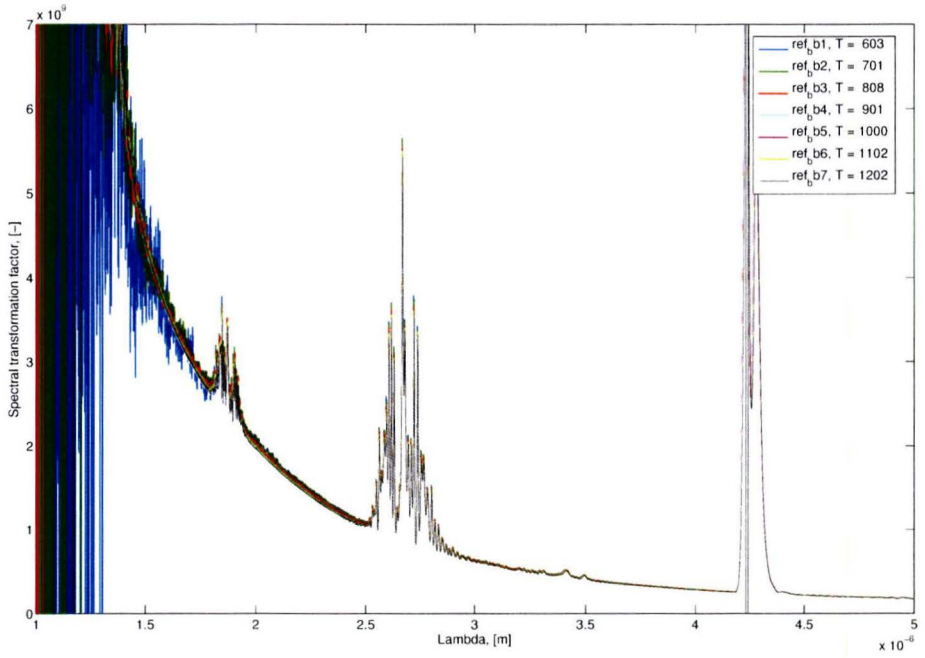

Figure C.1: Spectral transformation factor between T = 600 - 1200 °C

Appendix D

Addition to the experimental set-up

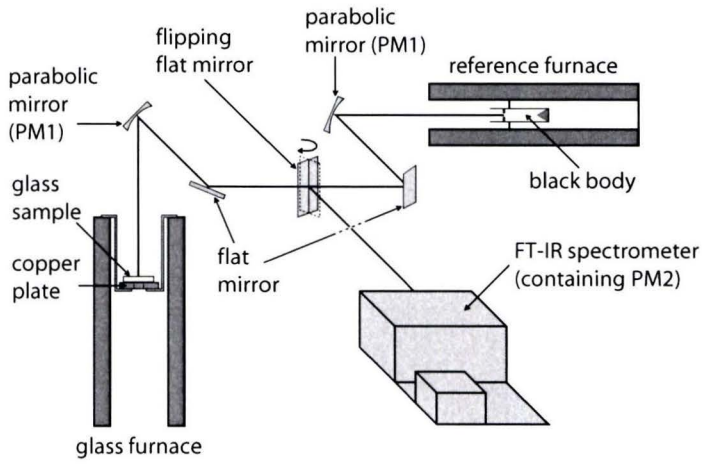

Figure D.1: Overview of the experimental setup

D.1 Black body

In practice a black body, defined as a perfect absorber and emitter, does not exist. It is a theoretical idealization that is often used as a reference in radiation calculations. The black body used in the emissivity experiments consists of a stainless steel cylinder with a small inner diameter, compared to the cylinder length. The front side is closed with a plate with a small circular hole in the center. The back side of the cylinder is closed completely. At this side a cone is placed, pointing in the direction of the symmetry axis toward the front side. The cone is used to increase the effective emissivity of the black body. If an incident beam enters the black body, it is partly absorbed by the cone wall. The part that is not absorbed is reflected towards another wall inside the black body. Here, again a part of the beam is absorbed and a part will be reflected towards yet another wall, and so on. In this way, only a very small fraction of the incident beam will be reflected in the direction of the opening. For this type of "black body" the emissivity is larger than 0.999 according to [10].

D.2 Working principle FT-IR spectrometer

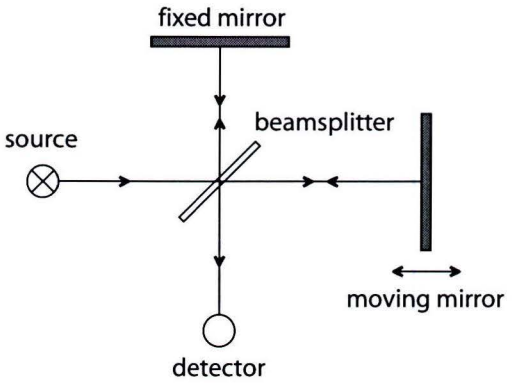

Figure D.2: Working principle FT-IR spectrometer, the Michelson interferometer

The working principle of the FT-IR spectrometer is based on the same principle as the Michelson interferometer, shown in Figure D.2. In a Michelson interferometer, a beamsplitter divides a beam of radiation emitted by a source into a transmitted and a reflected part. One part is directed to a fixed mirror, the other to a moving mirror. In this way an optical path difference can be created. Both beams are reflected at the mirrors, back towards the beamsplitter. At the beamsplitter, these beams are again split in a transmitted and a reflected part. The transmitted part of one beam is combined with the reflected part of the other and vice versa. As a consequence approximately 50% of the original beam will be directed in the direction of the detector, respectively in the direction of the source. If the optical path distance between the beamsplitter and the fixed mirror, respectively the moving mirror are the same, the original emitted beam is unchanged. However if the optical path distances are different, the recombination leads to an interference pattern at the detector. This interference pattern is a function of optical path distance. The spectral energy, power versus wavelength, emitted by the source, can now be found by Fourier transformation of the interference pattern. Measurements take only a fraction of a second.

D.3 Optics

In this section, we first discuss the optical components. For simplicity, we distinguish the components inside and outside the FT-IR spectrometer. Then, we discuss the optical alignment calculations needed to position our measurement beam. This analysis follows Nagtegaal, [10], in which the alignment method is based on the position of the b-stop image. The b-stop is an aperture situated inside the FT-IR spectrometer.

D.3.1 Optical components

The set-up for the optical components outside the FT-IR spectrometer can be seen in Figure D.1. Radiation from a glass sample or the black body is reflected by a parabolic mirror towards a flat mirror, which on its turn reflects it in the direction of the flipping mirror. This flipping mirror is used to choose the direction of the measured beam. In one position it reflects the radiation coming from the optical path of the glass sample towards the FT-IR spectrometer. In the other it reflects the radiation coming from the optical path of the black body towards the FT-IR spectrometer. The components in the optical paths and the path lengths must be the same during the experiments. This is a requirement for the derivation of the spectral intensity. Since the components and the lengths of these paths are the same we will further address these paths and components as one.

The parabolic mirror in the optical path outside the FT-IR spectrometer is important for the positioning and the size of the measurement spot. From the measurement position this is the first encountered parabolic mirror and is therefore called PM1. This is the same mirror as used by Nagtegaal, [10], with a focal point of $76.2cm$. This focal point is checked using Bessel's method.

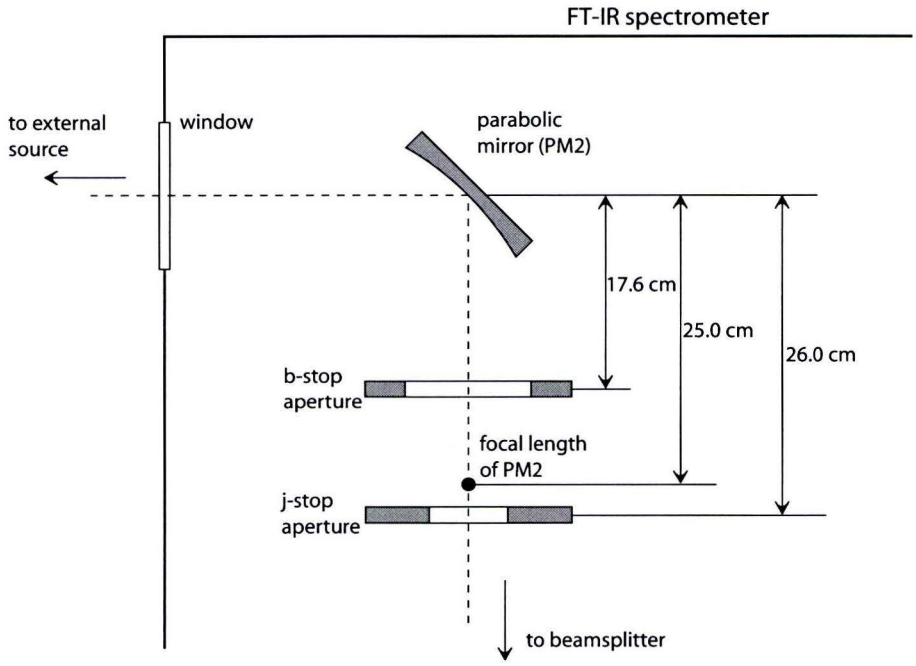

Figure D.3: Part of the FT-IR spectrometer that contains the j-stop, the b-stop and parabolic mirror PM2

The radiation reflected by the flipping mirror enters the FT-IR spectrometer at the external window. This incident radiation is directed through a complicated optical path via plane mirrors, a parabolic mirror, the b-stop and j-stop apertures and a beam splitter towards the detector. Since the lay-out of these components is confidential and the sensitivity of the apparatus does not allow internal measurements by the user, we use the information from [10], shown in Figure D.3. This information is required for the optical alignment for the measurement position at the external power source. The parabolic mirror inside the FT-IR spectrometer is the second one encountered from the measurement position and is therefore called PM2. The two other components, important for the optical alignment, are the variable, software-controlled, b-stop and j-stop (Jacquinot-stop) diaphragm apertures. The b-stop determines the area of the beam that enters the beamsplitter and consequently the area of the beam that enters the detector. A larger b-stop results in a larger measurement area and therefore a higher detected spectral energy level. The j-stop restricts the divergence of the beam in the direction of the beamsplitter. Together, the B- and j-stop determine the solid angle of the radiation from the external source passing through the FT-IR spectrometer.

D.3.2 Optical alignment calculations

In this section, we discuss the optical alignment calculations, following [15], for the derivation of the measurement spot position as well as the measurement spot size. The optical alignment method used is based on the image position of the b-stop, following [10]. In this method, the image position of the b-stop is defined as a measurement spot. In our case, this image is positioned at the top of a glass sample respectively at the entrance of the black body.

In the calculations for the determination of the position of the b-stop image, we use the values of the internal optical components as shown in Figure D.3. To calculate this position, we can use the lens formula, equation (D.1),

$$\frac{1}{b} + \frac{1}{v} = \frac{1}{f} \tag{D.1}$$

with b and v the image and the object distance respectively with respect to the parabolic mirror. The focal length of the parabolic mirror is f. Although this formula is derived for lenses, it can also be used for parabolic mirrors. For the completeness of the optical positioning analysis, the position of the j-stop image will also be calculated,

When we talk about the b-stop or j-stop image, we actually mean the position of the image of the referred aperture with respect to one of the parabolic mirrors, PM1. This position is the result of the combination of both parabolic mirrors, PM1 and PM2. Therefore in our calculations we have to distinguish between image positions with respect to the one or the other. For this purpose, we use in the notations of object, image and focal length of a parabolic mirror, the subscript "$_1$" for PM1 and subscript "$_2$" for PM2.

In our calculations, we first apply the lens formula on PM2. From this we can calculate the first image position with respect to PM2, b_2. It is important to understand how this image serves as the object, v_1, for parabolic mirror PM1. To calculate v_1 from b_2 we use equation (D.2),

$$v_1 = D_{PM1-PM2} - b_2 \tag{D.2}$$

in which $D_{PM1-PM2}$ denotes the distance between parabolic mirrors PM2 and PM1. Combining equation (D.1) and (D.2), we can now derive an expression for the image position with respect to PM1 as a function of $D_{PM1-PM2}$:

$$b1 = \frac{f_1}{1 - \frac{f_1}{D_{PM1-PM2} - b_2}} \tag{D.3}$$

with

$$b2 = \frac{f_2}{1 - \frac{f_2}{v_2}} \tag{D.4}$$

The position of the parabolic mirror and the b-stop and j-stop apertures inside the FT-IR spectrometer are fixed. Therefore, we can only influence the position of the images of the apertures with respect to PM1, by varying the distance between the parabolic mirrors PM2 and PM1, shown in Figure D.4. It can be seen that the distance between the j-stop and b-stop image differ enough to make a distinction, during the alignment of the optics procedure.

Another important quantity is the magnification of the image at PM1 with respect to the size of the object at PM2. Our set-up is a system of parabolic mirrors. Therefore the total magnification, M_T, is the product of the magnifications of the individual mirrors, M_1 and M_2 , equation D.5.

$$M_T = M_1 M_2 = (-\frac{b_1}{v_1})(-\frac{b_2}{v_2}) = \frac{b_1 b_2}{v_1 v_2} \tag{D.5}$$

We can now calculate the magnification of the images of the apertures. This is especially useful for the b-stop image positioned at the black body entrance. Care must be taken to ensure that the image can access the black body without "touching" the side plate. The entrance to the black body is limited to about $16mm$. The total magnification of the b-stop and j-stop image is given in Figure D.5.

Combining Figure D.4 and Figure D.5, we can now determine our optical alignment set-up. The distance between parabolic mirror PM1 and PM2 is approximately $260cm$. This gives a b-stop an j-stop image position, with respect to PM1, of about $100cm$, respectively $64cm$. The total magnification of the b-stop and j-stop image are respectively -1.1 and -4.1. Because of the magnification, the b-stop diameter is set to $10.0mm$. This way the image size is $11mm$, small enough to enter the black body. The j-stop diameter is set fully open, at $12.5mm$, to maximize the incident radiation at the detector.

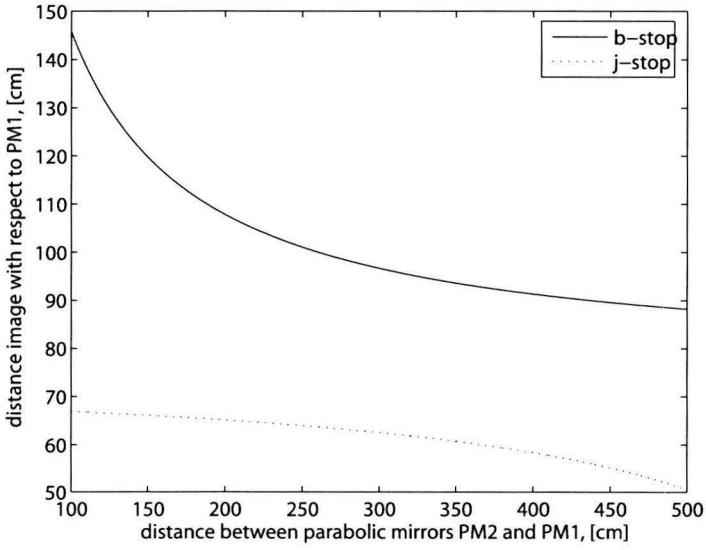

Figure D.4: b-stop and j-stop image position with respect to PM1

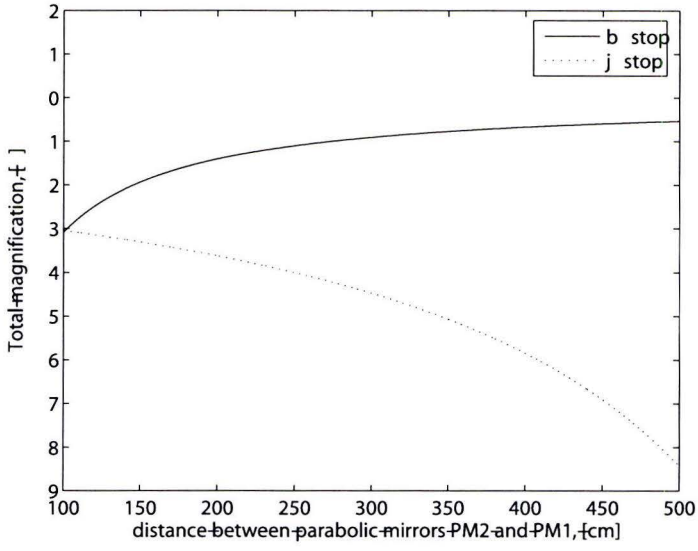

Figure D.5: Total b-stop and j-stop image magnification

Appendix E

1D:Uniform glass inflow, non-uniform elements distribution

Below, the results are shown from the 1D uniform glass inflow simulation with the mesh using non-uniform elements, as discussed in section 5.1.1.

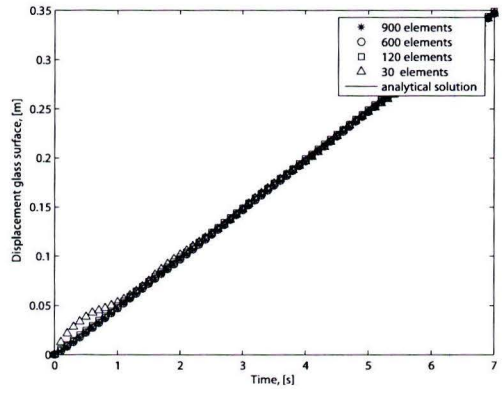

Figure E.1: Glass surface displacement

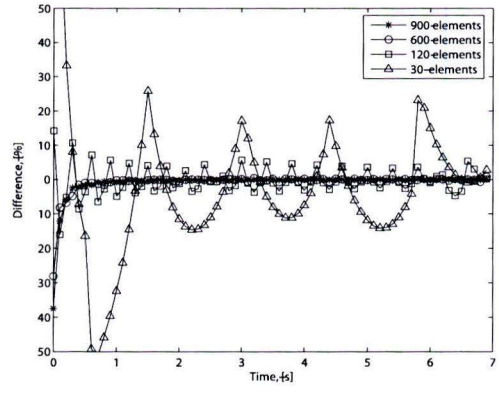

Figure E.2: Glass surface displacement per time step in proportion to the analytical solution

Appendix F

Heat flux vector field in gobform simulation

The characteristic heat flux vector field in gobform simulation is shown in figure F.1 for the TRH- and IRH-method.

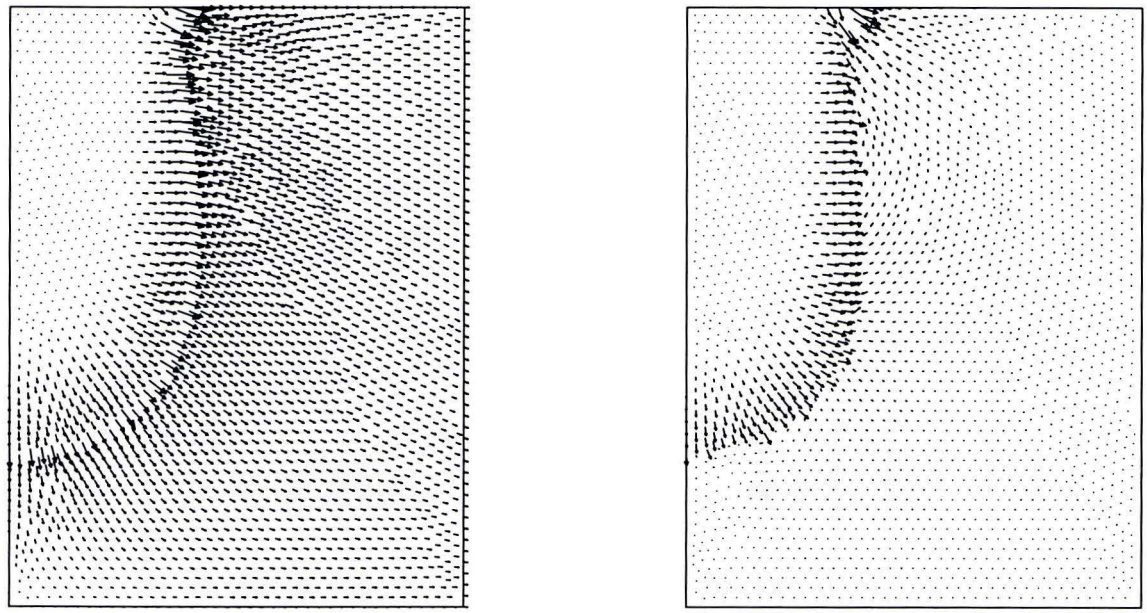

(a) (b)

Figure F.1: Heat flux vector field: (a) TRH-method, (b) IRH-method

Appendix G

Example gobform simulation

An example of a gobform simulation is shown in figure G.1. The simulation was performed using the IRH-method.

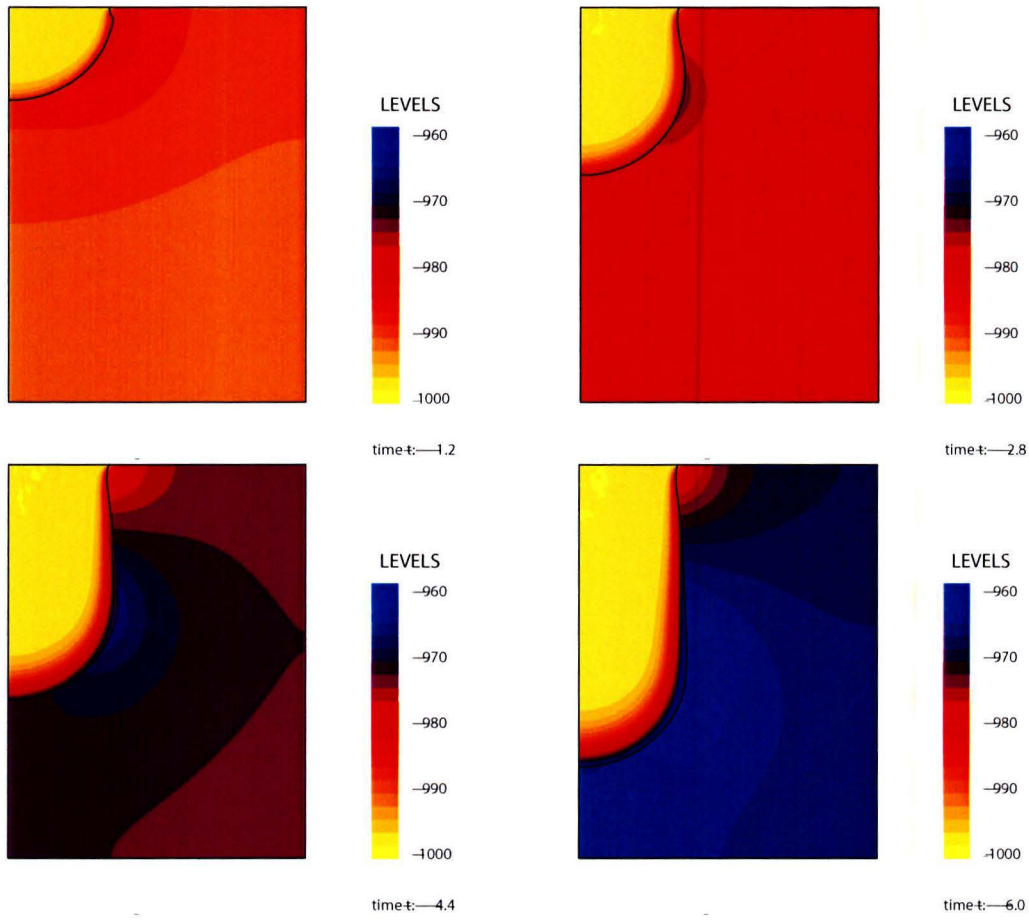

Figure G.1: Gobform model results: temperature profile and gob shape

Samenvatting

In het productieproces van glas worden afzonderlijke glasdruppels geproduceerd uit een continue glasstroom. De druppels worden losgeknipt en geleid naar de laatste fase in het vormingsproces. In dit productieproces zijn een reproduceerbaar gewicht, vorm en temperatuurverdeling in de druppel essentieel, omdat zij effect hebben op de gelijkvormigheid en reproduceerbaarheid van het eindproduct. Variatie in de temperatuurverdeling in de laatste fase van het vormingsproces kan leiden tot plaatselijke glasfouten, grote inwendige spanningen en vormafwijkingen in het eindproduct. Deze temperatuurverdeling kan worden afgeleid van de temperatuurverdeling in het glas gedurende de druppelformatie. Voor een beter begrip en besturing van het gobformproces is een model ontwikkeld waarin de vorm van de glasdruppel en de temperatuurverdeling kunnen worden gesimuleerd.

Het gobformmodel maakt gebruik van de eindige elementen methode. In het model wordt de pseudo-concentratie methode toegepast. De geldende vergelijkingen worden opgelost in een vast grid over het gehele domein. In dit domein wordt een onderscheid gemaakt tussen de glasdruppel en de omringende lucht. Omdat onze interesse niet ligt in een correcte beschrijving van het fysische gedrag van de lucht, kan deze worden vervangen door een fictieve vloeistof met een viscositeit die 10^{-3} keer kleiner is dan de viscositeit van het glas. De dichtheid van de fictieve vloeistof blijft echter gelijk aan die van lucht. Door deze substitutie wordt het Reynolds getal verlaagd zonder hiermee de interactie tussen het glas en de omringende lucht te veranderen. Als gevolg van het verlaagde Reynolds getal, kunnen we de niet lineaire termen uit de conservatie van momentum vergelijking verwaarlozen. In de pseudo-concentratie methode wordt een "material label" geïntroduceerd, c, om een onderscheid te kunnen maken tussen het glas en de fictieve vloeistof. Alle materiaaleigenschappen zijn gedefinieerd als een functie van deze "material label".

In een gobformproces wordt de warmteoverdracht van de glasdruppel naar de omgeving gedomineerd door straling. In verhouding is de convectieve warmteoverdracht in de lucht rond de glasdruppel ongeveer 6%. In het modelleren van het gobformproces ligt de grootste uitdaging in de eigenschappen van de semi-transparante stralingswarmteoverdracht in combinatie met het bewegende vrije oppervlak van de glasdruppel. Op dit moment zijn de bekende, op de DOM-methode gebaseerde stralingsmodellen, zoals bijvoorbeeld de "improved diffusion" methode van Lentes en Siedow, nog niet toepasbaar in simulaties met een materiaal interface. Daarom is er een methode ontwikkeld, waarin er onderscheid gemaakt wordt in de interne stralingsoverdracht in het glas en de stralingsoverdracht van de glasdruppel naar de omgeving. Inwendig in de druppel wordt een Rosseland benadering toegepast. Twee verschillende methodes zijn ontwikkeld voor de beschrijving van de warmteoverdracht naar de omgeving. In de ene methode, de TRH methode, wordt de warmteoverdracht proportioneel voorgeschreven op een gekozen rand van het rekendomein. In de andere methode, de IRH methode, wordt de warmteoverdracht voorgeschreven als een putterm liggende op het glasoppervlak van de druppel. De grootte van de heat flux is benaderd met $q_r = \sigma\varepsilon({T_{glas}}^4 - {T_{omgeving}}^4)$. In ons geval is ε, de niet-spectrale hemisferische emissiviteit.

Een voorbeeld van de emissiviteit, ε, wordt afgeleid van spectrale metingen van ruitenglas. In deze experimenten wordt gemeten bij glassample temperaturen van 600, 700 en 800 °C. De resultaten, verkregen bij deze temperaturen, worden gextrapoleerd naar het temperatuurgebied van het gobformproces, ongeveer 1000 °C. De geldigheid van deze extrapolatie is gebleken uit een analyse van de temperatuurafhankelijkheid van de absorptiecoëfficiënt van het glas. De spectrale energie is loodrecht op het glasoppervlak gemeten. De richtingsafhankelijkheid is geïntroduceerd

met behulp van gevonden waarden in de literatuur. De resultaten voor de totale hemisferische emissiviteit zijn vergeleken met de waarden afgeleid van de door TNO gemeten absorptiecoëfficiënt van een vergelijkbaar glastype. De resultaten kwamen goed overeen. Op de experimenten is een analyse uitgevoerd betreffende de optische uitlijning, de spectrale transformatiefactor, de grond intensiteit en de reproduceerbaarheid.

Het model is gevalideerd door gebruik te maken van numerieke tests en van data van een geschaalde (isotherme) gobformsimulatie van LG.Philips. In de numerieke tests worden verschillende onderdelen van het gobformmodel individueel gevalideerd. Er is een goede overeenkomst met de referentie-oplossingen. De resultaten van het gobform model en de data van LG.Philips geven afwijkende resultaten wat betreft de vorm van de glasdruppel. Enerzijds is dit het gevolg van de afwijking in de voorgeschreven randvoorwaarden voor de glasinstroom op de "spout orifice". Anderzijds is dit het gevolg van het ontbreken van informatie over de invloed van het knipmechanisme. De instroom randvoorwaarde is verantwoordelijk voor een afwijking in de massa van de glasdruppel van 5 tot 50%, afhankelijk van de gesimuleerde case. De invloed van het knipmechanisme is afgeleid van de resultaten van de karakteristieke glasdruppelafmetingen, zoals beschreven in de data van LG.Philips. Daarom, op basis van deze bevindingen, kunnen de data van LG.Philips niet gebruikt worden in de validatie van het gobform model.

Concluderend kan gesteld worden, dat het ontwikkelde model in staat is om het gobformproces te simuleren. In tegenstelling tot frequent gebruikte stralingsmodellen, is de geimplementeerde stralingswarmteoverdracht in staat om te gaan met het bewegende materiaal interface.